Provided for non-commercial research and education use.
Not for reproduction, distribution or commercial use.

ISSN 0016-7037
Volume 87
June 15, 2012

ELSEVIER

Geochimica et Cosmochimica Acta

JOURNAL OF THE GEOCHEMICAL SOCIETY
AND THE METEORITICAL SOCIETY

Executive Editor: Marc Norman

Associate Editors: Robert C. Aller, Jeffrey C. Alt, Yoko Amelin, Carol Arnosti, Miriam Bar-Matthews, Liane G. Benning, Thomas S. Bianchi, Jamie Blundell-Tuff, Alan D. Brandon, David J. Bunker, Peter Burnard, Robert C. Burruss, Robert H. Byrne, Jon Chorover, George Cooper, Christopher J. Daughney, James Farquhar, Jérôme Gaillardet, Susan Glasauer, Jessica N. Gorham, Johnson R. Haas, H. Roger Harvey, George R. Helz, Sydney R. Hemming, Peter Hodge, Gregory F. Herzog, Jurgi Horita, Shiuh-Min Huang, Trevor Ireland, Jun-ichiro Ishibashi, Karin Johannesson, Clark Johnson, Christopher S. Kim, Christian Koeberl, Stephen M. Kraemer, S. Krishnaswami, Alexander N. Krot, Graham A. Logan, Boaz Luz, Timothy J. Lyons, Michael L. Machesky, Tom McCollom, James McManus, Anders Meibom, Jack J. Middelburg, Frederic Moynier, Alfonso Mucci, Bjorn Myhre, Hiroko Nagahara, Martin Novak, Peggy A. O'Day, Dimitri Papanastassiou, Mark Rehkämper, W. Uwe Reimold, Peter W. Reiners, Edward M. Ripley, Claire Rollion-Bard, Sara S. Russell, James Rustad, Edwin A. Schauble, Jacques Schott, Timothy J. Shaw, Steven B. Shirey, Jaap S. Sinninghe Damsté, Donald L. Sparks, Carl Steefel, Dmitri A. Sverjensky, Michael J. Taylor, Peter Ulmer, Derek Vance, David J. Vaughan, Richard J. Walker, Jörg Wijbrans, Roy A. Wogelius, Chen Zhu

Volume 87 June 15, 2012

Articles

Continued on outside back cover

This article appeared in a journal published by Elsevier. The attached copy is furnished to the author for internal non-commercial research and education use, including for instruction at the authors institution and sharing with colleagues.

Other uses, including reproduction and distribution, or selling or licensing copies, or posting to personal, institutional or third party websites are prohibited.

In most cases authors are permitted to post their version of the article (e.g. in Word or Tex form) to their personal website or institutional repository. Authors requiring further information regarding Elsevier's archiving and manuscript policies are encouraged to visit:

http://www.elsevier.com/copyright

Author's personal copy

Available online at www.sciencedirect.com

SciVerse ScienceDirect

Geochimica et Cosmochimica Acta 87 (2012) 81–116

Geochimica et Cosmochimica Acta

www.elsevier.com/locate/gca

Mineralogical and isotopic constraints on chondrule formation from shock wave thermal histories

Alexei V. Fedkin [a], Lawrence Grossman [a,b,*], Fred J. Ciesla [a], Steven B. Simon [a]

[a] Department of the Geophysical Sciences, The University of Chicago, 5734 South Ellis Avenue, Chicago, IL 60637, United States
[b] Enrico Fermi Institute, The University of Chicago, 5640 South Ellis Avenue, Chicago, IL 60637, United States

Received 28 September 2011; accepted in revised form 14 March 2012; available online 24 March 2012

Abstract

When a shock wave passes through a nebular gas, increasing water enrichment leads to higher temperatures and post-shock P^{tot}, but lower cooling rates. A kinetic evaporation model is developed for tracking the chemical and isotopic changes that would occur in a clump of chondrule precursor dust surrounded by nebular gas in a closed system traversed by a nebular shock wave, taking into account effects of non-equilibrium melting and fractional crystallization on the liquid composition and the temperature difference between the gas and the droplet. A range of shock wave temperature–pressure histories computed for systems enriched relative to solar composition by factors of 550 in water, to achieve the redox state of chondrules, and 600 in dust, to retard evaporation, are employed, and redox changes are assumed to occur on the time–scale of heating and cooling in each. Two different system compositions are assumed, with the mean Fe/Si ratios of Types I and II chondrules. Two different textural outcomes are modeled, PO, in which nuclei are preserved and olivine crystallization begins immediately upon reaching saturation, and BO, in which no nuclei are preserved and olivine crystallization begins only after 300–400 K of supersaturation. In all cases, all iron evaporates, regardless of its oxidation state, as well as alkalis and smaller fractions of Mg and Si. In most cases, recondensation occurs on the time-scale of cooling, resulting in droplets whose bulk compositions have small isotopic anomalies in Mg, Si and Fe, comparable to those seen in bulk chondrules. Because fractional crystallization of olivine occurs before recondensation is complete, however, large isotopic variations, especially for iron, would have been recorded both within olivine crystals and between olivine and glass within these objects. Even after diffusive relaxation during crystal growth and cooling, variations in δ^{25}Mg of several tenths of a ‰ to several ‰, in δ^{29}Si of 0.1‰ to several ‰ and in δ^{56}Fe of several ‰ would be measurable within large grains that grew throughout the olivine crystallization interval in many cases, and olivine-glass differences of $\geqslant$several tenths of a ‰ in δ^{29}Si, and of several ‰ in δ^{56}Fe would be preserved. Such internal isotopic heterogeneities have not yet been observed in chondrules, suggesting that the latter did not form in these shock wave thermal histories. Suppression of production of internal isotopic variations requires heating times that are shorter by a factor of 100, combined with dust enrichments $\geqslant 6 \times 10^4$ and/or $P^{tot} \geqslant 10^{-2}$ bar. Together with relatively high f_{O_2}, these constraints suggest that chondrules formed in clouds of liquid and vapor generated by impact on ice-rich planetesimals.
© 2012 Elsevier Ltd. All rights reserved.

1. INTRODUCTION

1.1. Physico-chemical conditions of chondrule formation

Chondrules are silicate-rich, glassy spherules that existed as independent liquid droplets in the solar nebula. The textures of porphyritic chondrules are reproduced in laboratory experiments by heating solid precursors to temperatures where some nuclei survive, either just below the liquidus, or above the liquidus for insufficient time to destroy all pre-existing nuclei (Hewins and Radomsky, 1990). Barred chondrules are produced when solid precursors are heated above the liquidus, and almost all pre-existing nuclei are destroyed (Hewins and Radomsky, 1990). Although a continuum of compositions exists between them, Types I and II chondrules are defined as having mean

* Corresponding author. Address: Enrico Fermi Institute, The University of Chicago, Chicago, IL 60637, United States.
E-mail address: yosi@uchicago.edu (L. Grossman).

0016-7037/$ - see front matter © 2012 Elsevier Ltd. All rights reserved.
http://dx.doi.org/10.1016/j.gca.2012.03.020

Author's personal copy

FeO/(FeO+MgO) atomic ratios <0.1 and ⩾0.1, respectively, in their olivine and pyroxene. The two types differ also in their total iron contents, with the mean Fe/Si ratios of Type Is being ~0.1 (Jones and Scott, 1989; Jones, 1994) and those of Type IIs ~0.34 (Jones, 1990, 1996), both relative to CI chondrites. The FeO contents of both types are important constraints on their origin, as they imply chemical communication with a gas whose log f_{O_2} was ~IW-1.3, *i.e.*, 1.3 log units below the f_{O_2} of the iron-wüstite (IW) buffer, about 5 log units more oxidizing than a system of solar composition (Grossman et al., 2008). In an attempt to understand why chondrules are so oxidized, models have been proposed in which excess water was added to chondrule-forming regions of the solar nebula by evaporation of ice from planetesimals that migrated inward from cold regions (*e.g.*, Ciesla and Cuzzi, 2006).

Low-fayalite cores in olivine phenocrysts in Type II chondrules (Jones, 1990) and dusty olivine grains in Type I chondrules (Jones, 1994) are interpreted as relict grains of solid precursors in which the oxidation state of iron differs from the bulk of the material in their host chondrules. Their presence suggests that at least partial oxidation of metallic iron and reduction of FeO occurred on the timescale of chondrule formation. Relict grains constitute *prima facie* evidence of incomplete equilibration of pre-existing solids with chondrule liquids, implying rapid heating. Experiments show that the cores of 50-μm-diameter olivine grains require >1 h to equilibrate with liquid of chondrule composition at a subliquidus temperature of 1823 K (Whattam and Hewins, 2009) and that superliquidus survival times of relict olivine correlate with grain size, with 20–45-μm-diameter grains persisting for up to 1 h (Hewins and Connolly, 1996). Chondrules in primitive chondrites exhibit extensive heterogeneity of olivine compositions both between and within grains. X_{Fa} increases from <0.1 to values >0.30 in the rims of individual crystals in Type II chondrules, *prima facie* evidence of fractional crystallization. For Type II porphyritic olivine (PO) chondrules in Semarkona, diffusion modeling of zoning profiles of olivine phenocrysts yields cooling rates of 5 to 1100 K/h, depending on the chondrule, in the temperature interval 1500–1900 K (Miyamoto et al., 2008), and diffusion modeling of relict forsterite gives a cooling rate that falls from ~400 K/h at 1873 K to ~135–275 K/h at 1273 K (Hewins et al., 2009).

Both Type I and, to a lesser extent, Type II chondrules are depleted relative to Si in elements more volatile than Si compared to CI chondrites (Jones et al., 2005). Such volatile element depletions are expected to result from evaporation when chondrule precursors are heated to near-liquidus temperatures in hydrogen-rich cosmic gases. Because this process would also produce heavy isotope enrichments in the fractions of the evaporated elements that remain in chondrule residues, however, a major problem in understanding the origin of chondrules is the absence from them of large isotopic mass-fractionations of moderately volatile elements. In an attempt to solve this problem, models have been proposed in which chondrule production occurred under conditions where Rayleigh fractionation of isotopes was suppressed, such as in regions enriched in condensable elements relative to the gas by factors of at least several hundred relative to solar abundances (*e.g.*, Alexander, 2004). Although Alexander (2004) employed experimentally derived evaporation rates, no attempt was made in that work to include the effects of non-equilibrium melting, fractional crystallization, redox change during melting, or a water-rich ambient gas on liquid composition.

1.2. Suitability of shock waves as a heat source for chondrules

Solar nebular shock waves are among the leading candidates for the heat source needed for production of chondrules (Ciesla, 2005). Investigations of the thermal history of chondrule precursors heated by nebular shock waves have included the effects of gas drag and radiation from other chondrules on chondrule heating rates, the effect of chondrule enrichment on heating and cooling rates, and the effect of the post-shock cooling rate of the surrounding gas on cooling rates of chondrules. These studies demonstrated that the resulting thermal evolution of condensed matter is consistent with the rapid heating, peak temperatures and rapid cooling deduced for chondrule formation from chondrule properties and laboratory experiments (Hood and Horanyi, 1991, 1993; Iida et al., 2001; Desch and Connolly, 2002; Ciesla and Hood, 2002; Ciesla et al., 2003). Systems investigated so far have been solar in composition except for the dust enrichments, but the oxidation state and isotopic compositions of chondrules require both dust and water enrichments.

1.3. Purposes of this study

The first objective of the present work is to investigate the pressure–temperature conditions to which chondrule precursors would be subjected during passage of shock waves through nebular systems enriched simultaneously in dust and water relative to solar composition. The second objective is to model the evolution of the mineralogical, chemical and isotopic compositions of chondrule precursors subjected to such conditions to see if the resulting properties match those of observed chondrules. Preliminary versions of this work appeared in Fedkin et al. (2008, 2011).

2. PROPERTIES OF CHONDRULES

Electron microprobe analyses were performed to establish the typical shapes of fayalite histograms and mesostasis compositions for individual Types I and II PO chondrules. Techniques employed and results obtained are given in Appendix A.

2.1. Isotopic compositions of chondrules

Isotopic mass-fractionations observed in chondrules are quite small. Magnesium isotopic compositions of Allende chondrules were measured by Galy et al. (2000) and Young et al. (2002) against the SRM980_O standard, and of Allende, Murchison and Murray chondrules by Bizzarro et al. (2004) and Bouvier et al. (2009) against the DSM3 standard. Because Galy et al. (2003) found that SRM980_O

Author's personal copy

has a mean δ^{25}Mg of −1.78‰ when measured against DSM3, the Galy et al. (2000) and Young et al. (2002) data were corrected according to $(\delta^{25}\mathrm{Mg})_{DSM3} = (\delta^{25}\mathrm{Mg})_{SRM980\_O} - 1.78$. Because Bouvier et al. (2009) found that whole carbonaceous chondrites have a mean δ^{25}Mg of -0.14 ± 0.09 relative to DSM3, all chondrule data were renormalized to mean solar system matter (ss) according to $(\delta^{25}\mathrm{Mg})_{ss} = (\delta^{25}\mathrm{Mg})_{DSM3} + 0.14$. While Galy et al. (2000), Bizzarro et al. (2004) and Bouvier et al. (2009) analysed whole chondrules, Young et al. (2002) performed multiple analyses of individual spots within chondrules by laser ablation. A simple average was made of all spots within each chondrule measured by Young et al. (2002), and all data from the three studies are plotted on Fig. 1a, from which it can be seen that δ^{25}Mg varies from −0.6 to + 1.0‰ in individual chondrules, with a slight bias toward positive values. No significant difference in δ^{25}Mg can be discerned between PO and barred olivine (BO) or between Types I and II chondrules.

The only Si isotopic data for individual chondrules from carbonaceous and ordinary chondrites are those reported by Clayton et al. (1983, 1991), Georg et al. (2007), Hezel et al. (2010) and Armytage et al. (2012). These were measured relative to NBS-28 but have been renormalized relative to mean solar system matter according to $(\delta^{29}\mathrm{Si})_{ss} = (\delta^{29}\mathrm{Si})_{NBS-28} + 0.275$, as in Grossman et al. (2000). For chondrules studied by Clayton et al. (1983, 1991), those with bulk FeO contents $\leqslant 8$ wt.% were reclassified as Type I and those with FeO > 8 wt.% as Type II. The data are plotted in Fig. 1b. Almost all of the chondrules have δ^{29}Si within ±0.4‰ of average solar system matter and are approximately evenly distributed about $\delta^{29}\mathrm{Si} = 0$. The Si isotopic compositions of Type I chondrules are indistinguishable from those of Type IIs, as are those of BO from PO chondrules.

Shown in Fig. 1c are K isotopic compositions measured for an Allende chondrule by Humayun and Clayton (1995) and in individual chondrules from the Bishunpur L/LL3.1 chondrite (Alexander et al., 2000) and Semarkona (Alexander and Grossman, 2005). In the latter two studies, chondrules were found to be internally heterogeneous in K isotopic composition, so a mean for each chondrule was obtained by weighting the different analyses from each by the inverse square of their 1σ uncertainties. Humayun and Clayton (1995) found that the average K isotopic composition of chondrites was indistinguishable from their chemical standard and that the average K isotopic composition of terrestrial materials was nearly so. Because Alexander et al. (2000) and Alexander and Grossman (2005) used a terrestrial basalt glass standard, all data in Fig. 1c are assumed to be relative to mean solar system matter. The chondrules range in δ^{41}K from −5.5 to + 12‰, with more positive than negative values and a mean of +1.5‰. Almost all Type II chondrules have positive δ^{41}K, while Type Is are more evenly distributed about normal K. This is particularly true of the porphyritic chondrules.

Literature data for the Fe isotopic compositions of individual chondrules from carbonaceous and ordinary chondrites are plotted in Fig. 1d. The data of Mullane et al. (2005), Zhu et al. (2001) and Hezel et al. (2010) were reported relative to the IRMM-014 standard and those of Kehm et al. (2003) relative to the Kil1919 standard. Because IRMM-014 has an Fe isotopic composition very close to that of mean solar system matter (Dauphas and Rouxel, 2005), the Kehm et al. (2003) data were re-normalized to IRMM according to $(\delta^{56}\mathrm{Fe})_{IRMM} = (\delta^{56}\mathrm{Fe})_{Kil1919} + 0.078$ (Dauphas and Rouxel, 2005). All of the chondrules have δ^{56}Fe within ±1.0‰ of that of mean solar system matter, and are close to normally distributed about $\delta^{56}\mathrm{Fe} = 0$. Little difference in δ^{56}Fe can be discerned between Type I and Type II chondrules, nor between porphyritic and barred chondrules.

3. THERMAL EVOLUTION IN WATER-RICH SHOCK WAVES

3.1. General considerations

All thermal histories used herein were calculated using the model described by Ciesla et al. (2003), which allows the nebular water abundance to be varied. Specifically, the gas is treated as being composed of 4 species (H_2, H, He, and H_2O), each of which is described by a similar set of equations describing mass, energy, and momentum conservation (see review by Desch et al., 2005). The approach of Desch and Connolly (2002) is used to calculate a mass-weighted average gamma (ratio of heat capacity at constant pressure to that at constant volume) for these molecules to determine the changes in fluid properties across the shock front.

Due to the high mass density of water and chondrule precursors considered here, the spatial resolution of the shock model was increased relative to previous published studies, to account for the large optical depth that must be modeled. That is, in models such as those presented by Desch and Connolly (2002) and Ciesla and Hood (2002), chondrule properties were recorded at distance intervals of ~100 km, thus defining their evolution throughout the shock. Here, the spatial resolution was chosen such that the optical depth from one grid point to the next did not exceed 0.001. This resulted in spatial resolutions of ~1 km in many runs due to the high densities of materials considered.

In all cases, solids were assumed to be present as 1 mm-diameter silicate spheres with densities of 3.3 g/cm^3. The heat capacity of the chondrules was taken to be 10^7 erg/g/K and the latent heat of melting as 4.5×10^9 erg/g. To account for the fact that chondrules are not pure substances, and thus melt over a range of temperatures, the latent heat of melting was spread across a temperature range of 1400–1900 K, in essence increasing the effective heat capacity over that temperature range (Desch and Connolly, 2002; Ciesla et al., 2003). The solar solid/gas mass ratio was taken to be 0.005 and the solar H_2O/H_2 molecular ratio was taken to be 5×10^{-4} (Fedkin and Grossman, 2006).

In the present work, all dust is assumed to be processed into chondrules, and a greater initial amount of dust is assumed to lead to a greater chondrule number density. Consequently, the terms "dust" and "chondrule precursors" are used interchangeably, as are "dust enrichment"

Author's personal copy

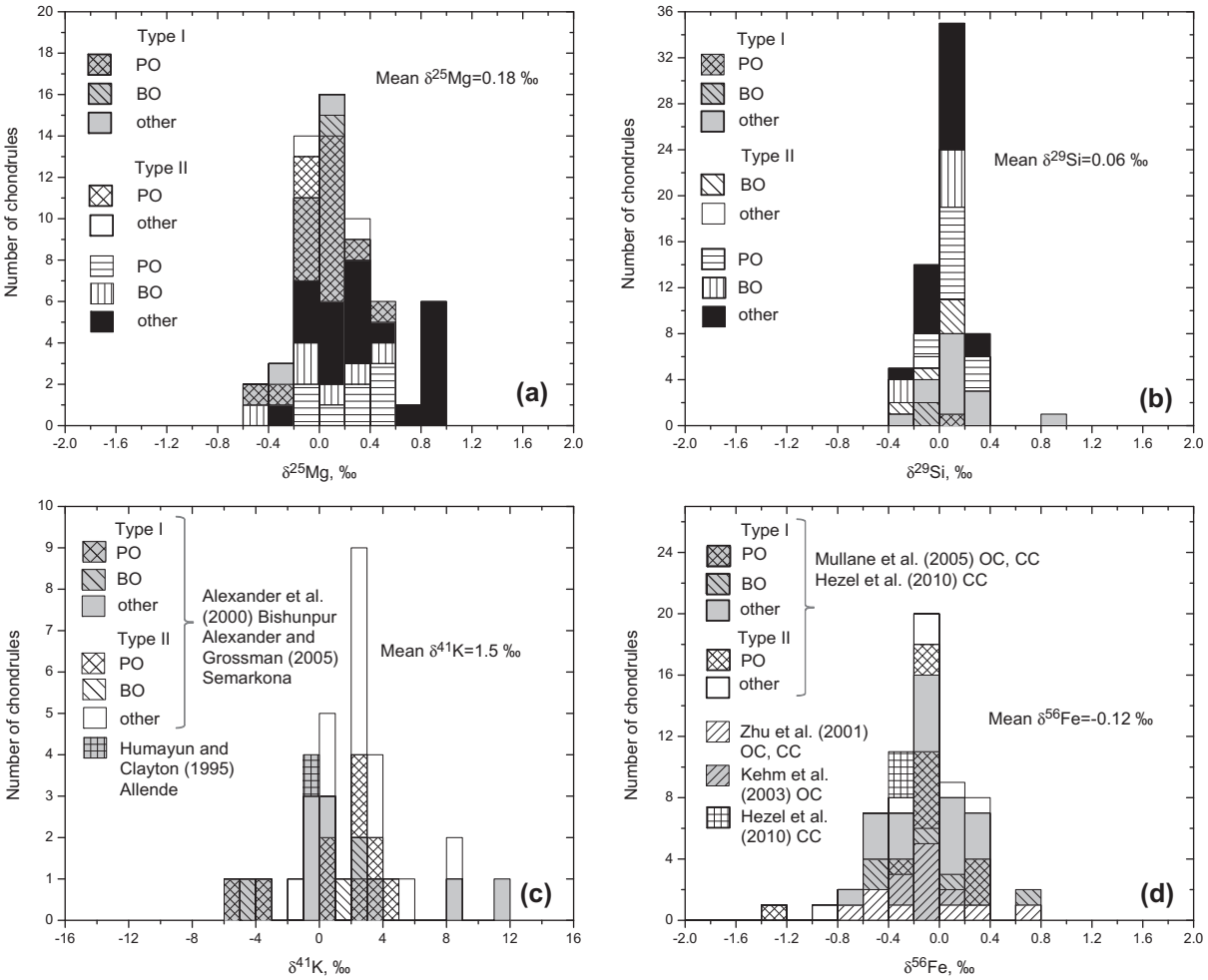

Fig. 1. (a) Magnesium isotopic compositions of individual chondrules from carbonaceous chondrites, as reported by Galy et al. (2000), Young et al. (2002), Bizzarro et al. (2004) and Bouvier et al. (2009) renormalized to mean solar system matter. (b) Silicon isotopic compositions of individual chondrules from carbonaceous and ordinary chondrites, as reported by Clayton et al. (1983, 1991), Georg et al. (2007), Hezel et al. (2010) and Armytage et al. (2012) renormalized relative to mean solar system matter. (c) Potassium isotopic compositions of chondrules from Allende, Bishunpur, and Semarkona. (d) Iron isotopic compositions of individual chondrules from carbonaceous (CC) and ordinary (OC) chondrites, as reported in the literature relative or renormalized to the IRMM-014 standard, indistinguishable from mean solar system matter. PO: porphyritic olivine; BO: barred olivine; Other: chemical and/or textural types are either unknown or different from the labeled types.

and "chondrule enrichment". Based on the parameter space explored here, the following generalizations arise from the shock wave models considered (Fig. 2). The thermal histories are characterized by an initial period with a near-linear, relatively low heating rate of chondrule precursors due to their absorption of radiation propagating upstream of the shock and emitted by the hot chondrules behind the shock front. This period ends at what is referred to herein as the "pre-shock temperature", that of the warmed chondrules as they cross the shock front. This is followed by a very short period at the time of shock passage when the temperature spikes sharply upward to the peak temperature and then sharply downward, reaching a value referred to herein as the "inflection temperature". This is followed by a long period of near-linear, relatively slow cooling. During the temperature spike, the gas is heated to a temperature several thousand degrees higher than the droplet and cooled back to ~2500 K, all in only a few minutes. During the pre-shock period, P^{tot} and, consequently, P_H^{tot}, rise logarithmically with time, spike sharply upward at the time of shock passage, then slightly downward, and are nearly constant during the post-shock period. Decreasing chondrule size while holding the chondrule abundance and all other factors constant increases heating and cooling rates (Fig. 2a) but has a minimal effect on evolution of P^{tot} (Fig. 3a). Everything else being equal, greater shock velocities result in higher post-shock gas temperatures and densities, leading to higher temperatures of chondrule precursors, more rapid cooling rates (Fig. 2b) and higher post-shock total pressures (Fig. 3b). All other things being equal, a slightly greater initial pressure leads to a higher post-shock density, which leads to much higher peak and inflection temperatures, more rapid cooling and higher post-shock total pressures (Figs. 2b and 3b). When all other

Author's personal copy

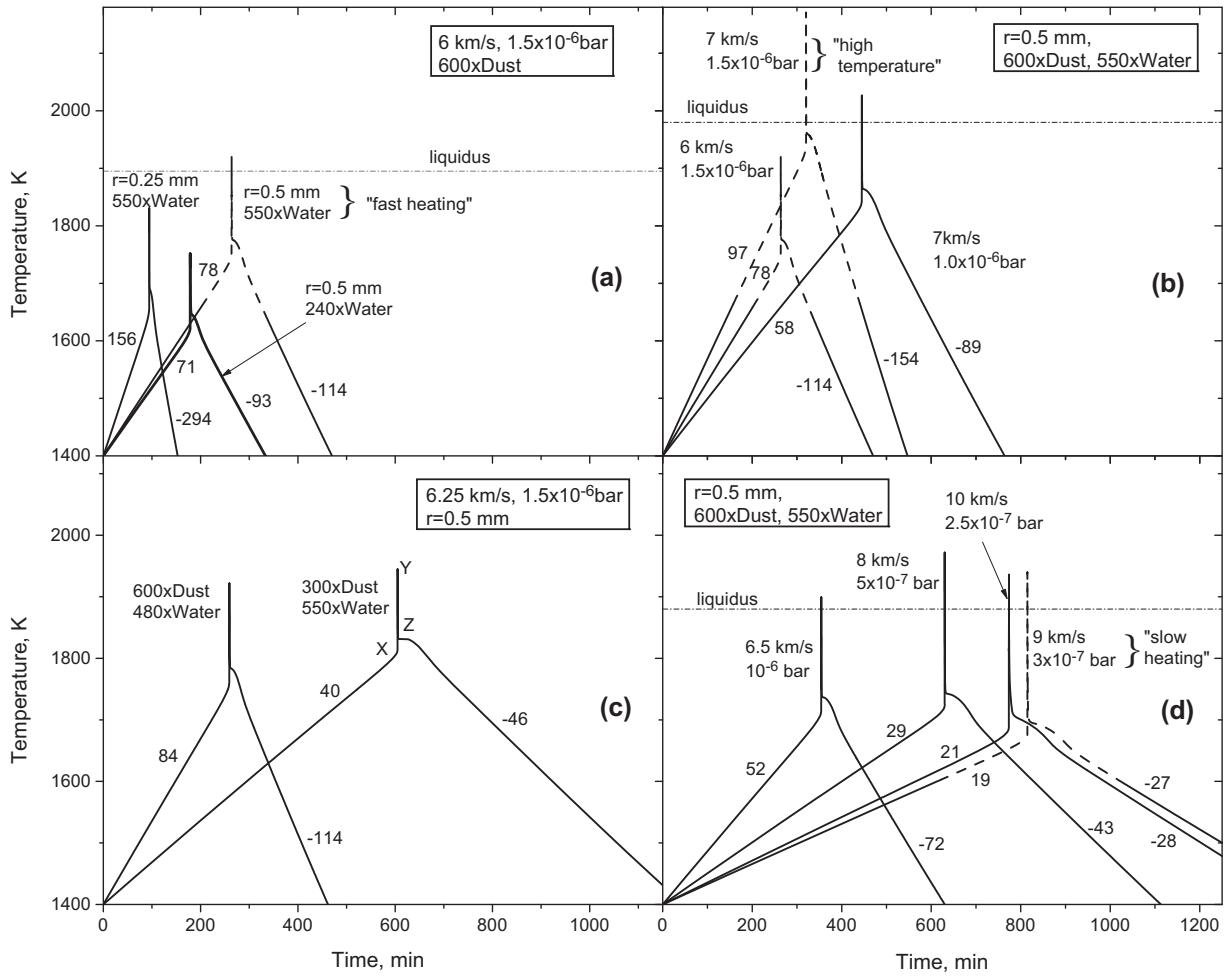

Fig. 2. Effects on computed time-dependence of protochondrule temperature accompanying passage of nebular shock waves due to changes in (a) chondrule radius, r, and water enrichment; (b) shock velocity and P^{tot}; (c) simultaneous variations in dust and water enrichment; and (d) simultaneous variations in shock velocity and P^{tot}. In all panels, time-zero is defined as the time when the temperature reaches 1400 K. Linear portions of the thermal histories are labeled with their heating and cooling rates in K/hr. On one of the curves in (c), the following inflection points characteristic of all thermal histories discussed herein are defined: X-the pre-shock temperature; Y-the peak temperature; and Z-the inflection temperature. For the 0.5 mm, 550x water case in (a), the "fast heating' profile in this work; the 7 km/s, 1.5×10^{-6} bar case in (b), the "high temperature" profile; and the 9 km/s case in (d), the "slow heating" profile; dashed segments of the thermal histories indicate intervals where the protochondrules contain no FeO, and were thus modeled as CMAS systems. Liquidus temperatures are the temperatures of disappearance of olivine for the same cases.

factors are held constant, higher chondrule densities lead to higher pre-shock, inflection and peak temperatures, higher heating and cooling rates, and higher post-shock pressures.

3.2. Water concentration

The effect of water concentration on shock wave thermal histories was investigated in the present work for the first time. In a gas of solar composition, the H_2O/H_2 molecular ratio varies with temperature and averages $\sim 5 \times 10^{-4}$ (Fedkin and Grossman, 2006). At constant pressure and temperature, increasing the water concentration by simple addition of water molecules reduces the concentrations of other species, most of which are H_2 and He. Because of the relatively high molecular weight of water, this increases the gas mass density. As a result, when chondrule precursors move through the gas immediately behind the shock front, the collisions they experience are more energetic, causing higher peak and inflection temperatures (Fig. 2a). Furthermore, the increase in water concentration results in the gas having higher heat content, requiring the system to radiate away more energy to cool. Although this would tend to decrease the cooling rates of solids, there is a competing effect. The increased gas density due to higher water content results in a greater spatial concentration of chondrules in the post-shock region that, as seen above, leads to higher cooling rates. For the combinations of dust and water enrichments investigated here, the latter effect more than offsets the former, causing the cooling rates of solids processed in a shock wave to increase when the water concentration increases, when all other factors are held constant (Fig. 2a). The higher inflection temperatures resulting from increasing water enrichment also lead to higher post-shock total pressures (Fig. 3a).

Author's personal copy

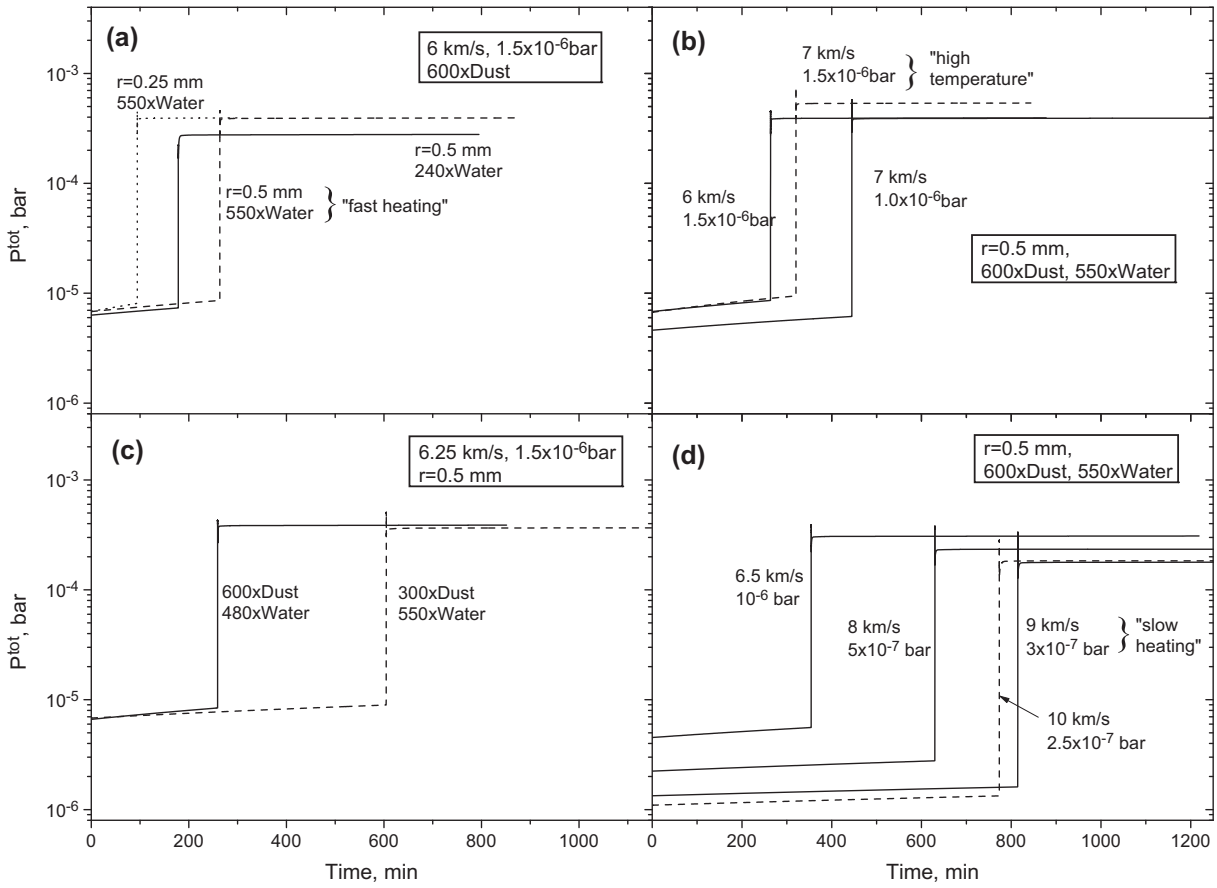

Fig. 3. Effects on computed time-dependence of ambient total pressure, P^{tot}, for the shock wave thermal histories shown in Fig. 2. In all panels, time-zero is defined as in Fig. 2.

This model does not account for cooling of the gas *via* line emission from the water molecules. This issue was examined by Iida et al. (2001) and Miura and Nakamoto (2006) who used the analytic expressions of Neufeld and Kaufman (1993) to estimate how much energy was lost from the post-shock gas as a function of temperature, water abundance and distance from the shock front. In most cases, they found that inclusion of this effect led to very rapid cooling of the gas, increasing the cooling rates of the chondrules to $> 10^4$ K/hr, which is much greater than the cooling rates predicted when that effect is neglected (*e.g.*, Desch and Connolly, 2002; Ciesla and Hood, 2002).

Morris et al. (2009a) extended the work of Neufeld and Kaufman (1993) by considering the cooling effects of 1.2 million emission lines from the water molecule. They found that, while cooling can still be efficient as a result of these lines, high dust densities significantly slow the rate of energy loss. Preliminary calculations incorporating this effect into a full chondrule shock heating model suggest that cooling rates during crystallization will likely be increased by a total of ~10 K/hr (Morris et al., 2009b; Morris and Desch, 2010). Such an increase is small given other uncertainties in the model, and is ignored here for simplicity.

Line cooling may have a more significant effect right around the shock front where gas temperatures significantly exceed those of the chondrules. Morris et al. (2009a) found that radiation from immediately behind the shock front may escape more readily due to line cooling, resulting in more rapid cooling of the gas; however, this cooling may be slowed as a result of the high dust densities considered here. The temperatures predicted here would likely result also in dissociation of water molecules, whose effect on cooling rate has not been considered. The time that chondrules spend in this region is very small compared to the overall time of interest, and it is assumed that these effects would not greatly impact the present results.

Next, the chemical and isotopic evolution of chondrule precursors is explored as they are overrun by nebular shock waves of the type described above. Note that while the solids undergo vaporization and recondensation of some elements, effects of these processes are not considered in the energy balance of the solid particles or the gas evolution in the thermal model for shock processing. While a fully coupled physical and chemical model would be ideal, the computational demands of such a study prohibit it.

4. CHEMICAL MODELING TECHNIQUE

4.1. Thermodynamic state of the condensed assemblage

Several major improvements over the method employed by Fedkin et al. (2006) are incorporated into the method described herein. In this work, only equilibrium vapor pressures and actual ambient pressures are calculated,

Author's personal copy

eliminating the use of P^{drop} and P^{gas}; treatment of oxygen as an independent component eliminates the necessity of calculating virtual and actual assemblages; and the temperature difference between the ambient gas and the condensed assemblage is taken into account for the first time.

The total system is assumed to consist of the following 17 elements: H, He, C, N, O, Na, Mg, Al, Si, P, S, K, Ca, Ti, Cr, Fe and Ni. Of these, the condensed assemblage is assumed to contain all but H, He, C, N, S and P. The computational engine is the MELTS thermodynamic model of Ghiorso and Sack (1995). The bulk chemical composition, temperature and pressure of a condensed system uniquely determine its equilibrium phase assemblage. The MELTS model is used to determine the equilibrium assemblage by iterating on f_{O_2} until an assemblage is found whose oxygen content matches that of the condensed assemblage. This yields the equilibrium weight and volume proportions of solid and liquid silicate, metal and oxide phases, their individual compositions and the activities of all components. The equilibrium f_{O_2} at which the assemblage is computed is also the equilibrium vapor pressure of $O_{2(g)}$ for the assemblage.

4.2. Calculation of equilibrium vapor pressures

To calculate the equilibrium vapor pressures of all other molecules, the speciation of the gas phase that would be in equilibrium with the condensed assemblage, hereafter referred to as the droplet, is computed at the temperature of the droplet. For each element in the droplet, the vapor pressure of the monatomic species is determined first, from such relations as

$$P_O = \sqrt{K_1 f_{O_2}}, \tag{1}$$

$$P_{Si} = K_2 a_{SiO_2}/f_{O_2} \tag{2}$$

$$P_{Na} = \sqrt{\frac{K_3 a_{Na_2SiO_3}}{a_{SiO_2} P_O}} \tag{3}$$

where K_1, K_2 and K_3 are the equilibrium constants for the reactions,

$$O_{2(g)} \Longleftrightarrow 2O_{(g)}, \tag{4}$$

$$SiO_{2(l)} \Longleftrightarrow Si_{(g)} + O_{2(g)} \tag{5}$$

$$\text{and } Na_2SiO_{3(l)} \Longleftrightarrow 2Na_{(g)} + SiO_{2(l)} + O_{(g)}, \tag{6}$$

respectively, and a_{SiO_2} and $a_{Na_2SiO_3}$ are the activities of SiO_2 and Na_2SiO_3, respectively, in the liquid phase.

The gas-phase speciation of the system is described by a set of 17 mass-balance equations, one for each element i. In each such equation, the sum of the partial pressures of all species of element i, multiplied by their respective stoichiometric coefficients, is defined as P_i^{tot}. In all calculations, P_H^{tot} is an input parameter. For all other elements entirely in the gas phase, *i.e.*, He, C, N, P and S,

$$P_i^{tot} = A(i)P_H^{tot}/A(H), \tag{7}$$

where $A(i)$ and $A(H)$ are the relative atomic abundances of elements i and H, respectively. For each of the other elements, those whose vapor pressures were determined as in the previous paragraph, P_i^{tot} is a dependent variable. Examples of mass-balance equations for elements entirely in the gas phase are those for hydrogen,

$$2P_{H_2} + 2P_{H_2O} + P_H + \ldots = P_H^{tot} \tag{8}$$

$$\text{and sulfur,} \quad P_{H_2S} + P_{SiS} + \ldots = P_S^{tot}, \tag{9}$$

$$\text{that become} \quad K_4 P_H^2 + K_5 P_H^2 P_O + P_H = P_H^{tot} \tag{10}$$

$$\text{and } K_6 P_H^2 P_S + K_7 P_{Si} P_S = P_S^{tot}, \tag{11}$$

respectively, where K_4, K_5, K_6 and K_7 are the equilibrium constants for the reactions,

$$2H_{(g)} \Longleftrightarrow H_{2(g)}, \tag{12}$$

$$2H_{(g)} + O_{(g)} \Longleftrightarrow H_2O_{(g)}, \tag{13}$$

$$2H_{(g)} + S_{(g)} \Longleftrightarrow H_2S_{(g)} \tag{14}$$

$$\text{and } Si_{(g)} + S_{(g)} \Longleftrightarrow SiS_{(g)}, \tag{15}$$

respectively. As illustrated by Eqs. (10) and (11), wherein P_O and P_{Si} are uniquely determined by the condensed phase assemblage, the mass-balance equation for each element i entirely in the gas phase introduces only one additional variable, the partial pressure of its monatomic species, P_i. After substitution of the value determined for P_i for each of the elements that do enter the condensed phase assemblage, a Newton–Raphson method is used to solve, to one part in 2×10^{15}, the resulting system of 6 simultaneous non-linear mass-balance equations for P_i for each of the elements that do not enter the condensed phase. When all P_i are known, the partial pressures of all other species in the vapor that would be in equilibrium with the droplet are calculated simply using the equilibrium constants for their formation from their monatomic gaseous constituents. The 156 gaseous species carried in the present calculations are listed in Table 1. All thermodynamic data are from Chase (1998), except for several corrections as discussed by Fedkin and Grossman (2006).

In the thermal histories investigated in this work, the droplet experiences total evaporation of Na and K early in the heating stage and total loss of Fe, regardless of its oxidation state, before reaching peak temperature. At that point, the condensed assemblage consists only of CaO, MgO, Al_2O_3, SiO_2, (CMAS) and minor TiO_2 and Cr_2O_3, and cannot be modeled accurately with MELTS (Fedkin et al., 2006). After the FeO content of the liquid falls to <0.3 wt.%, computation of the subsequent evaporation history is done by transferring all Ti, Cr and the remaining Fe into the gas, and calculating vapor pressures as in the closed-system CMAS evaporation model of Grossman and Fedkin (2003) with one modification: oxide speciation in the vapor pressure calculation is assumed to be constrained entirely by the droplet, *i.e.*, $P_O^{tot} = P_O^{drop}$. To find when recondensation of iron begins, an equilibrium condensation calculation for a non-ideal, metallic nickel–iron alloy is performed in parallel with the CMAS calculation at each temperature step after reaching peak temperature. At the next temperature step below that where the alloy becomes stable, two silicate evaporation calculations are performed. One is a pure CMAS calculation. The other seeds all of the iron of the alloy, and nickel in chondritic proportion to it, into the same CMAS composition, oxidizes 50%

Author's personal copy

Table 1
Gas species included in the calculation.

Si	AlOH	CaS	C_2O	H_2N_2	NS
Si_2	AlS	Na	C_3O_2	H_2O	O
Si_3	Cr	Na_2	CH	H_2O_2	O_2
SiC	CrN	NaCN	CH_2	HO_2	O_3
SiC_2	CrO	$(NaCN)_2$	CH_3	H_2P	OH
Si_2C	CrO_2	NaH	CH_4	HS	P
SiH	CrO_3	NaO	C_2H	H_2S	P_2
SiH_4	Fe	NaOH	C_2H_2	H_2SO_4	P_4
SiN	FeO	$(NaOH)_2$	C_2H_4	He	PH
Si_2N	$Fe(OH)_2$	Na_2SO_4	C_2H_4O	N	PH_3
SiO	FeS	K	CHNO	N_2	PO
SiO_2	Mg	K_2	CHO	N_3	PO_2
SiS	Mg_2	KCN	CHP	NH	PS
Ti	MgH	$(KCN)_2$	CN	NH_3	P_4S_3
TiO	MgN	$(KOH)_2$	CN_2	N_2H_4	S
TiO_2	MgO	KH	CNO	NO	S_2
Al	MgOH	KO	CO	NO_2	S_3
Al_2	$Mg(OH)_2$	KOH	CO_2	NO_3	S_4
AlC	MgS	K_2SO_4	COS	N_2O	S_5
AlH	Ni	C	CP	N_2O_3	S_6
AlN	NiS	C_2	CS	N_2O_4	S_7
AlO	Ca	C_3	CS_2	N_2O_5	S_8
AlO_2	Ca_2	C_4	H	NOH	SO
Al_2O	CaO	C_5	H_2	NO_2H	SO_2
Al_2O_2	CaOH	C_2N_2	HCN	NO_3H	SO_3
AlO_2H	$Ca(OH)_2$	C_2N	H_2N	NP	S_2O

of the added iron, uses MELTS to find the equilibrium f_{O_2} of the resulting assemblage and calculates the flux of iron across the droplet-gas interface. If iron evaporates, the pure CMAS calculation is retained, and the process is repeated at the next temperature step. At the first temperature step where iron does not evaporate, the pure CMAS calculation is abandoned and evolution of the droplet upon further cooling is modeled with MELTS.

4.3. Calculation of partial pressures in the ambient gas

Using the actual relative atomic abundances of the same 17 elements as above to calculate all P_i^{tot}, the partial pressures of the same 156 molecular species are calculated by solving a system of 17 mass-balance equations *via* the Newton–Raphson method at the temperature of the ambient gas. Because none of the partial pressures are constrained to be in equilibrium with the droplet in this calculation, the resulting molecular speciation is that which would exist in the absence of the droplet or any other condensed phase.

4.4. Calculation of liquid–gas equilibration rates

The net flux, J_i, of a gaseous species i, in moles cm^{-2} sec^{-1}, across the droplet-gas interface is expressed as the difference between an evaporation rate and a condensation rate in the Hertz-Knudsen equation,

$$J_i = \left[\frac{\gamma_i^e P_i^v}{\sqrt{2\pi M_i R T_d}} - \frac{\gamma_i^c P_i^a}{\sqrt{2\pi M_i R T_g}}\right], \tag{16}$$

where M_i, γ_i^e, γ_i^c, P_i^v and P_i^a are the molecular weight, evaporation coefficient, condensation coefficient, equilibrium vapor pressure and ambient pressure of i, respectively, and R is the gas constant. When the temperature of the condensed assemblage, T_d, differs from that of the ambient gas, T_g, γ_i^e and P_i^v are evaluated at T_d, and P_i^a at T_g. Marcus et al. (2010) used transition state theory to reason that γ_i^c should be evaluated at T_g when i condenses into a liquid phase and at T_d when condensing into a solid phase, and this formulation is adopted in the present work. The rate of mass transfer, J_i, between condensed and vapor phases is seen to be directly dependent upon two parameters that are computed from thermodynamics only, P_i^v and P_i^a, and two others, γ_i^e and γ_i^c, that must be determined experimentally and within which lies the kinetic information. To calculate the total evaporation rate, J_j^t, of any element j, the evaporation rate of each species of that element, as given by Eq. (16), must be multiplied by a stoichiometric coefficient, υ_i, and then summed together with the evaporation rates of all other species of that element, as in

$$J_j^t = \sum_i \upsilon_i \left[\frac{\gamma_i^e P_i^v}{\sqrt{2\pi M_i R T_d}} - \frac{\gamma_i^c P_i^a}{\sqrt{2\pi M_i R T_g}}\right]. \tag{17}$$

In this work, the total fluxes of Al, Ca, Ti and Cr are assumed to be zero.

4.5. Evaporation coefficients and isotopic fractionation factors

Sources of data and assumptions made in employing them in the present work are found in Appendix B for evaporation coefficients and Appendix C for isotopic fractionation factors.

4.6. Redox equilibration

In the above treatment, when a cation evaporates from the silicate liquid, it is accompanied by an amount of oxygen in stoichiometric proportion to it in its liquid oxide component, regardless of the identity of the dominant evaporating gas species of that cation. Hence, there is a stoichiometric flux of oxygen, J_O^{stoich}, defined as

$$J_O^{stoich} = 0.5J_{Na}^t + J_{Mg}^t + J_{Fe}^{ts} + 2J_{Si}^t + ..., \tag{18}$$

where J_{Fe}^{ts} refers only to the flux of iron from the silicate liquid. There is also a total flux of iron from solid and liquid metallic iron alloys, J_{Fe}^{tm}. Because of the different evaporation coefficients of Fe from silicate and metal, and the changing relative surface areas of these phases during heating and evaporation, the FeO/Fe^o activity ratio of the assemblage and thus, the equilibrium f_{O_2}, change during evaporation. When the equilibrium f_{O_2} of the droplet is different from the f_{O_2} of the ambient gas, there is a driving force for transfer across the droplet-gas interface of additional oxygen, unaccompanied by cations of elements in the droplet. This results in an additional redox flux of oxygen, J_O^{red}, such that

$$J_O^t = J_O^{stoich} + J_O^{red}. \tag{19}$$

In this work, J_O^{red} is defined as

Author's personal copy

$$J_{\mathrm{O}}^{\mathrm{red}} = \frac{\gamma_O}{\sqrt{2\pi R}}\left[\frac{1}{\sqrt{M_{\mathrm{H_2O}}}}\left(\frac{P^v_{\mathrm{H_2O}}}{\sqrt{T_d}} - \frac{P^a_{\mathrm{H_2O}}}{\sqrt{T_g}}\right) + \frac{1}{\sqrt{M_O}}\left(\frac{P^v_O}{\sqrt{T_d}} - \frac{P^a_O}{\sqrt{T_g}}\right) + \frac{2}{\sqrt{M_{\mathrm{O_2}}}}\left(\frac{f_{\mathrm{O_2}}}{\sqrt{T_d}} - \frac{f^a_{\mathrm{O_2}}}{\sqrt{T_g}}\right) + \ldots\right], \quad (20)$$

in which there is a term for each oxygen-bearing gaseous species that does not also contain a condensable cation. In all cases investigated in this study, the water term is more than an order of magnitude larger than all other terms in Eq. (20), and this term is correlated with the $f_{\mathrm{O_2}}$ term. Thus, when $f_{\mathrm{O_2}}/\sqrt{T_d} > f^a_{\mathrm{O_2}}/\sqrt{T_g}$, oxygen evaporation occurs. When $f_{\mathrm{O_2}}/\sqrt{T_d} < f^a_{\mathrm{O_2}}/\sqrt{T_g}$, condensation of oxygen occurs. In this way, reduction of $\mathrm{FeO_{(l)}}$ is modeled as oxygen evaporation, and oxidation of metallic iron as oxygen condensation.

Low-fayalite cores and dusty olivine grains in chondrules indicate that the oxidation state of iron changed on the time-scale of chondrule formation. The purpose of the above formulation for $J_{\mathrm{O}}^{\mathrm{red}}$ is not to propose a model for the mechanism of redox processes in silicate melt + metallic nickel–iron systems exposed to water-rich cosmic gases, but rather to obtain a computationally tractable algorithm that yields an oxidation rate of metallic nickel–iron that occurs on the time-scale of the evolution of protochondrule material processed in nebular shock waves, assuming that this is the same as the chondrule evolution time-scale. The objective is to account for the effect of this process on the chemical composition of the silicate liquid so that evaporation rates from the liquid can be modeled more accurately than if oxidation were ignored. Setting γ_O=0.3 at 2000 K and giving it the same $1/T$ dependence as ln γ^e_{SiO} ensures that the oxidation state of iron changes on the time-scales of chondrule melting explored in this work.

4.7. Compositions of chondrule precursors

The chondrule precursors are assumed to contain enough mass to yield a spherical droplet of initial radius ~0.5 mm when equilibrated at the initial temperature of 1400 K. Initially, they contain chondritic proportions of Na, Mg, Al, Si, K, Ca, Ti and Cr, but S/Si, Fe/Si and Ni/Si are all 0.1, relative to CI chondrites, for the Type I precursors and 0.33 for the Type II precursors. The ambient gas contains none of these elements initially but does contain 100% of each of the H, He, C, N and P in the system, implying that they did not condense into the dust, and eventually contains 100% of the S, implying that it was totally volatilized prior to the precursor reaching its initial temperature. The initial partitioning of oxygen is determined by the $f_{\mathrm{O_2}}$ at which the precursor is assumed to have equilibrated at the starting temperature. Ideally, that log $f_{\mathrm{O_2}}$ should be less than ~IW-6.0, to simulate formation conditions of low-temperature, solar nebular condensates (Fedkin and Grossman, 2006) but this yields vanishingly small amounts of FeO. When an initial log $f_{\mathrm{O_2}}$ of IW-2.6 is assumed instead, Types I and II precursors begin with nonzero but minimal FeO contents. Initial bulk chemical and mineralogical compositions of the droplet, as well as the chemical compositions of the phases present in the assumed chondrule precursors, are shown in Table 2.

Table 2
Chemical compositions of both assumed chondrule precursors, and their equilibrium mineral assemblages at 1400 K and log$f$O$_2$ = IW-2.6.

Type I					Type II				
Bulk chem. comp.		Mineralogical composition			Bulk chem. comp.		Mineralogical composition		
Oxide	wt.%		wt.%		Oxide	wt.%		wt.%	
SiO_2	49.9	Alloy	2	$X_{Ni} = 0.11$	SiO_2	45.2	Alloy	11	$X_{Ni} = 0.06$
TiO_2	0.16	Olivine	43	$X_{Fa} = 0.04$	TiO_2	0.14	Olivine	40	$X_{Fa} = 0.04$
Al_2O_3	3.59	Opx	30	$X_{Fs} = 0.04$	Al_2O_3	3.26	Opx	27	$X_{Fs} = 0.04$
Cr_2O_3	0.85	Cpx	6	$X_{Di} = 0.72$, $X_{En} = 0.17$	Cr_2O_3	0.77	Cpx	5	$X_{Di} = 0.72$, $X_{En} = 0.17$
FeO	2.95	Spinel	2	$X_{Chr} = 0.72$	FeO	2.76	Spinel	1	$X_{Chr} = 0.72$
MgO	36.0	Feldspar	6	$X_{Ab} = 0.61$	MgO	32.6	Feldspar	6	$X_{Ab} = 0.61$
NiO	0	Sil. Liq.	11	SiO_2 67.3, TiO_2 0.79, Al_2O_3 12.2, Cr_2O_3 0.045, FeO 0.32, MgO 4.0, NiO 0.0, CaO 5.1, Na_2O 9.0, K_2O 1.2 wt.%	NiO	0	Sil. Liq.	10	SiO_2 67.3, TiO_2 0.79, Al_2O_3 12.2, Cr_2O_3 0.045, FeO 0.33, MgO 4.0, NiO 0.0, CaO 5.1, Na_2O 9.0, K_2O 1.2 wt.%
CaO	2.85				CaO	2.58			
Na_2O	1.48				Na_2O	1.34			
K_2O	0.15				K_2O	0.13			
Fe	1.88				Fe	10.5			
Ni	0.24				Ni	0.73			

Author's personal copy

Table 3
Relative atomic abundances in systems employed in this work, and their components.

Element	Solar	Type I* Dust	Enhancement due to 600xDust enrichment	Enhancement due to 550xWater enrichment	Bulk system composition	Gas composition
H	2.790E+10	–	–	6.406E+09	3.431E+10	3.431E+10
He	2.720E+09	–	–	–	2.720E+09	2.720E+09
C	6.849E+06	–	–	–	6.849E+06	6.849E+06
N	3.130E+06	–	–	–	3.130E+06	3.130E+06
O	1.367E+07	3.347E+06	2.005E+09	3.203E+09	5.222E+09	3.213E+09
Na	5.740E+04	5.740E+04	3.438E+07	–	3.444E+07	–
Mg	1.074E+06	1.074E+06	6.433E+08	–	6.444E+08	–
Al	8.490E+04	8.490E+04	5.086E+07	–	5.094E+07	–
Si	1.000E+06	1.000E+06	5.990E+08	–	6.000E+08	–
P	1.040E+04	–	–	–	1.040E+04	1.040E+04
S	4.458E+05	4.458E+04	2.670E+07	–	2.715E+07	–
K	3.770E+03	3.770E+03	2.258E+06	–	2.262E+06	–
Ca	6.110E+04	6.110E+04	3.660E+07	–	3.666E+07	–
Ti	2.400E+03	2.400E+03	1.438E+06	–	1.440E+06	–
Cr	1.350E+04	1.350E+04	8.087E+06	–	8.100E+06	–
Fe	9.000E+05	9.000E+04	5.391E+07	–	5.481E+07	–
Ni	4.930E+04	4.930E+03	2.953E+06	–	3.002E+06	–

* For Type II dust, the abundances of Fe, Ni and S are 2.970×10^5, 1.627×10^4 and 1.471×10^5, respectively.

4.8. Composition of the total system

As seen in Fig. 1a–d, isotopic mass-fractionations of relatively volatile elements in chondrules are very small to nonexistent. Enriching the bulk composition of the system in dust relative to gas is a way of suppressing isotopic fractionation that might otherwise occur during heating and evaporation of chondrule precursors. This is because the fraction of a volatile element that need be evaporated in order to reach the equilibrium vapor pressure in the ambient gas becomes smaller with increasing dust enrichment. In the present work, the system was assumed to be enriched in dust by a factor of 600 relative to the gas compared to solar composition. The dust is assumed to be a low-temperature condensate that was processed into the chondrule precursors shown in Table 2. Thus, the dust compositions are those in Table 2, augmented by the chondritic proportion of S assumed to have been degassed when the precursors formed by heating the dust to 1400 K, the starting point of the present calculations. Atomic abundances adopted by Fedkin and Grossman (2006) and used herein are shown in Table 3, along with the composition of Type I dust derived from them and the amounts of each element added to solar abundance due to enrichment in Type I dust by a factor of 600.

Olivine in both Type I and Type II chondrules contains significant FeO. At liquidus temperatures, the gas with which such chondrule compositions are in equilibrium has log f_{O_2} ~IW-1.3, ~5 log units more oxidizing than a system of solar composition. Grossman et al. (2008) reviewed two ways of creating cosmic gases more oxidizing than solar composition: by dust enrichment; and by water enrichment. When gas otherwise solar in composition is enriched in dust by a factor of 600, log f_{O_2} of the ambient gas reaches only ~IW-2.6 at chondrule liquidus temperatures. Therefore, in addition to this dust enrichment, the system was assumed to be enriched in water by a factor of 550. The amount added to the system was calculated by multiplying by 549 the fractional abundances of hydrogen and oxygen that are present as water in solar gas at 10^{-3} bar and a temperature of 1800 K, where there are no stable condensates. The amounts of H and O so added to solar composition are shown in Table 3, as well as the bulk composition of the system, determined by adding to solar composition the augmentations due to dust and water enrichment. For 600× dust and 550× water enrichment relative to solar composition, 38% of the added oxygen is from the added dust. The initial gas composition shown in Table 3 is obtained by subtracting the total amount of each element in the dust from the bulk composition of the system.

4.9. Computational strategy

Because the equilibrium mineralogical composition of the chondrule precursor is calculated from MELTS at a specific temperature and f_{O_2}, the activities of all components and the volumes of all condensed phases are known. The equilibrium vapor pressure of each species is calculated from the activities of the components and from the composition and assumed P^{tot} of the surrounding gas in the manner described above. The actual molecular speciation of the ambient gas is also calculated as above from its elemental composition, temperature and P^{tot}. At the initial temperature and P^{tot}, the flux of each molecular species out of or into the droplet is calculated from Eq. (16), and the total flux of each element from Eqs. (17) and (19). To calculate the rate of evaporation or condensation of each species or element, its flux must be multiplied by an appropriate surface area. The radius of the droplet and its total surface area are calculated from the sum of the volumes of all constituent phases. Table 2 shows that the starting Type II assemblage contains 11 wt.% Fe,Ni alloy, which translates to 4.8 vol.%. An initial radius of 3 μm is assumed for each

Author's personal copy

grain of metallic Fe,Ni, and the number of such grains is calculated from the initial total volume of metal and held constant. It is assumed that five per cent of the metal grains reside on the surface of the droplet at all times, and that each consumes πr^2 of surface area. Metal thus occupies ~10.4% of the total surface area initially and is over-represented compared to its volume percent. Because of very low metal contents, the proportion of the metal residing on the surface was gradually increased during cooling in most of the Type I model runs to ensure full recondensation of iron. The relative surface areas of non-metallic phases are assumed equal to their relative volumes. Silicate liquid is the only non-metallic phase assumed to evaporate. The fluxes of Fe and Ni associated with metallic Fe,Ni are then multiplied by the surface area of metal, and the fluxes of all elements associated with silicate liquid by the surface area of that phase. In all cases in this study, the equilibrium f_{O_2} of the droplet is initially less than the ambient f_{O_2}, so the oxygen redox flux is multiplied by the surface area of metal in order to oxidize metallic Ni and Fe into $NiSi_{0.5}O_{2(l)}$ and $Fe_2SiO_{4(l)}$, respectively.

The chemical evolution of the droplet is calculated while the temperature and P_H^{tot} of the system change according to the input thermal history. Although the full thermal history calculation begins at a much lower temperature and P_H^{tot}, the chemical evolution calculation begins only when the temperature and P_H^{tot} reach 1400 K and the corresponding P_H^{tot}, respectively. A time step size corresponding to a temperature change of 0.3–3 K is selected. Its size may vary from a fraction of a second to several minutes within a given model run, depending on the instantaneous rate of change of temperature. A typical model run requires 1000 to 1500 time steps to complete a heating and cooling cycle. The initial rates of evaporation and condensation calculated above for silicate liquid and metallic phases are multiplied by the initial time step size in order to calculate the absolute amount of each element crossing the droplet-vapor interface. The amount of each element evaporated from the droplet is subtracted from the initial amount present and added to the ambient gas, and the amount condensed, including oxygen, is subtracted from the ambient gas and added to the droplet. The fractions of each element's total system abundance in the vapor and in the droplet are known prior to the evaporation step, and the known fraction by which these amounts change during the evaporation step is used to adjust P_i^{tot} in the ambient gas using Eq. (7). At the next time step, where temperature and P_H^{tot} are different from those in the previous step, the compositions of both the droplet and the ambient gas are also incrementally different due to evaporation and condensation during that step. The equilibrium f_{O_2} of the droplet is found by iteration until an assemblage is produced whose oxygen content matches the known oxygen content of the droplet to within 10^{-12}. This usually requires about 50 iterations. The f_{O_2} so determined, together with the activities of this equilibrium assemblage and the new ambient gas composition, are used to compute a new set of vapor pressures for this time step. The speciation of the ambient gas is also calculated from its new elemental composition, and new fluxes are obtained. The sizes of the metal grains are allowed to change, and the relative surface areas of the phases are calculated for the new time step. In a typical model run, the MELTS equations are solved between $5x10^4$ and 9×10^4 times, requiring about 6 h of computation time on a 2 GHz G5 processor.

Because the goal of this work is to model olivine chondrules, formation of all non-metallic phases other than olivine and spinel was suppressed during cooling, allowing a metastable liquid to persist to 900 K.

Relict olivine grains survive in porphyritic chondrules, and in experiments in which olivine spends more time at near-liquidus temperatures than in many shock wave thermal histories. Similarly, olivine zoning is ubiquitous in chondrules, and is produced in experiments whose cooling rates, similar to those in the shock wave thermal histories investigated herein, yield chondrule textures. Evaporation rates depend on the instantaneous liquid composition, but this differs from that of the equilibrium liquid at the same temperature when relict grains survive or fractional crystallization occurs. Thus, in order to model evaporation from a chondrule liquid properly, its composition variation should reflect sequestration of (1) relict grains; and (2) appropriate relative amounts of fractionally crystallized olivine of each fayalite content. Therefore, a theory of non-equilibrium melting and an empirical model of fractional crystallization of the silicate fraction of the droplet were incorporated into the present model, and are discussed in the Appendix. For descriptions of the equilibrated and sequestered fractions and the relationship between them, as well as of PO and BO models, the reader is referred to Appendix E.

5. RESULTS AND INTERPRETATION

5.1. Shock wave thermal histories

Three of the shock wave thermal histories shown in Fig. 2 were selected for investigation. All resulted from using a chondrule radius of 0.5 mm, and water and dust enrichments of 550x and 600x, respectively, but have distinctly different temperature profiles. The one for a shock velocity of 7 km/s and initial $P^{tot} = 1.5 \times 10^{-6}$ bar (Fig. 2b) reaches the highest peak temperature, 2170 K, has the highest heating and cooling rates, 97 and 154 K/hr, respectively, of all three, and is referred to hereafter as the "high temperature" profile. The one for 6 km/s and initial $P^{tot} = 1.5 \times 10^{-6}$ bar (Fig. 2a), the "fast heating" profile, has a near-liquidus peak temperature and intermediate heating and cooling rates, 78 and 114 K/hr. The one for 9 km/s and initial $P^{tot} = 3\times10^{-7}$ bar (Fig. 2d), the "slow heating" profile, also has a near-liquidus peak temperature, and has the lowest heating and cooling rates, 19 and 27 K/hr. Mineralogical, chemical and isotopic properties calculated for model chondrules are shown in Table 4 for the PO and BO case of each precursor composition (Types I and II) subjected to each of these thermal histories.

5.2. Evolution of a Type II precursor

5.2.1. Standard case: fast heating, all solid nuclei destroyed; a Type II BO simulation

As seen in Fig. 2a, the pre-shock, peak and inflection temperatures for this profile are 1750, 1916 and 1777 K,

Author's personal copy

Table 4
Distribution of isotopes of Mg, Si and Fe within model chondrules at 900 K.

Composition	Type I						Type II					
Texture type	BO (supercooled)			PO (relics)			BO (supercooled)			PO (relics)		
Thermal history	High-T	Fast heating	Slow heating	High-T	Fast heating	Slow heating	High-T	Fast heating	Slow heating	High-T	Fast heating	Slow heating
Glass												
Wt% Na_2O	4.41	4.67	4.83	5.25	4.11	4.11	4.79	5.15	5.80	4.09	3.56	3.61
Wt% FeO	4.53	2.89	1.95	0.09	7.07	7.13	5.95	4.99	2.12	8.95	18.01	17.03
Wt% MgO	3.49	1.20	1.02	0.68	4.18	4.17	5.99	3.02	1.25	8.88	5.04	5.03
Wt% in chondrule	33.88	31.82	30.57	28.16	35.33	35.75	27.67	25.37	22.47	32.46	37.20	36.55
δ^{25}Mg	20.85	6.91	2.49	24.73	−0.96	−0.27	20.57	4.05	1.53	15.43	−0.47	−0.10
δ^{29}Si	1.58	0.28	0.37	0.41	−2.06	−0.95	2.77	0.62	0.60	1.26	−1.51	−0.69
δ^{56}Fe	6.19	8.29	15.40	8.21	1.77	1.61	5.86	7.17	6.73	2.50	0.74	0.89
Olivine												
δ^{25}Mg min	−3.50	−0.32	−0.22	−7.38	−2.80	−1.78	−4.25	−0.37	−0.27	−7.64	−2.30	−1.17
δ^{25}Mg mean	−1.58	−0.18	−0.04	−0.92	0.00	0.01	−1.89	−0.16	−0.02	−2.12	0.01	0.01
δ^{25}Mg max	13.88	3.13	1.25	25.81	0.51	0.32	11.86	1.01	0.72	7.08	0.53	0.33
δ^{29}Si min	−3.38	−0.69	−0.55	−5.71	−2.86	−2.25	−3.74	−0.72	−0.60	−5.78	−2.72	−1.94
δ^{29}Si mean	−2.92	−0.65	−0.35	−2.19	1.17	0.76	−3.39	−0.68	−0.36	−2.37	1.09	0.61
δ^{29}Si max	−0.69	−0.21	0.20	1.16	2.69	2.39	−1.27	−0.34	0.28	4.91	2.74	2.41
δ^{56}Fe min	−18.00	−18.00	−18.00	−18.00	−18.00	−18.00	−18.00	−7.70	−6.80	−18.00	−18.00	−18.00
δ^{56}Fe mean	−5.72	−7.97	−4.86	−0.20	−5.92	−5.46	−5.27	−3.75	−1.18	−5.08	−6.46	−5.14
δ^{56}Fe max	3.09	3.71	11.34	8.77	−0.49	0.46	1.68	1.83	4.47	−0.94	−3.49	−1.57
Bulk												
δ^{25}Mg	−0.84	−0.11	−0.02	−0.87	−0.04	−0.01	−0.75	−0.06	−0.01	−0.56	−0.02	0.00
δ^{29}Si	−0.86	−0.24	−0.04	−1.11	−0.34	−0.06	−0.92	−0.21	−0.04	−0.70	−0.14	−0.01
δ^{56}Fe	−0.56	−2.79	−1.76	−0.12	0.00	0.00	−1.20	−1.32	−0.30	−0.35	−0.24	−0.01
% of total Mg condensed	96.54	99.50	99.95	96.25	99.79	99.99	97.44	99.84	99.99	98.02	99.94	100.00
% of total Si condensed	96.98	99.13	99.92	95.45	98.41	99.86	96.78	99.31	99.94	97.66	99.59	99.99
% of total Fe condensed	93.49	78.16	91.21	99.02	100.00	100.00	92.12	93.76	99.00	97.62	98.85	99.97

Author's personal copy

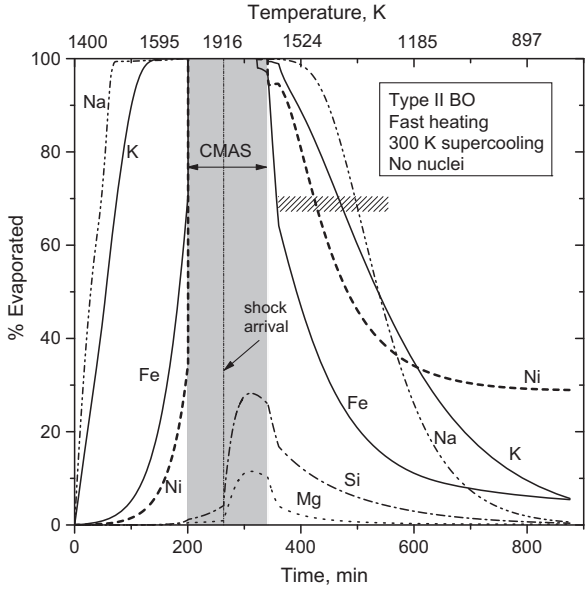

Fig. 4. Percent of each of Na, K, Fe, Ni, Si and Mg calculated to evaporate when a Type II precursor is subjected to the fast heating thermal history. Droplet temperatures corresponding to various times are indicated at the top of the graph. Total loss of Fe occurs even before the pre-shock temperature is reached. The shaded region indicates the time interval over which the droplet composition was modeled as a CMAS system. Cross-hatched bar represents the interval over which olivine solidifies.

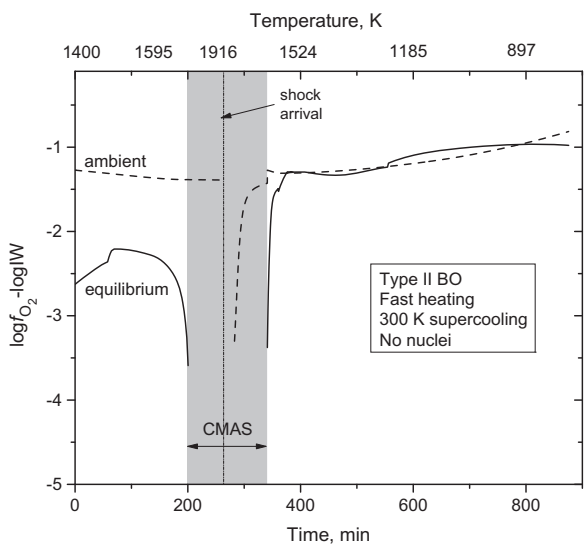

Fig. 5. Redox equilibration of the droplet and gas when a Type II precursor is subjected to the fast heating thermal history. The log of the equilibrium f_{O_2} of the droplet (solid curve) and of the ambient gas (dashed curve) are each plotted as a function of time relative to the logarithm of the f_{O_2} of the iron-wüstite (IW) buffer. The ambient f_{O_2} is only shown below 2000 K, the limit to which IW was extrapolated.

respectively, and the cooling rate is 114 K/hr. The corresponding pre-shock and final values of P^{tot} in Fig. 3a are 8.6×10^{-6} and 3.9×10^{-4} bar, respectively. The time of shock arrival is 263 min after the droplet reaches 1400 K. As the bulk composition of the droplet changes due to evaporation along this profile, its liquidus temperature also changes, and the last solids would melt at 1896 K at equilibrium, 20 K below the peak temperature reached within the spike. Although the droplet contains 23 wt.% olivine and 25 wt.% orthopyroxene at the pre-shock temperature, it was assumed in this run that all solid nuclei would be destroyed.

In Fig. 4, the fraction of each element evaporated is plotted as a function of time. Significant fractions of Na and K begin to evaporate before any other element, and both are completely lost from the droplet prior to shock arrival. Although they evaporate more gradually than the alkalis, both Fe and Ni also are lost totally at 1658 K, ~100 K below the pre-shock temperature. Subsequent modeling of the liquid requires use of the CMAS activity-composition model (Berman, 1983). Significant fractions of Si and Mg evaporate only after total Fe loss, increase sharply after the temperature peaks and reach maxima of 28 and 11%, respectively, before recondensation begins. These results are relatively insensitive to conditions within the temperature spike, as its duration is so short that only ~10% and ~7% of the total volatilized Si and Mg, respectively, evaporate within it. Si and Mg recondense relatively quickly, but the alkalis do so very gradually over the next 10 h, reaching total condensation after the droplet cools below 800 K. Fe

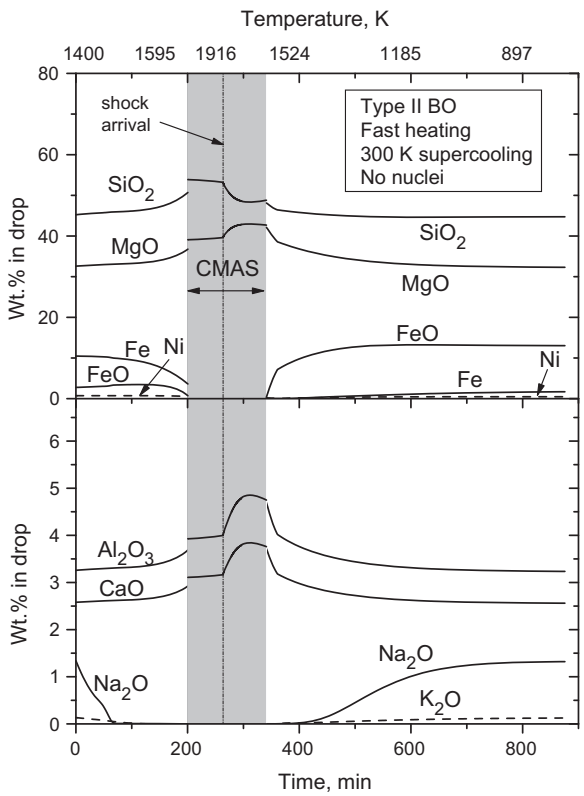

Fig. 6. Bulk chemical composition of the droplet when a Type II precursor is subjected to the fast heating thermal history, plotted as a function of time. The major effects seen are due to oxidation and evaporation of metallic Fe, and evaporation and recondensation of alkalis.

Author's personal copy

and Ni begin to recondense relatively quickly but their recondensation rates slow markedly below 1200 K. For Fe, this is because the condensation coefficient of FeO becomes very small at this temperature; for Ni, because the surface area of metal is very small. The high dust enrichment fails to prevent evaporation but it does promote recondensation.

Alexander (2001) drew attention to the possible role of diffusion in limiting evaporation rates. For each element, both the diffusion rate through the liquid and the evaporation and recondensation rates vary continuously as the temperature and composition of the liquid change. To the extent that published diffusion coefficients apply to the range of liquid compositions generated within the droplet at their predicted temperatures, diffusion appears to be able to keep pace with the evaporation rates of all elements considered here, but may be unable to homogenize the silicate liquid continuously as fast as recondensation of K, Fe and Si occurs. Diffusion, however, is not the only means by which the liquid can be homogenized. While the droplets are molten, their shapes change due to rotation and the ram pressure they experience as they move through the gas (Miura et al., 2008), and this causes their internal flow fields to evolve. The internal dynamics depend sensitively on such parameters as the gas density, the relative velocity of the droplet with respect to the gas, the rotation rate, the viscosity of the melt, and the proportion and sizes of crystals, each of which varies with time as the droplet cools and interacts with the gas. Thus, the melt and crystals inside will be stirred continuously as they attempt to reach the equilibrium shape and flow structures governed by the instantaneous physical conditions experienced by the droplet. Because of the combined effects of stirring and diffusion, it is assumed that liquid heterogeneity is minimal.

The variation of the equilibrium f_{O_2} of the droplet and the f_{O_2} of the ambient gas are plotted in Fig. 5 as a function of time. Given the elemental composition of the ambient gas, its log f_{O_2} at 1400 K is IW-1.3. As temperature rises, both the surface area of silicate liquid and the evaporation coefficient of FeO from it increase, but so do the oxidation coefficient of metallic iron and the evaporation coefficient of Fe from it. As a result, the FeO concentration and, consequently, the equilibrium f_{O_2} of the droplet first rise and then fall before total Fe loss. The uptake of oxygen by the droplet causes the f_{O_2} of the ambient gas to decrease slightly in this temperature interval. Because of the absence of Fe during the interval where the CMAS model is used, the equilibrium f_{O_2} of the droplet is undefined. After shock passage, incipient recondensation of Fe results in a low FeO content of the liquid and, consequently, a low equilibrium f_{O_2}. As the temperature falls further, the FeO content of the liquid and the equilibrium f_{O_2} both increase rapidly. The rate of metallic Fe recondensation is limited by the small surface area of metal, and the large difference between the ambient and equilibrium f_{O_2} causes rapid oxidation of a large fraction of the metal that does manage to recondense. At ~400 min, the droplet and ambient gas become very similar in log f_{O_2} at ~IW-1.3, after which time oxidation or reduction of the droplet may occur depending on relative rates of condensation of metallic Fe and FeO.

The resulting changes in the bulk chemical composition of the droplet are plotted as a function of time in Fig. 6. Prior to shock passage, the relatively rapid decline in Na_2O and K_2O contents is caused by their evaporation, and the more gradual decrease in the content of metallic Fe is caused by a combination of evaporation and oxidation. The FeO content first increases slightly and then decreases. This is due to the fact that the oxidation rate of metallic Fe is at first greater than the evaporation rate of FeO but becomes smaller than the latter as the amount of metallic Fe drops sharply. Total Fe loss prior to shock passage is responsible for the discontinuous jumps in the concentrations of other elements. Within the CMAS interval, Si evaporation is more extensive than that of Mg, causing the Mg concentration to increase along with those of Ca and Al. During recondensation, the FeO concentration rises more steeply than that of Fe due to the relatively high f_{O_2}. After 400 min, the metallic Fe concentration gradually increases because its recondensation rate is greater than its oxidation rate.

The changing mineral proportions in the model droplet are illustrated in Fig. 7. As the temperature rises and alkalis are volatilized, feldspar and clinopyroxene are the first phases to dissolve in the melt, making excess SiO_2 available for reaction of olivine with liquid to form orthopyroxene. The proportion of Fe,Ni alloy gradually falls due to evaporation and oxidation of Fe, and orthopyroxene begins dissolving into the melt after 62 min. Total Fe loss occurs at 200 min, causing destabilization of FeO-bearing spinel. The discontinuities seen at this point in the amounts of olivine, orthopyroxene and silicate liquid are due to small inconsistencies in the activity-composition relations between the MELTS model (Ghiorso and Sack, 1995) and

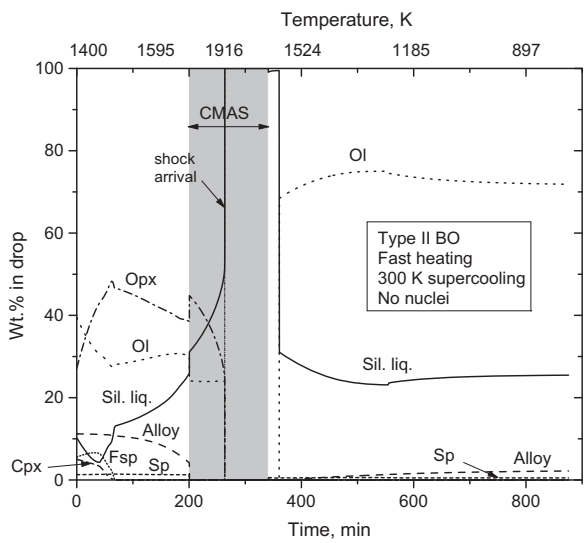

Fig. 7. Mineralogical composition of the droplet when a Type II precursor is subjected to the fast heating thermal history, plotted as a function of time. All nuclei of olivine and orthopyroxene are assumed to be destroyed at superliquidus temperatures within the spike, olivine is assumed to crystallize after 300 K of supercooling, and olivine and spinel are the only non-metallic phases assumed to nucleate.

Author's personal copy

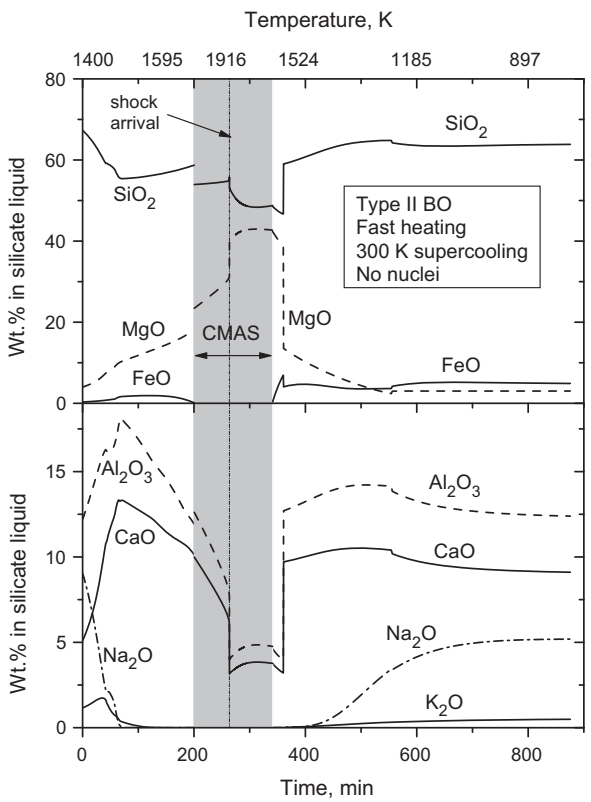

Fig. 8. Bulk chemical composition of silicate liquid in the droplet when a Type II precursor is subjected to the fast heating thermal history, plotted as a function of time. During the first 200 min, the liquid evolution is dominated by melting of feldspar and clinopyroxene, a faster rate of evaporation of the alkalis than the rate at which they are added by melting, and formation of orthopyroxene by reaction of olivine with the liquid. At the time of shock arrival, orthopyroxene and olivine dissolve and, at later times, olivine subtraction and recondensation of FeO and alkalis control the liquid composition.

the CMAS model (Berman, 1983). Assumptions made in this run are that all orthopyroxene and olivine remaining at the pre-shock temperature dissolve at the superliquidus temperature within the spike, olivine does not nucleate until the liquid subcools by 300 K, to 1595 K at 361 min, and that olivine and spinel are the only non-metallic phases that nucleate during cooling, thus simulating a barred olivine (BO) chondrule. About 68% of the droplet crystallizes as olivine at this point, followed by another few% over the next ~100 K. As the temperature falls, more metallic Fe,Ni condenses and, when the temperature falls to 900 K, the object contains 72 wt.% olivine, 25% glass (Table 4), 2% metal and 1% spinel.

The change in silicate liquid composition accompanying the above mineralogical changes is shown as a function of time in Fig. 8. At 1400 K, the initial liquid composition is that listed for the Type II precursor assemblage in Table 2. As clinopyroxene and feldspar dissolve into the liquid with increasing temperature, the CaO and Al_2O_3 contents of the liquid increase but the evaporation rates of the alkalis exceed the rates at which they are added to the liquid, and their concentrations fall. The SiO_2 content falls and the MgO content increases as the liquid gradually reacts with olivine to form orthopyroxene. The FeO content gradually increases and then falls as metallic Fe,Ni is first oxidized and then volatilized. When large amounts of orthopyroxene melt prior to total Fe loss, the MgO and SiO_2 contents rise and those of CaO and Al_2O_3 fall. Discontinuities seen in the concentrations of these four oxides at 200 min are due again to small inconsistencies between the MELTS and CMAS models. When residual olivine and orthopyroxene melt at the time of shock passage, the MgO concentration rises and those of CaO and Al_2O_3 fall. After shock passage, rapid evaporation depletes the melt in SiO_2, causing the concentrations of MgO, CaO and Al_2O_3 to rise. When olivine nucleates, the MgO content drops sharply, causing sudden increases in the concentrations of SiO_2, CaO and Al_2O_3. Evolution of the silicate liquid composition beyond this point is controlled by further olivine subtraction and recondensation of FeO and alkalis. If quenching occurred at 900 K, the glass would contain 3.0% MgO, 5.0% FeO and 5.2% Na_2O, as seen in Table 4, and 63.7% SiO_2 and 0.47% K_2O.

The histogram of olivine compositions that precipitate from the liquid is shown in Fig. 9a. In this run, all crystals remaining at the pre-shock temperature are assumed to have melted during the temperature spike to superliquidus temperatures. The histogram is thus composed only of olivine that formed by fractional crystallization after the liquid subcooled 300 K to 1595 K, where the cooling rate is 114 K/hr. Crystallization begins at 361 min, and the degree of sequestration reaches 100% when the droplet reaches 1270 K at 547 min. The olivine is FeO-bearing because these temperatures are below that where FeO recondensation begins. The mean X_{Fa} is 0.171, well within the range of the BO chondrules in Fig. A-1b. The shape of the calculated histogram is very similar to that of Chondrule 696 in having a short, low-Fa limb and a long, high-Fa tail.

The variation of δ^{25}Mg and δ^{29}Si with time is shown in Fig. 10a and b, respectively. Preferential evaporation of light isotopes causes δ^{25}Mg and δ^{29}Si of the gas (insets) to begin at −10.0‰ and −8.6‰, respectively, and δ^{25}Mg and δ^{29}Si of the equilibrating fraction of the droplet to become only slightly more positive than the sequestered solids that remain isotopically normal. Due to the temperature dependence of the Mg isotope fractionation factor, δ^{25}Mg of the gas becomes more negative while δ^{29}Si becomes slightly less negative. The sequestered fraction disappears during shock passage, where the isotopic composition of the droplet becomes that of the equilibrating fraction. Evaporation of Mg and Si becomes more significant after the temperature peaks, where δ^{25}Mg and δ^{29}Si of the droplet reach maxima of 0.85 and 1.9‰, respectively, before falling due to isotopic exchange and recondensation. Post-shock, δ^{25}Mg and δ^{29}Si of the ambient gas increase, first because the evaporating droplet has higher δ^{25}Mg and δ^{29}Si and later because of preferential recondensation of light isotopes. A sequestered fraction reappears with the start of olivine crystallization, when δ^{25}Mg and δ^{29}Si of the equilibrating fraction are −0.36 and −0.34‰, respectively. Continued recondensation causes δ^{25}Mg and δ^{29}Si of the

Author's personal copy

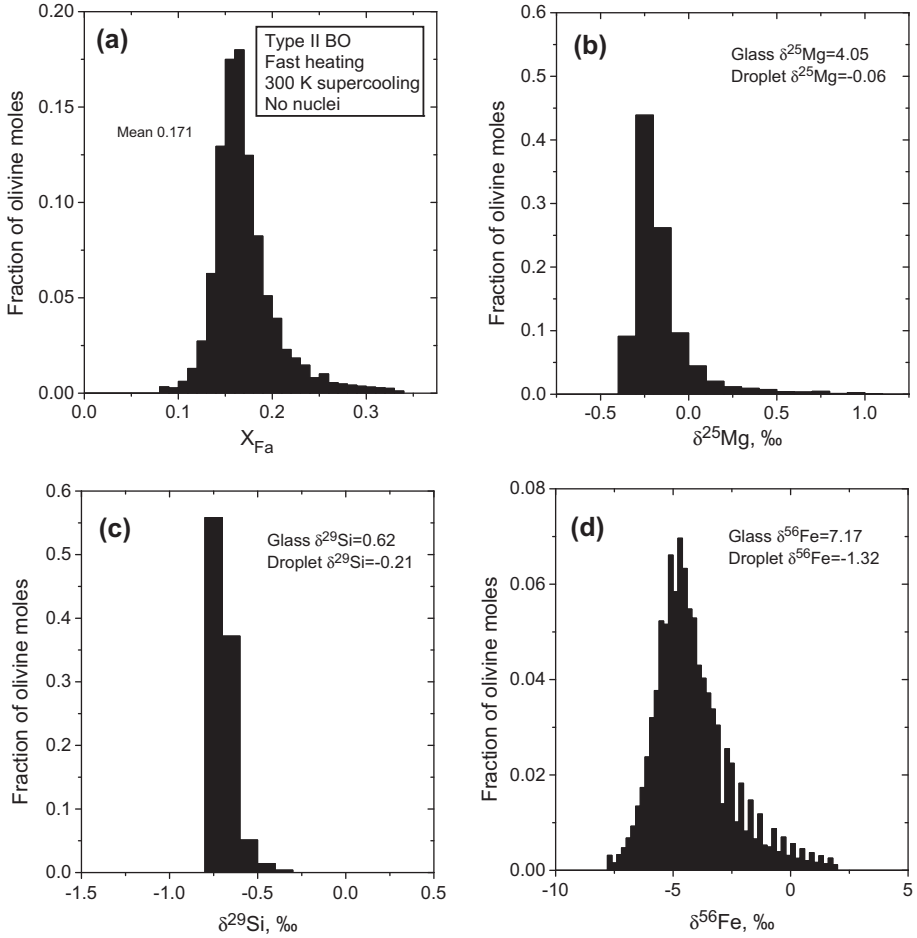

Fig. 9. Histograms of (a) fayalite content; (b) δ^{25}Mg; (c) δ^{29}Si; and (d) δ^{56}Fe recorded by fractionally crystallized olivine in the model droplet when a Type II precursor is subjected to the fast heating thermal history. The histogram in (a) is similar to several of those of Fig. A-1b, particularly chondrule 696.

equilibrating fraction to fall slightly, and the cumulative δ^{25}Mg and δ^{29}Si of the sequestered crystals even more slowly. The isotopic composition of the equilibrating fraction becomes distinguishable from that of the bulk droplet when the sequestered fraction becomes significant. Shortly thereafter, δ^{25}Mg and δ^{29}Si of the equilibrating fraction begin to rise because of the rising δ^{25}Mg and δ^{29}Si of the gaseous Mg and Si condensing into it. At 900 K, δ^{25}Mg of the glass, the bulk olivine fraction and the bulk droplet are +4.1, −0.16 and −0.06‰ (Table 4), respectively. δ^{29}Si of these fractions are +0.62, −0.68 and −0.21‰, respectively. Remaining in the gas are 0.16% of the total Mg and 0.69% of the total Si (Table 4). If such a droplet quenched and stopped equilibrating with the gas at this temperature, its bulk δ^{25}Mg and δ^{29}Si would be well within the ranges observed in chondrules in Fig. 1a and b, respectively.

The variation of δ^{41}K with time is shown in Fig. 11a. Feldspar, the low-melting component, is the only K-bearing crystalline phase in the starting assemblage. Initially, K evaporates quickly from the liquid, producing a vapor with δ^{41}K of −19.3‰ and causing δ^{41}K to increase rapidly in the equilibrating fraction while sequestered feldspar retains normal K isotopic composition. At 60 min, all remaining feldspar is in equilibrium with the liquid, and dissolves completely at 69 min. δ^{41}K of the gas becomes less negative as δ^{41}K of the equilibrating fraction rises. The latter reaches a maximum of 107‰ when 99.6% of the K is evaporated, and then declines sharply due to isotopic exchange with near-normal, gaseous K. There is no K in the droplet during the CMAS interval. K begins to recondense into the droplet very slowly at first and then more quickly (Fig. 4), upon massive olivine precipitation at 361 min (Fig. 7). As a result, δ^{41}K of the droplet is initially negative, becomes less so as it exchanges with the gas, and then more negative when recondensation accelerates. As K recondensation nears completion, δ^{41}K of both gas and droplet gradually become more positive as δ^{41}K of the recondensing K is more negative than that of the gas but more positive than that of the droplet. At 900 K, 9.7% of the K remains in the gas, whose δ^{41}K is 40.8‰, and δ^{41}K of the droplet is −4.4‰.

The variation of δ^{56}Fe with time is shown in Fig. 13b. Initially, iron evaporates rapidly from solid Fe,Ni without isotopic fractionation and relatively slowly from silicate li-

Author's personal copy

quid, producing a very small positive δ^{56}Fe in the equilibrating system and the bulk droplet and a small negative δ^{56}Fe in the ambient gas. The rate of Fe evaporation from metal increases relative to that from silicate with increasing temperature, causing δ^{56}Fe of the ambient gas to increase but, after ~51 min, the relative evaporation rate falls due to the increased surface area of silicate liquid, causing a greater rate of increase of δ^{56}Fe in the equilibrating system and the bulk droplet and a decrease of δ^{56}Fe in the ambient gas. During the CMAS interval, all Fe is in the gas. When recondensation of FeO into the silicate liquid and of metallic Fe onto metal nuclei begin, the droplet is isotopically light initially, causing δ^{56}Fe of the gas to become positive. Continued recondensation of Fe that is isotopically lighter than that in the gas but heavier than that in the equilibrating fraction causes δ^{56}Fe of both to increase gradually. Olivine that forms by fractional crystallization instantaneously incorporates δ^{56}Fe of the equilibrating system. δ^{56}Fe of the sequestered fraction is the cumulative δ^{56}Fe of the fractionally crystallized olivine, and necessarily lags that of the equilibrating fraction. δ^{56}Fe of the sequestered fraction thus rises and then levels off while that of the equilibrating fraction continues to increase, as recondensation continues even though olivine crystallization has ceased. At 900 K, 6.2% of the total Fe is in the gas (Table 4), whose δ^{56}Fe is 20.2‰. δ^{56}Fe of the glass, the total sequestered olivine and the total droplet are +7.2, −3.8, and −1.3‰ (Table 4), respectively. The latter value is just beyond the range of values observed for the chondrules in Fig. 1d.

Because fractional crystallization of olivine occurs while the isotopic composition of the liquid is changing during recondensation, a range of isotopic compositions is recorded by olivine. The cores of the first grains to crystallize inherited the isotopic composition the liquid possessed when solidification began, while the last grains to nucleate and the rims on earlier grains crystallized with the isotopic composition the liquid had at the end of solidification. Histograms showing the distribution of each of δ^{25}Mg, δ^{29}Si and δ^{56}Fe (Fig. 9b, c and d) reveal variations of ~1.4, 0.4 and 9.5‰, respectively, within the total olivine in the model droplet. Sequestration of olivine occurs from 1595 K at 361 min to 1270 K at 547 min, during which time both δ^{25}Mg and δ^{29}Si (Fig. 10a, b) of the equilibrating fraction pass through minima, while δ^{56}Fe increases monotonically. Thus, for any olivine grain that nucleated at the beginning and continued to grow until the end of this interval, the variation of δ^{56}Fe from core to rim would be from the lowest value on the histogram to the highest, while both δ^{25}Mg and δ^{29}Si would first decrease and then increase. Because recondensation of heavy isotope-enriched Mg, Si and Fe into the liquid continues after olivine crystallization ceases, glass formed from the quenched liquid will also be enriched in the heavy isotopes compared to the sequestered olivine. If quenching of the liquid at 900 K ended gas-droplet isotopic communication, δ^{25}Mg and δ^{56}Fe of the glass would be 4.1‰ and 7.2‰, respectively, while δ^{29}Si would be only 0.6‰ (Table 4). These are all substantially more positive than their respective values in any olivine in the droplet. Note that, for each of these elements, the mean isotopic compositions of olivine, glass and the bulk droplet are independent of the time step size used in the calculation. When the step size is reduced by a factor of ten during olivine crystallization, the maximum deviation found in any of the δ-values is 0.05‰.

Table 4 also shows that δ^{25}Mg and δ^{56}Fe of the bulk droplet are −0.06‰ and −1.3‰, respectively, reflecting the fact that only 0.2% of the total Mg is still uncondensed, while 6.2% of the total Fe is still in the gas at 900 K (Fig. 4). A greater proportion of the K remains in the gas, 9.7%, resulting in a δ^{41}K for the droplet of −4.4‰. The δ-values of all four elements are negative in the bulk droplet because the δ-values in the residual gas are all positive at this temperature. Inspection of Figs. 10 and 11 shows that the δ-values in the residual gas are all more positive than their respective values in the liquid, part of the equilibrated fraction. If quenching of the liquid were delayed, and the liquid maintained chemical communication with the gas to temperatures below 900 K, each of these elements would become more completely condensed, their δ-values in the bulk droplet would become more normal and the δ-values of Mg, Si and Fe in the resulting glass would become more positive than those in Table 4 and, in particular, would become even more different from their δ-values in the olivine. In the model, liquid is the only host phase for recondensing K, so there is no opportunity to develop K isotopic differences between phases.

In conclusion, very large internal isotopic heterogeneities in Mg, Si and Fe would be recorded in solidified droplets that formed in this way, even if their bulk compositions show only small deviations from normal isotopic composition. In addition, because of near-total K loss and faster recondensation of the light isotopes in this and all cases considered in this work, partial K recondensation always results in negative δ^{41}K in the glass and bulk droplet, the magnitude decreasing as the degree of K recondensation increases (*e.g.*, Fig. 11a).

5.2.2. High-temperature and slow heating profiles, with all solid nuclei destroyed; Type II BO simulations

Model runs were carried out with the same precursor along the high-temperature and slow heating profiles with all other parameters, including the 300 K of supercooling, kept the same as in the previous example. Evolution of the Type II precursor along these profiles is qualitatively similar to that seen along the fast heating profile, but much greater evaporative losses, 84% of the Si and 82% of the Mg, result from the longer time, 246 *vs* 70 min, spent above 1700 K along the high-temperature profile, and slightly smaller losses, 23% of the Si and 8% of the Mg, from the shorter time, 4 min, spent above 1700 K along the slow heating profile. The lowest X_{Fa} found in a given model run depends on the degree of condensation of Fe by the time olivine begins to crystallize. This is 36% and 33% in the fast and slow heating cases, respectively, where the lowest X_{Fa} is 0.09 and 0.08, but is only 4% in the high-temperature case, where the lowest X_{Fa} is 0.0. The mean X_{Fa} in a given model run is heavily influenced by the X_{Fa} at the temperature where the product of the total amount of equilibrium olivine and the fraction of it that is sequestered is a maximum. The first factor is a complex function of liquid

Author's personal copy

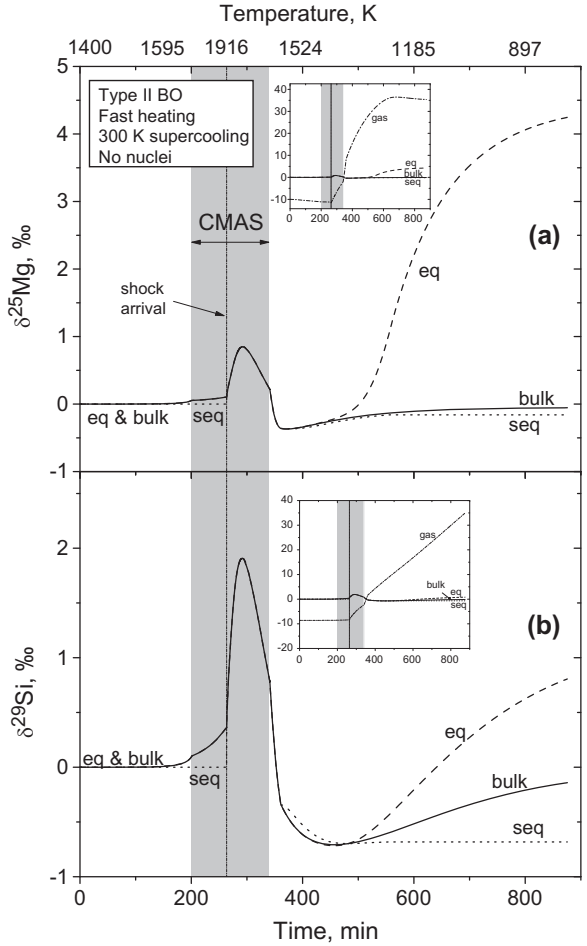

Fig. 10. The change in (a) δ^{25}Mg and (b) δ^{29}Si of the droplet when a Type II precursor is subjected to the fast heating thermal history, plotted as a function of time. The insets show the isotopic evolution of coexisting gas and droplet. Abbreviations: seq-sequestered fraction; eq – equilibrating fraction; bulk – bulk droplet.

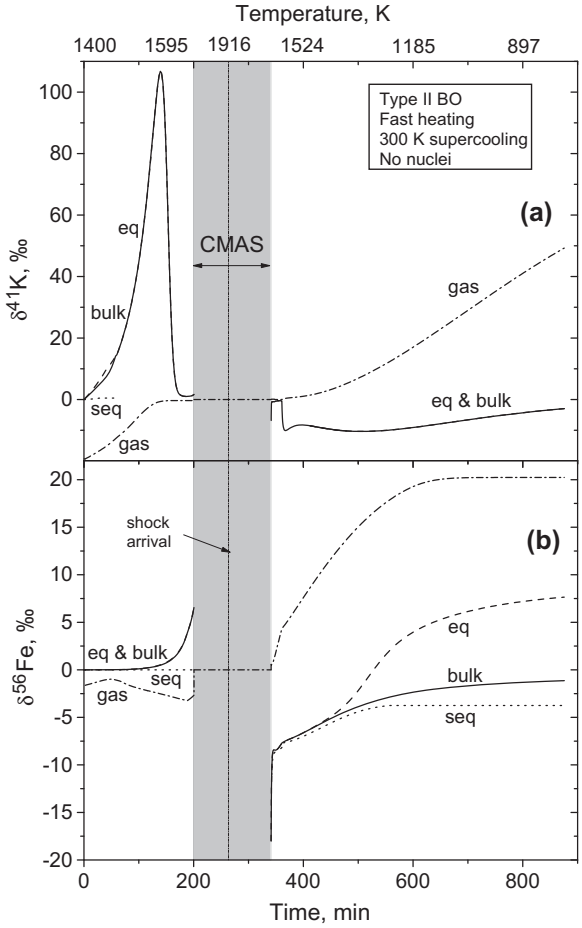

Fig. 11. The change in (a) δ^{41}K and (b) δ^{56}Fe for the droplet when a Type II precursor is subjected to the fast heating thermal history, plotted as a function of time. More than 99% of the K evaporates and the residual amount isotopically exchanges with the evaporated K before total Fe loss. Fractional crystallization of olivine begins at 1590 K (361 min), while δ^{56}Fe of the silicate liquid, part of the equilibrating fraction of the droplet, is strongly negative. At 900 K, 9.7% of the K is still uncondensed. The bulk droplet has δ^{41}K of −4.4‰ and δ^{56}Fe of −1.3‰. δ^{56}Fe of the bulk olivine and glass are −3.8‰ and +7.2‰, respectively. Abbreviations as in Fig. 10.

chemical composition and the second factor depends on cooling rate, as in Fig. E-2. Because the amount of sequestered olivine is a maximum at $X_{Fa} = 0.11$ in the high-temperature case, 0.165 in the fast heating case and 0.205 in the slow heating case, the mean X_{Fa} rises from 0.147 to 0.171 to 0.195 in the same sequence. The isotopic composition range sampled by olivine in a given model run is largely determined by the isotopic composition variation of the equilibrium assemblage (*e.g.*, Figs. 10 and 11) within the time interval when olivine is being sequestered, *e.g.*, between 360 and 547 min in the fast heating case in the cited Figures. As seen in Table 4, the ranges of δ^{25}Mg (~16‰) and δ^{56}Fe (~20‰) recorded by olivine are much greater, and those for δ^{29}Si (~2.5‰) slightly greater, in the high-temperature case than in the fast and slow heating cases. The 900 K liquid again has significantly more positive δ^{25}Mg, δ^{29}Si and δ^{56}Fe than all of the olivine in both the high-temperature and slow heating cases. In the bulk droplet, δ-values of these elements are again negative due to their incomplete recondensation; δ^{25}Mg and δ^{29}Si for the high-temperature case lie outside the ranges in chondrules (Fig. 1).

5.2.3. All thermal histories, with some nuclei remaining; Type II PO simulations

Model runs were performed with the same Type II precursor along the same three heating profiles as discussed in the previous two sections, but with some solid nuclei remaining, allowing fractional crystallization to occur with no supercooling. Results for the high-temperature profile are shown in Fig. 12. Because crystallization of large amounts of olivine at higher temperature modifies the liquid composition and reduces the surface area of liquid near the temperature of maximum evaporation in these cases, evaporative losses of Si and Mg are less than for the supercooling cases. For example, 75% of the Si and 65% of the Mg are evaporated in the high-temperature case (Fig. 12a), 29% and 4%, respectively, in the fast heating case and 25% and 3%, respectively, in the slow heating case. In

Author's personal copy

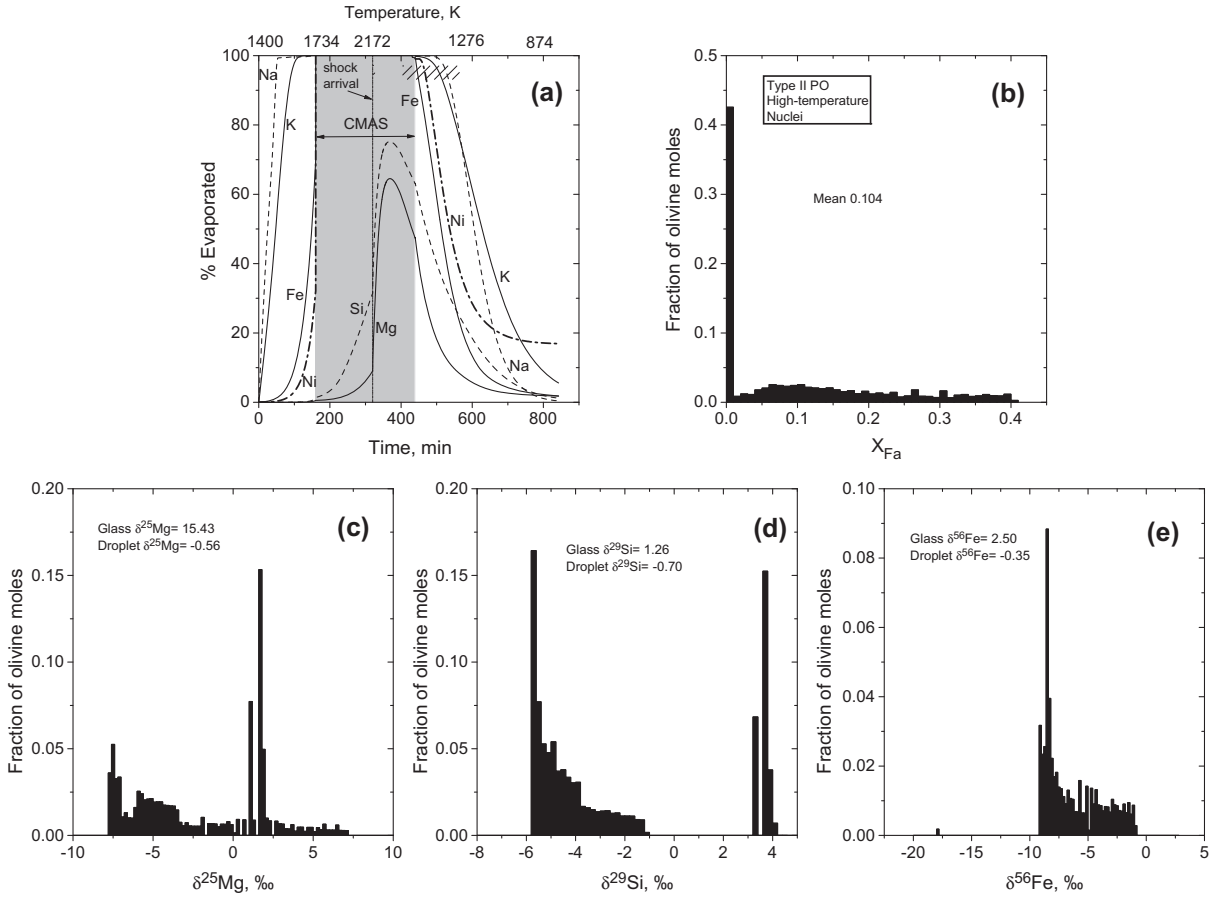

Fig. 12. Computed evaporation curves (a) and histograms of fayalite content (b), δ^{25}Mg (c), δ^{29}Si (d) and δ^{56}Fe (e) for a Type II precursor exposed to the high temperature thermal history, when solid nuclei are assumed to survive. Cross-hatching in (a) as in Fig. 4. In (e) and subsequent analogous figures, the sum of the olivine fractions in all bins may be <1 because much of the olivine is FeO-free.

all three cases, cooling and fractional crystallization of olivine start during the CMAS portion of the evolution, before the beginning of recondensation of iron, so the fayalite histograms are characterized by dominant peaks at $X_{Fa} \leqslant 0.01$ and long, very low tails out to $X_{Fa} = 0.40$. Despite the Type II bulk compositions of these systems, the mean X_{Fa}, 0.037 and 0.040, is within the Type I range in the fast heating and slow heating cases, respectively. The higher mean X_{Fa}, 0.104, in the high temperature case is due to a much smaller proportion of the total olivine, 43%, at $X_{Fa} \leqslant 0.01$ than in the other cases, ~78%. This, in turn, is due to the fact that, in the high-temperature case, no olivine crystallizes at temperatures above the inflection temperature, where the high cooling rate leads to a high degree of olivine sequestration. In the other cases, olivine crystallizes for ⩾80 K above the inflection temperature. Large variations of δ^{25}Mg (~1.5 to ~15‰), δ^{29}Si (~4 to ~11‰) and δ^{56}Fe (~14 to ~17‰) are recorded by olivine in all three thermal histories, while the 900 K liquid is enriched in ^{56}Fe compared to all of the olivine in all three cases and in ^{25}Mg and ^{29}Si in the high-temperature case (Table 4). Small negative δ-values in the bulk droplets are due to incomplete recondensation of Mg, Si and Fe, and all but δ^{29}Si in the high-temperature case lie within the chondrule ranges in Fig. 1.

5.3. Evolution of a Type I precursor

5.3.1. With all solid nuclei destroyed; Type I BO simulations

Model runs were conducted with the Type I precursor along the same three thermal history profiles discussed for the Type II precursor, assuming no solid nuclei survive and 400 K of supercooling. Results for the slow heating case are shown in Fig. 13. The degree of evaporation of all elements is almost the same as in the Type II cases with supercooling, and the same decline is seen in the maximum degree of evaporation of Si and Mg from the high-temperature to the fast heating to the slow heating cases (Fig. 13a). Model fayalite histograms peak between X_{Fa} of <0.01 (high-temperature) and 0.06 (slow heating), and have long, very low tails out to $X_{Fa} \geqslant 0.40$. In contrast to the Type II cases, the mean X_{Fa} are within the range of Type I chondrules, from 0.043 in the fast heating case to 0.061 in the slow heating case. But for the long, low tail, the histogram in Fig. 13b has similarities to those of the Type I chondrules CH18 and CH11 (Fig. A-1a). As seen in Table 4, the three thermal histories result in variations of ~1.5–17‰, 0.48–2.7‰ and 21–29‰ in δ^{25}Mg, δ^{29}Si and δ^{56}Fe, respectively, within the olivine in the model droplets. As in the Type II BO simulations, δ^{25}Mg, δ^{29}Si and δ^{56}Fe are each signifi-

Author's personal copy

Table 5
Sensitivity of model results to various input parameters for the Type II BO, fast heating simulation.

	Log fO_2 of starting material			% of metal on droplet surface		Oxidation rate, expressed as γ_O at 2000 K			Supercooling (K)		
	IW-2.1	IW-2.6*	IW-3.1	5*	15	$\gamma_O = 0.1$	$\gamma_O = 0.3$*	$\gamma_O = 0.6$	200	300*	400
Glass											
Wt% Na_2O	5.46	5.15	5.46	5.15	5.66	5.50	5.15	5.30	4.47	5.15	5.84
Wt% FeO	3.44	4.99	3.50	4.99	2.72	3.14	4.99	4.20	10.20	4.99	1.32
Wt% MgO	1.34	3.02	1.37	3.02	1.23	1.27	3.02	1.33	3.93	3.02	1.01
Wt% in chondrule	23.88	25.37	23.85	25.37	22.54	23.62	25.37	24.84	29.58	25.37	22.02
δ^{25} Mg	6.94	4.05	6.79	4.05	6.38	4.83	4.05	10.16	5.00	4.05	1.16
δ^{29}Si	0.62	0.62	0.62	0.62	0.56	0.63	0.62	0.38	−0.20	0.62	0.38
δ^{56}Fe	7.74	7.17	7.92	7.17	6.10	7.19	7.17	7.60	5.18	7.17	5.42
Olivine											
δ^{25}Mg min	−0.37	−0.37	−0.37	−0.37	−0.35	−0.33	−0.37	−0.36	−0.41	−0.37	−0.09
δ^{25}Mg mean	−0.13	−0.16	−0.13	−0.16	−0.12	−0.08	−0.16	−0.21	−0.27	−0.16	−0.02
δ^{25}Mg max	2.30	1.01	2.27	1.01	2.91	2.20	1.01	4.30	0.70	1.01	0.50
δ^{29}Si min	−0.72	−0.72	−0.71	−0.72	−0.69	−0.67	−0.72	−0.82	−1.40	−0.72	−0.58
δ^{29}Si mean	−0.67	−0.68	−0.67	−0.68	−0.65	−0.60	−0.68	−0.66	−0.30	−0.68	−0.35
δ^{29}Si max	−0.26	−0.34	−0.07	−0.34	−0.13	−0.03	−0.34	0.34	1.53	−0.34	0.09
δ^{56}Fe min	−7.67	−7.70	−7.69	−7.70	−7.33	−5.73	−7.70	−18.00	−18.00	−7.70	−3.45
δ^{56}Fe mean	−3.54	−3.75	−3.38	−3.75	−1.07	−2.88	−3.75	−5.02	−6.85	−3.75	−1.32
δ^{56}Fe max	3.50	1.83	4.39	1.83	4.88	4.12	1.83	3.85	−0.66	1.83	2.99
Bulk											
δ^{25} Mg	−0.06	−0.06	−0.06	−0.06	−0.06	−0.04	−0.06	−0.10	−0.08	−0.06	−0.02
δ^{29}Si	−0.23	−0.21	−0.22	−0.21	−0.25	−0.18	−0.21	−0.29	−0.26	−0.21	−0.11
δ^{56}Fe	−1.49	−1.32	−1.29	−1.32	−0.09	−1.12	−1.32	−1.82	−1.16	−1.32	−0.82
% of total Mg condensed	99.83	99.84	99.83	99.84	99.82	99.91	99.84	99.59	99.66	99.84	99.97
% of total Si condensed	99.25	99.31	99.24	99.31	99.08	99.45	99.31	98.90	99.02	99.31	99.71
% of total Fe condensed	92.98	93.76	93.88	93.76	99.56	94.70	93.76	89.98	93.52	93.76	97.16

* Denotes the standard case described in detail in the text.

cantly higher in the 900 K liquid than their values in all of the olivine for each thermal history. Small negative δ-values in the bulk droplets reflect incomplete recondensation of Mg, Si and Fe; δ^{25}Mg and δ^{29}Si for the high-temperature case and δ^{56}Fe for the other cases lie outside the ranges in chondrules (Fig. 1).

5.3.2. With some nuclei remaining; Type I PO simulations

For a given thermal history, the model run for the Type I precursor yields almost the same evaporation curves as that for the Type II precursor, when nuclei are assumed to survive in both calculations. Results for the fast heating thermal history are shown in Fig. 14. As for the analogous Type II runs, fayalite histograms have dominant peaks at $X_{Fa} \leqslant 0.01$, with long, very low tails out to beyond $X_{Fa} = 0.30$ (Fig. 14b). Also like the Type II PO runs and for the same reasons, the mean X_{Fa} is highest in the high temperature case, 0.077, and lower, *e.g.*, 0.018 to 0.019 in the fast and slow heating cases, respectively. As in the other cases investigated, Table 4 shows that very large variations of δ^{25}Mg (~2.1–33‰), δ^{29}Si (~4.6–6.9‰) and δ^{56}Fe (~17–27‰) are recorded by the olivine in all three thermal histories. For each thermal history, the isotopic compositions of the 900 K liquid lie within the ranges recorded by olivine except for δ^{56}Fe, which is significantly more positive than all of the olivine in the fast- and slow-heating cases. The bulk droplets again have small negative δ-values due to incomplete recondensation of Mg, Si and Fe; δ^{25}Mg and δ^{29}Si for the high-temperature case again lie outside the ranges in chondrules (Fig. 1).

In summary, regardless of whether the droplets have Type I or Type II chemical compositions, and whether or not nuclei survive heating, large internal isotopic heterogeneities are recorded, even when the droplet bulk compositions do not show large deviations from normal isotopic composition, in all three thermal histories.

5.4. Sensitivity of results to model assumptions

The robustness of the chemical and isotopic results was tested by re-running the model many times, in each case varying only one of the assumed parameters relative to those used in the standard case. Some parameters, such as the degrees of dust and water enrichment, have a major effect on the thermal history as well as the droplet composition, but their values were selected to suppress evaporation significantly and to yield the desired FeO contents, respectively. With those two parameters fixed, the variation of

Author's personal copy

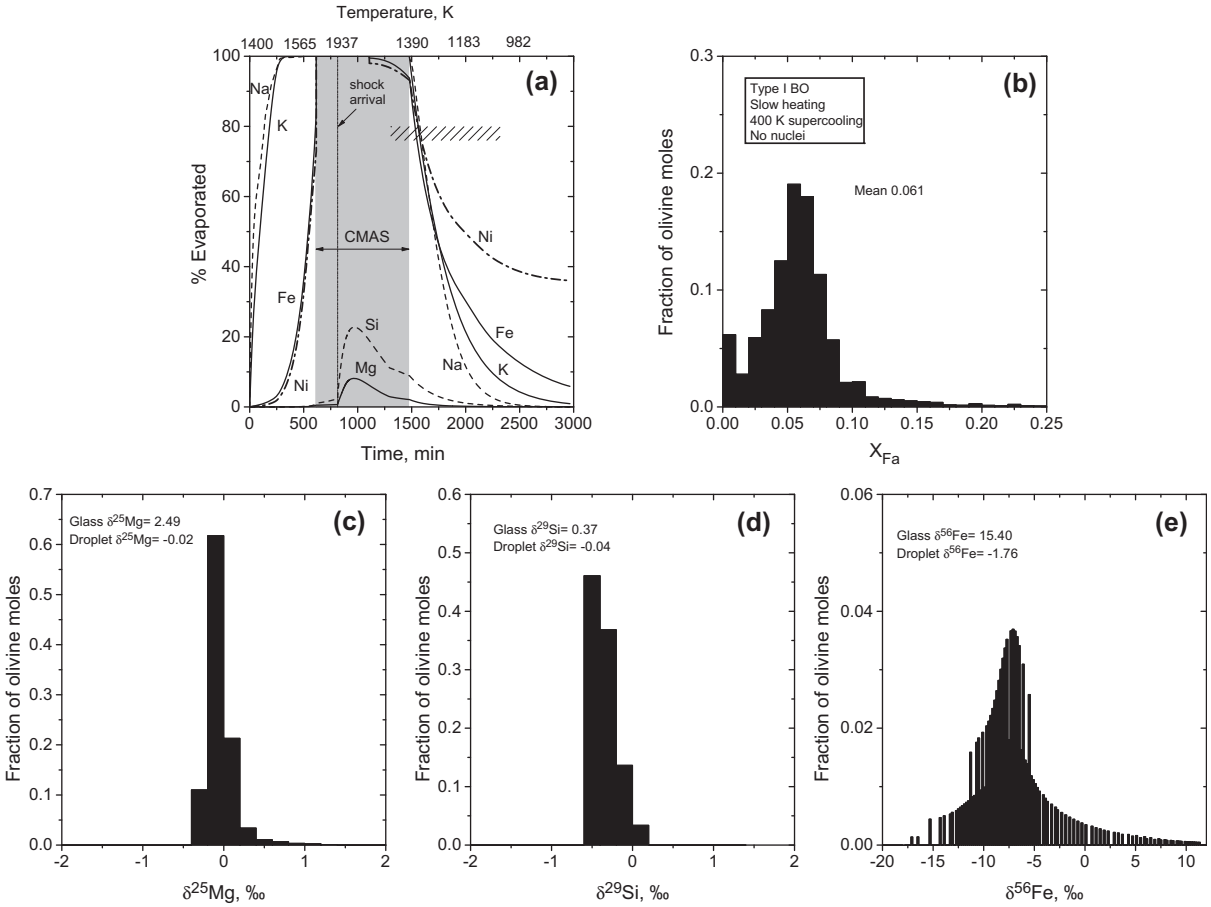

Fig. 13. Computed evaporation curves (a) and histograms of fayalite content (b), δ^{25}Mg (c), δ^{29}Si (d) and δ^{56}Fe (e) for a Type I precursor exposed to the slow heating thermal history, assuming no solid nuclei survive and 400 K of supercooling. Cross-hatching in (a) as in Fig. 4.

model results at various thermal histories was discussed above. Only those parameters that have little effect on the thermal history are considered here. A summary of the results is found in Table 5.

5.4.1. Initial redox state of the droplet

When the starting material is assumed to form at log f_{O_2} = IW-3.1 and IW-2.1 instead of IW-2.6, the droplet begins with 12 and 8.9 wt.% metallic Fe,Ni, respectively, instead of 11 wt.%. The initial FeO contents are 1.5 and 5.6 wt.%, instead of 2.8 wt.%. In these examples, the variations in oxygen content of the precursor are complementary to those of the gas with which it is assumed to have equilibrated at 1400 K, and the composition of the dust with which the systems are enriched is always the same. Thus, the total oxygen content of the system is the same in all three cases. Because metallic Fe generally evaporates slightly faster than does FeO from the silicate liquid, the difference in initial mineralogy leads to total loss of Fe in 189 min at the lowest f_{O_2} and 217 min at the highest f_{O_2}, compared to 201 min in the standard case. Evaporation rates of the other elements are almost identical in the three cases. Since the bulk chemical composition of the system is the same in all three cases and the properties of the olivine are established after recondensation of Fe begins, the differences in the histograms of fayalite content, δ^{25}Mg, δ^{29}Si and δ^{56}Fe of the olivine are imperceptible, as can be inferred from Table 5.

5.4.2. Amount of surface metal

When the proportion of the total metal grains assumed to reside on the surface of the droplet is increased by a factor of 3, to 15%, metal occupies 19% of the surface area of the droplet initially and is vastly over-represented compared to its volume%. Because of the much higher surface area of metallic iron, total evaporation of iron occurs ten minutes sooner than in the standard case, at 191 min. During recondensation, the higher surface area of metal causes iron and nickel to recondense more quickly and oxidation of metal to increase the FeO content of the silicate liquid more quickly than in the standard case. As a result, although the shape of the histogram of fayalite content of olivine is almost identical to that for the standard case, the mean X_{Fa} increases from 0.171 to 0.193. Evaporation and recondensation curves for the other elements are almost the same as in the standard case. As can be inferred from Table 5, histograms of δ^{25}Mg and δ^{29}Si are almost identical to those for the standard case, while that for

Author's personal copy

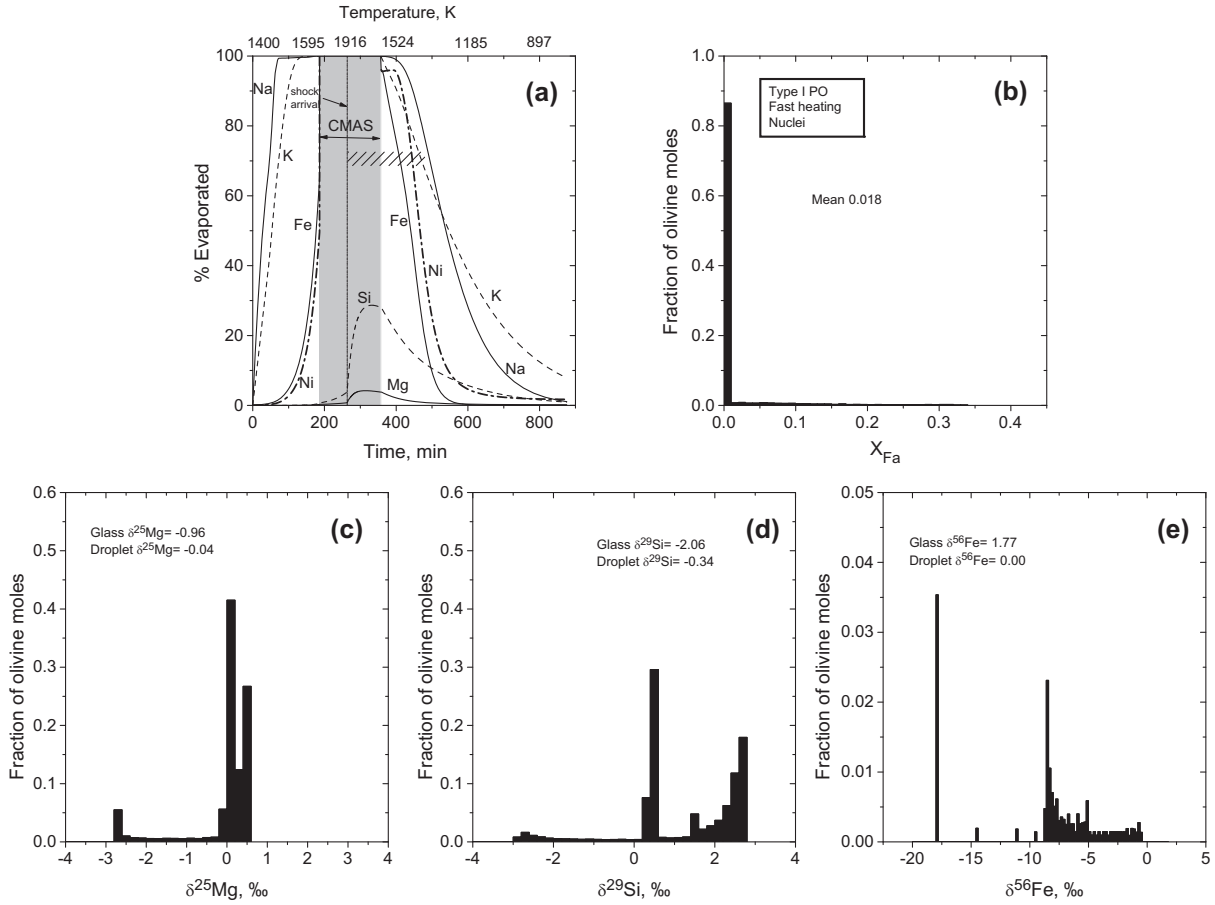

Fig. 14. Computed evaporation curves (a) and histograms of fayalite content (b), δ^{25}Mg (c), δ^{29}Si (d) and δ^{56}Fe (e) for a Type I precursor exposed to the fast heating thermal history, when solid nuclei are assumed to survive. Cross-hatching in (a) as in Fig. 4.

Table 6
Changes due to diffusion of the chemical and isotopic compositions of the cores of 50 μm-thick olivine plates in Type II BO simulations.

Thermal history		X_{Fa}		δ^{25}Mg (‰)		δ^{29}Si (‰)		δ^{56}Fe (‰)	
		Core	Rim	Core	Rim	Core	Rim	Core	Rim
Fast heating	Growth zoning	0.088	0.335	−0.35	1.01	−0.35	−0.44	−7.65	1.83
	After diffusive relaxation	0.144		−0.27				−5.56	
High Temperature	Growth zoning	0.011	0.402	−4.24	11.86	−3.17	−1.27	−18.00	1.68
	After diffusive relaxation	0.106		−3.39				−8.11	
Slow Heating	Growth zoning	0.086	0.407	−0.26	0.72	−0.30	0.28	−6.80	4.47
	After diffusive relaxation	0.181		−0.07				−2.64	

δ^{56}Fe is shifted to more positive values because of the greater degree of Fe recondensation.

5.4.3. Oxidation rate

When γ_O, the oxidation coefficient, is decreased by a factor of 3 at all temperatures, *i.e.*, to 0.1 at 2000 K, more of the iron evaporates as metal, so total iron loss occurs more quickly, in 191 min, than in the standard case, 201 min. When γ_O is increased by a factor of 2 at all temperatures, *i.e.*, to 0.6 at 2000 K, total iron loss occurs more slowly, in 210 min. Evaporation curves for the other elements are nearly identical to those in the standard case. Because of the relatively high ambient f_{O_2} during recondensation in all cases, almost all of the iron recondenses as FeO, so the oxidation rate has little effect on the condensation rate of iron or any other element. As a result, histograms of fayalite content, δ^{25}Mg, δ^{29}Si and δ^{56}Fe of olivine are nearly identical in all three cases, as can be inferred from Table 5.

5.4.4. Degree of supercooling

When the temperature of incipient olivine crystallization is assumed to be 200 K below its equilibrium crystallization temperature, olivine first appears before the beginning of

Author's personal copy

Table 7
Effects of diffusion on chemical and isotopic profiles computed for olivine spheres in Type II PO simulations.

Thermal history	Grain radius (μm)		X_{Fa}			$\delta^{25}Mg$ (‰)			$\delta^{29}Si$ (‰)			$\delta^{56}Fe$ (‰)		
			r_1*	r_2*	r_3*	r_1	r_2	r_3	r_1	r_2	r_3	r_1	r_2	r_3
Fast heating	50	$r_1 = 46.6$; $r_2 = 48.6$; $r_3 = 49.2$ μm												
Cooling rate = 114 K/hr		Growth zoning	0.038	0.204	0.267	0.08	−2.06	−2.29	1.94	−1.47	−2.23	−8.63	−7.29	−5.66
		With diffusion during growth	0.050	0.247	0.327	−0.04	−2.18	−2.25				−8.57	−6.08	−4.49
		With diffusion during and after growth	0.050	0.248	0.344	−0.04	−2.18	−2.23				−8.57	−6.06	−4.08
	75	$r_1 = 69.9$; $r_2 = 72.9$; $r_3 = 73.8$ μm												
		Growth zoning	0.038	0.204	0.267	0.08	−2.06	−2.29	1.94	−1.47	−2.23	−8.63	−7.29	−5.66
		With diffusion during growth	0.041	0.223	0.297	0.06	−2.14	−2.27				−8.62	−6.74	−5.01
		With diffusion during and after growth	0.041	0.223	0.299	0.06	−2.14	−2.27				−8.62	−6.74	−4.96
	100	r_1=93.1; r_2=97.2; r_3=99.0 μm												
		Growth zoning	0.038	0.204	0.305	0.08	−2.06	−2.28	1.94	−1.47	−2.47	−8.63	−7.29	−4.79
		With diffusion during growth	0.039	0.214	0.327	0.08	−2.10	−2.26				−8.63	−6.99	−4.46
		With diffusion during and after growth	0.039	0.214	0.330	0.08	−2.10	−2.25				−8.63	−6.99	−4.39
High-Temperature	50	r_1=40.6; r_2=45.2; r_3=49.0 mm												
Cooling rate = 154 K/hr		Growth zoning	0.073	0.167	0.335	−7.50	−3.51	3.50	−4.95	−5.75	−4.61	−8.62	−7.25	−2.76
		With diffusion during growth	0.074	0.168	0.337	−7.50	−3.46	3.58				−8.62	−7.21	−2.71
		With diffusion during and after growth	0.074	0.168	0.337	−7.50	−3.46	3.58				−8.62	−7.21	−2.71
	75	r_1=60.8; r_2=67.8; r_3=74.1 μm												
		Growth zoning	0.073	0.167	0.360	−7.50	−3.51	4.73	−4.95	−5.75	−4.35	−8.62	−7.25	−2.09
		With diffusion during growth	0.073	0.167	0.360	−7.50	−3.51	4.74				−8.62	−7.25	−2.09
		With diffusion during and after growth	0.073	0.167	0.360	−7.50	−3.51	4.74				−8.62	−7.25	−2.09
	100	r_1=81.1; r_2=90.4; r_3=98.9 μm												
		Growth zoning	0.073	0.167	0.360	−7.50	−3.51	4.73	−4.95	−5.75	−4.35	−8.62	−7.25	−2.09
		With diffusion during growth	0.073	0.167	0.360	−7.50	−3.51	4.73				−8.62	−7.25	−2.09
		With diffusion during and after growth	0.073	0.167	0.360	−7.50	−3.51	4.73				−8.62	−7.25	−2.09
Slow Heating	50	r_1=47.1; r_2=48.6; r_3=49.0 μm												
Cooling rate = 27 K/hr		Growth zoning	0.074	0.192	0.232	0.03	−0.98	−1.14	1.65	−0.69	−1.31	−7.85	−6.31	−5.47
		With diffusion during growth	0.139	0.271	0.301	−0.36	−1.12	−1.15				−6.16	−3.98	−3.36
		With diffusion during and after growth	0.143	0.351	0.427	−0.36	−1.14	−1.16				−5.85	−2.11	−0.84
	75	r_1=71.5; r_2=72.9; r_3=74.1 μm												
		Growth zoning	0.074	0.192	0.264	0.03	−0.98	−1.16	1.65	−0.69	−1.67	−7.85	−6.31	−4.44
		With diffusion during growth	0.097	0.238	0.309	−0.11	−1.09	−1.16				−7.17	−4.88	−3.20
		With diffusion during and after growth	0.097	0.258	0.437	−0.11	−1.09	−1.16				−7.17	−4.17	−0.65
	100	r_1=94.3; r_2=97.1; r_3=98.8 μm												
		Growth zoning	0.074	0.192	0.264	0.03	−0.98	−1.16	1.65	−0.69	−1.67	−7.85	−6.31	−4.44
		With diffusion during growth	0.083	0.219	0.298	−0.02	−1.06	−1.16				−7.57	−5.49	−3.46
		With diffusion during and after growth	0.083	0.222	0.392	−0.02	−1.06	−1.16				−7.57	−5.35	−1.49

* r_1, r_2 and r_3 are the distances from the center of the crystal.

Author's personal copy

iron recondensation; with 400 K of supercooling, it appears after 84% of the iron has recondensed, instead of after 36% recondensation of iron in the standard case (300 K). Because of this, the liquid contains 0, 4.1 and 6.1 wt.% FeO when olivine solidification begins for 200, 300 and 400 K of supercooling, respectively, causing histograms of olivine composition to be shifted to progressively higher X_{Fa}. At supercoolings of 200, 300 and 400 K, histograms have minimum X_{Fa} of 0.0, 0.09 and 0.17, mean X_{Fa} of 0.12, 0.17 and 0.20, respectively, and have long tails out to $X_{Fa} = 0.40$. When olivine begins to crystallize, the chemical composition of the liquid and, consequently, equilibrium vapor pressures are affected. As a result, progressively greater degrees of recondensation of Mg, Si and Fe and lesser degrees of Na and K occur at a given temperature with increasing supercooling, shifting slightly the curves of δ^{25}Mg, δ^{29}Si and δ^{56}Fe of the equilibrated fraction with time. The major effect on the histograms of isotopic composition is due to the shift of the temperature range over which formation of olivine samples the isotopic composition of the equilibrated fraction with increasing supercooling. For example, since δ^{56}Fe of the equilibrated fraction becomes more positive with time during olivine crystallization, progressive delay of olivine causes the minimum, mean and maximum δ^{56}Fe recorded by olivine to be progressively more positive with increasing supercooling, as seen in Table 5.

Thus, the prediction that large, internal isotopic heterogeneities will be recorded in objects formed in this way is independent of the degree of supercooling to within a range of at least 200 K; the areal percent of metal on the droplet surface to within a factor of at least two; the oxidation state of the precursor as long as significant amounts of both metal and Fe^{2+} are present; and the specific oxidation rate of metallic iron within a factor of at least six as long as the resulting oxidation time is comparable to the thermal cycling time of the droplet in shock wave thermal histories.

5.5. Preservation of internal chemical and isotopic heterogeneities

Because Fe, Mg and Si are recondensing into the liquid of the model droplets while olivine crystallizes from it, successively solidified batches of olivine record a sequence of instantaneous isotopic compositions of the liquid. What has not yet been demonstrated is whether the resulting isotopic zoning of individual olivine crystals would be preserved, or whether diffusion would erase isotopic heterogeneity in the time interval spent at relatively high temperatures during which crystal growth and post-growth cooling occurred, given the model cooling rates at which the droplets solidified. To study this possibility, the extent of modification, by diffusion, of isotopic compositions of specific points within model isotopic zoning profiles was calculated at the cooling rates at which the profiles were produced. The Type II bulk composition runs were investigated at each thermal history.

5.5.1. Olivine plates formed in BO simulations

For the BO simulations, growth of a 50 μm-thick plate symmetrically about a central axis was assumed to begin and end when olivine crystallization began and ended. The relative thickness of each layer normal to the axis was calculated from the relative volume of olivine of each composition computed to have crystallized from the liquid for each thermal history. Profiles of X_{Fa}, δ^{25}Mg, δ^{29}Si and δ^{56}Fe calculated in this way are shown in Fig. 15 for a plate that grew in the slow heating case. Fractional relaxations computed from Fig. 12 of Chakraborty and Ganguly (1991) were incorporated into a finite difference scheme in which the concentration of each isotope at the core of the plate was recalculated in incremental steps to allow for diffusion during growth of each successive layer of the crystal. Since the latter figure applies to a spherical crystal with fixed surface concentration and an initial, linear, core-rim concentration gradient, while the crystal in the present case is a plane sheet, this technique may overestimate the extent of diffusive relaxation. No significant difference was found, however, between fractional relaxations calculated from Crank (1989) for spherical and plane sheet geometries in solutions for the concentration profiles for initially homogeneous crystals with fixed boundary concentrations, at the Dt/a^2 values of the present problem. It is thus highly unlikely that the extent of diffusive relaxation has been

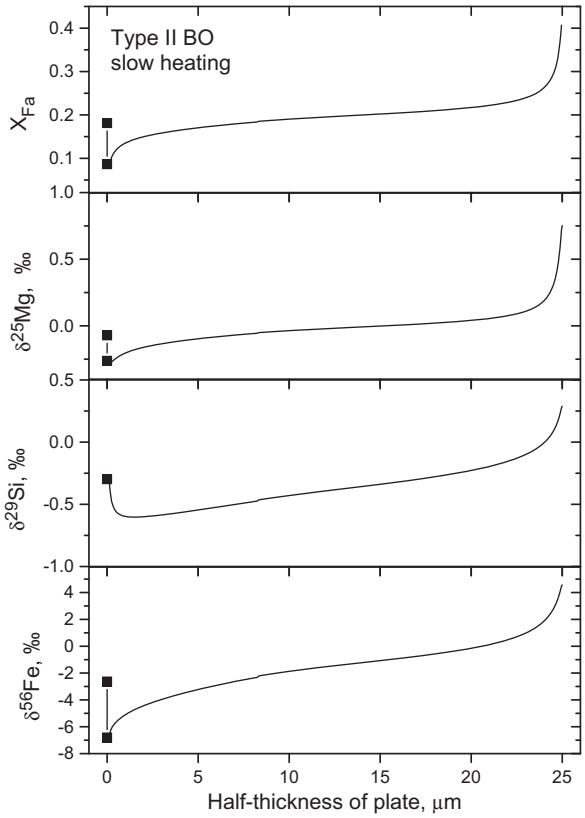

Fig. 15. Calculated chemical and isotopic profiles in a 50 μm-thick olivine plate that grew from the beginning to the end of olivine crystallization in the slow heating thermal history in a Type II BO simulation. The curve in each profile does not include the effects of diffusion. Points at the core show displacements due to the effect of diffusion during crystal growth and post-growth cooling.

Author's personal copy

overestimated significantly. A similar technique was used to calculate the additional relaxation after growth of olivine ceased, assuming that the surface maintained instantaneous chemical and isotopic equilibrium with the liquid. Because the gradients of all isotopes of each of Mg and Fe have the same sign, diffusion of each isotope occurs primarily by Mg and Fe exchanging places with one other. Thus, Fe–Mg interdiffusion coefficients (Dohmen and Chakraborty, 2007) were used in these calculations for the change in X_{Fa}, δ^{25}Mg and δ^{56}Fe. Diffusion coefficients for Si (Chakraborty, 2010) are so small at these temperatures that δ^{29}Si changes imperceptibly during the model cooling times. The composition changes are shown for all three thermal histories on Table 6, and in Fig. 15 for the slow heating case, where diffusion effects are greatest. Because X_{Fa} and δ^{56}Fe increase toward the crystal edge, Fe diffuses inward, raising XFa and δ^{56}Fe of the core significantly and displacing Mg outward.

Although this technique does not allow quantitative evaluation of the effects of diffusive relaxation at any point other than the core of the olivine, it can be assumed that δ^{29}Si will be unchanged throughout the crystal. Because each of X_{Fa}, δ^{25}Mg and δ^{56}Fe increase monotonically from core to rim, it can also be assumed that diffusion will cause each to change in the same direction throughout the crystal as they do in the core. Thus, comparing the post-diffusion core value of X_{Fa}, δ^{25}Mg or δ^{56}Fe with its respective pre-diffusion rim value gives a lower limit to its total variation within the crystal. For all three thermal histories, Table 6 shows that preservation of large isotopic variations is expected within 50 μm-thick olivine plates that formed in shock wave thermal histories similar to those modeled here, even after diffusive relaxation. These amount to $\geqslant$5‰ in δ^{56}Fe, $\geqslant$0.1‰ in δ^{29}Si and $\geqslant$several tenths of a ‰, and possibly much more in the high-temperature case, for δ^{25}Mg. In most cases, isotopic variations would be detectable with a microbeam instrument capable of measuring isotopic mass-fractionations of Mg and Si to ±0.1‰/amu and of Fe to ±0.5‰/amu if a 10 μm-diameter analytical spot were located in the center of a plate and another at its edge.

Since diffusive relaxation is negligible for Si, significant differences in the mean δ^{29}Si of olivine and glass (Table 4) would be detectable. As can be inferred from Table 6 and Fig. 15, post-growth diffusion of Fe into the grains leaves their mean δ^{56}Fe lower than in their respective host liquids (Table 4) whose δ^{56}Fe would be almost unaffected by this process. Thus, Fe isotopic differences between olivine and glass would also be detectable. Whether olivine-glass isotopic differences would be detectable for Mg is less certain, as Fe–Mg exchange may add large amounts of relatively light Mg from olivine to a relatively small amount of heavy Mg in the liquid, depending on the olivine grain size distribution in the droplet.

5.5.2. Olivine spheres formed in PO simulations

A similar procedure was followed for the PO simulations, except that radial growth of 50-, 75- and 100-μm radius spheres was assumed to begin and end when olivine growth began and ended. As seen in Fig. 16, increases in X_{Fa} and δ^{56}Fe are restricted to the outermost few μm in many cases, as FeO enters olivine relatively late in its crystallization history in these simulations. After smoothing out fine-scale complexities of the growth profiles by binning data for adjacent shells, the effect of diffusive relaxation on the growth profiles was calculated using Equation 6.21 of Crank (1989), a solution of the diffusion equation for an initially homogeneous sphere with fixed surface concentration. This solution was incorporated into a finite difference scheme in which the concentration of each isotope was recalculated in incremental steps to allow for diffusion during growth of each successive concentric shell of the crystal as well as during post-growth interaction with residual liquid. Use of the above equation overestimates the flux into or out of the crystal, and hence the extent of relaxation, since the initial condition for the present problem is a steep gradient near the grain boundary, rather than a discontinuity at the boundary. Slope reversals in the δ^{25}Mg, δ^{29}Si and δ^{56}Fe profiles were avoided by restricting calculations to regions exterior to the points of reversal.

The effect of diffusive relaxation was calculated for the innermost Fe-bearing shell (r_1), a point ~1 μm from the edge of the crystal (r_3), and a third point midway between the other two (r_2). The computed effects on X_{Fa}, δ^{25}Mg, δ^{29}Si and δ^{56}Fe are shown for all thermal histories and grain sizes on Table 7, and in Fig. 16 for a 100-μm sphere that grew in the high-temperature case. For a given grain size, the thickness of the entire Fe-containing zone is greatest for the high-temperature thermal history and least for the slow heating case. Thus, for each grain size, the points considered are furthest apart in the former and closest together in the latter. Diffusive relaxation effects are greatest in the smallest grains at each thermal history and, for a given grain size, in the thermal history with the lowest cooling rate, the slow heating case. Except for 100 μm grains in the fast heating case and all grain sizes in the high-temperature thermal history, X_{Fa} increases significantly even in the innermost FeO-bearing zone. In all cases, Si diffusion coefficients are so small that the δ^{29}Si profiles are unaffected by diffusive relaxation.

Table 7 shows that, even within the smallest olivine grains considered that cooled at the slowest rate, variations in δ^{25}Mg, δ^{29}Si and δ^{56}Fe of 0.8, ~3 and 5‰, respectively, would be preserved after diffusive relaxation. As seen in the Table for this case, however, the isotopic variations are separated by <3 μm, making them difficult to measure. If olivine in PO chondrules formed in shock wave thermal histories similar to those modeled here, variations in δ^{25}Mg, δ^{29}Si and δ^{56}Fe would be detectable in any grain large enough to have an FeO-bearing zone with a radial extent greater than the diameter of the analytical spot of a microbeam instrument, provided the instrument can measure isotopic mass-fractionations in these elements to ±0.5‰/amu. For a beam diameter of 10 μm, such isotopic variations would be measurable in olivine grains $\geqslant$75 μm in radius if they formed in the high-temperature thermal history but in none of the grain sizes if they formed in the other two thermal histories. Fig. 16, for example, shows that the outer 10 μm of a 100 μm olivine grain formed in

Author's personal copy

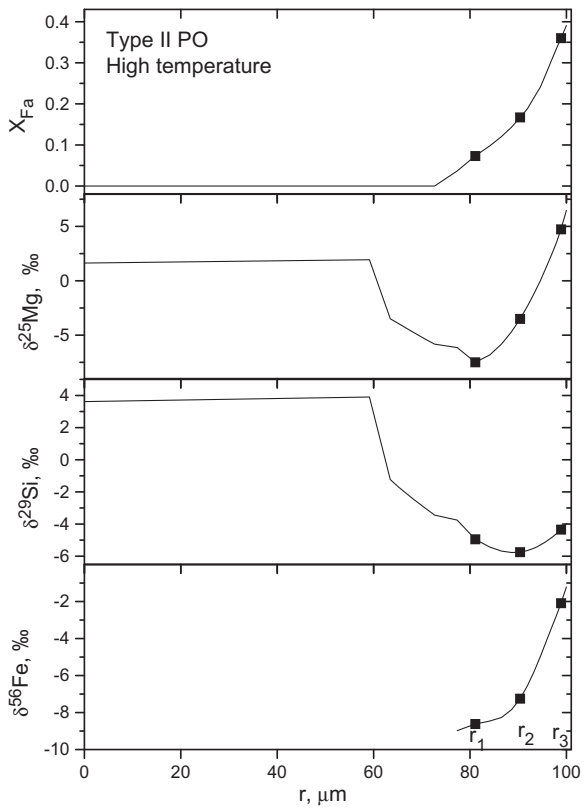

Fig. 16. Calculated chemical and isotopic profiles in a 100 μm-radius olivine crystal that grew from the beginning to the end of olivine crystallization in the high-temperature thermal history in a Type II PO simulation. For each parameter plotted, the curve is the growth profile, which does not include the effects of diffusion. r_1, r_2 and r_3 are locations where effects of diffusive relaxation were calculated. Dark squares show compositions at these points after taking into account diffusion during crystal growth and post-growth cooling. In this case, the dark squares lie on the growth profiles, indicating that diffusive relaxation is negligible. Discontinuities along curves are due to averaging of adjacent bins.

the high-temperature thermal history would have δ^{25}Mg, δ^{29}Si and δ^{56}Fe of ~+1, −5, and −4‰, respectively, while δ^{25}Mg and δ^{29}Si would be ~2 and 3.5‰, respectively, throughout much of the interior of the grain and δ^{56}Fe would be ~−8‰ in the 10 μm thick region immediately beneath that zone. For a beam diameter of 5 μm, isotopic variations would also be measurable in 50 μm-radius grains formed in the high-temperature thermal history and 100 μm grains formed in the fast and slow heating cases.

For the same reasons as in the BO simulations, measurable differences would be preserved between the mean δ^{29}Si of the olivine and that of the glass (Table 4) in the PO cases for all three thermal histories, and preservation of olivine-glass isotopic differences for Mg is less certain. Even if the mean δ^{56}Fe of olivine in each Type II PO simulation shown in Table 4 were modified by the maximum diffusive change at any location within the grain for each grain size shown on Table 7, a measurable difference would persist between the modified mean δ^{56}Fe of the olivine and δ^{56}Fe of the glass for every grain size considered at each thermal history.

6. DISCUSSION

6.1. Searches for internal Mg and Fe isotopic heterogeneity within chondrules

Young et al. (2002) used laser ablation MC-ICPMS to measure Mg isotope ratios in 100 μm-diameter spots within four Allende chondrules. While variations in δ^{25}Mg of up to 1.6‰ were observed from spot to spot within individual chondrules, and cannot be explained by the measurement uncertainty of ±0.15‰, they were attributed to core-rim differences in the degree of secondary alteration. Because different olivine/glass proportions were sampled from spot to spot, it is unlikely that differences in δ^{25}Mg of the sizes seen in Table 4 exist between olivine and glass in any of the chondrules studied. In an ion microprobe study using 12 μm-diameter spots, Nagahara et al. (2008) did not detect differences >1‰ in δ^{25}Mg from one olivine crystal to another or from one region of glass to another within individual Semarkona chondrules.

The only available iron isotopic measurements of regions within individual chondrules are the ion microprobe data of Alexander and Wang (2001). In that work, δ^{57}Fe (relative to ^{56}Fe) was measured in 20–25 μm-diameter spots within olivine grains in nine Chainpur chondrules, representing Type I, Type II, PO and BO varieties. Multiple olivine analyses were made in four of these objects. Observed δ^{57}Fe ranges from −0.7 to +4.3‰, although 2σ analytical uncertainties ranging from several ‰ for forsterite-rich olivine to ~±1‰ for more FeO-rich spots render all of these measurements indistinguishable from normal Fe isotopic composition. Had these chondrules formed in shock wave thermal histories similar to those investigated here, Table 4 shows that, in most cases, olivine within them would be expected to have mean Fe isotopic compositions that exhibit negative mass-fractionations of 1–3‰/amu. It is likely that such isotopic compositions would have been measurable in the work of Alexander and Wang (2001), especially in the more FeO-rich samples, but were not observed.

Although the database of point analyses of Mg and Fe isotopic compositions within individual chondrules is sparse, there is no evidence of mass-fractionations of these elements of the sizes predicted if chondrules formed in shock wave thermal histories such as those investigated here. Just as bulk chondrules have near-normal Mg and Fe isotopic compositions, so too, it appears, do their constituents.

In addition, Alexander et al. (2000) and Alexander and Grossman (2005) performed ion microprobe analyses of δ^{41}K in spots within Bishunpur and Semarkona chondrules, and the mean δ^{41}K of each chondrule is plotted in Fig. 1c. While the values range from ~−5.5 to + 12‰, it is seen that ~two-thirds of the chondrules have positive δ^{41}K. The positive values are incompatible with the shock wave thermal histories explored herein.

Author's personal copy

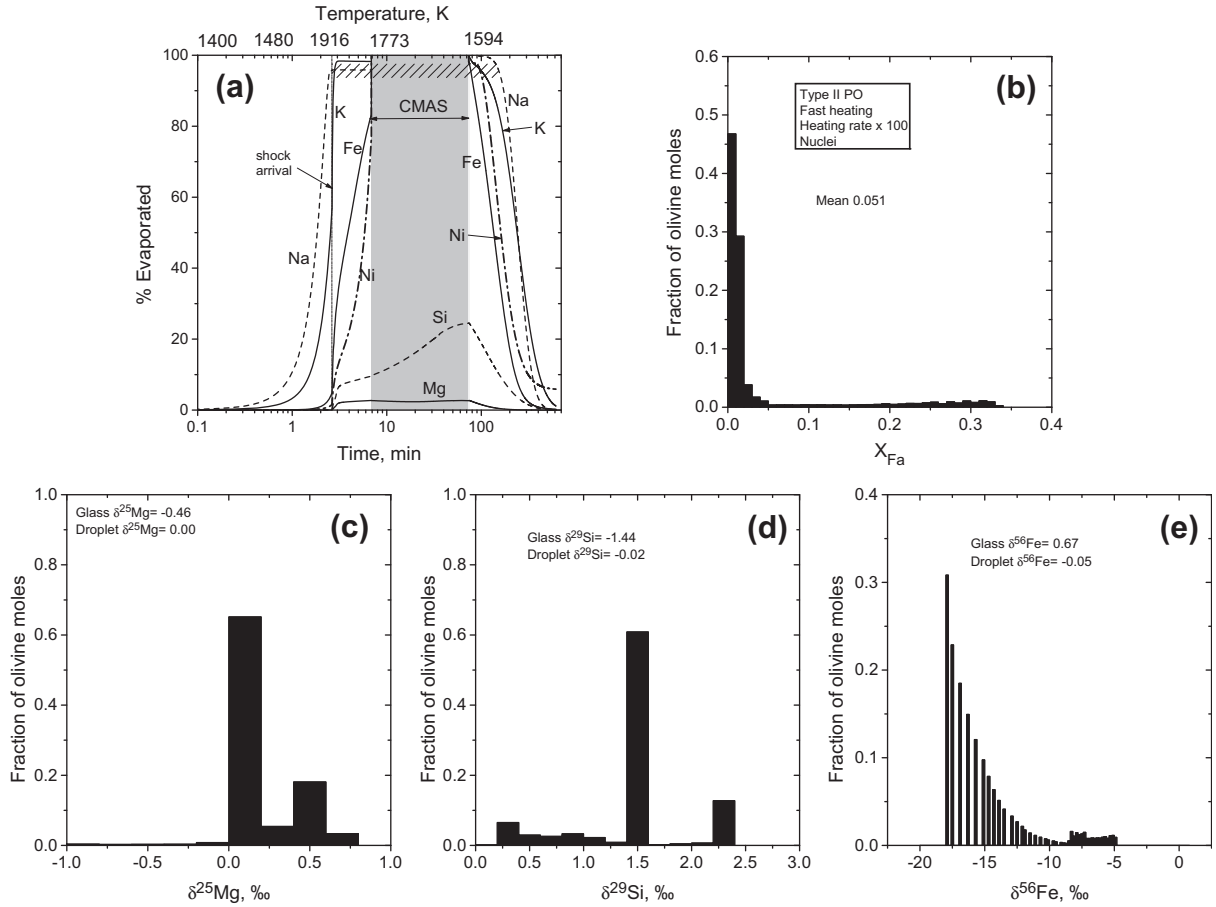

Fig. 17. Computed evaporation curves (a) and histograms of fayalite content (b), δ^{25}Mg (c), δ^{29}Si (d) and δ^{56}Fe (e) for a Type II precursor exposed to the fast heating thermal history, except for a reduction by a factor of 100 in the time required to reach each temperature, and its corresponding P^{tot}, from 1400 K through the inflection temperature. Solid nuclei are assumed to survive. All Fe evaporates, mostly during cooling. Note logarithmic scale in (a). Cross-hatching in (a) as in Fig. 4.

6.2. Thermal histories that prevent development of intra-chondrule isotopic variations

Because droplets formed in the shock wave thermal histories investigated here are predicted to have internal isotopic variations unlike those of chondrules, the question that remains is what thermal histories would lead to objects that do have the properties of chondrules. It is clear that evaporation must be suppressed. One of the standard approaches for accomplishing this, heating protochondrules in a dust-enriched region, was employed in all of the above simulations. It was seen that enrichment of dust by a factor of 600 relative to solar composition is capable of promoting recondensation on the time-scale of chondrule cooling and thus preventing development of large Mg, Si and Fe isotopic mass-fractionations in the bulk droplet that results. In the context of shock wave models, however, it was also seen that evaporation was not totally prevented in this approach, causing isotopic variations to be preserved by olivine that fractionally crystallized before recondensation was complete. The answer cannot be simply to find thermal histories with shorter cooling times, as the cooling rates in the models employed match those of many chondrules, and faster cooling rates would not result in more rapid recondensation anyway. Nor can the answer be thermal histories with much lower peak temperatures, as chondrule textures require near-liquidus peak temperatures.

In an attempt to show that thermal histories with shorter heating times are required, an evaporation calculation was conducted identical to that for the Type II composition subjected to the fast heating history with surviving nuclei, except that the heating time-scale was shortened by a factor of 100. In this calculation, the time required to reach each temperature (and its corresponding P^{tot}) in the profile from 1400 K through the inflection temperature was reduced by a factor of 100 compared to that for the original run, shown in Figs. 2a and 3a. Even with this short heating time, 3 min, all Fe is lost but mostly during cooling, as seen in Fig. 17a, and the familiar pattern of large isotopic variations are predicted for olivine, as seen in Fig. 17c–e. It is clear that simply shortening the heating time is insufficient to eliminate this phenomenon.

Although all of the above calculations assume a dust enrichment factor of 600 relative to solar composition, exceeding the enhancement achieved in vertical settling models by a factor of five (Cassen, 2001), chondrules pro-

Author's personal copy

vide evidence for even greater enrichments. Alexander et al. (2008) argued that the Na_2O concentrations of the most FeO-poor olivine crystal cores in 15 Types I and II PO and BO chondrules in Semarkona, 0.0007–0.0133 wt.%, imply that the chondrule liquids contained ~1–2 wt.% Na_2O when olivine began to crystallize. From Na vapor pressures calculated for these concentrations at liquidus temperatures, Alexander et al. (2008) estimated that the ambient pressures of Na necessary to hold these concentrations in solution in the melt require nebular dust concentrations of 72–9080 g/m^3 at 10^{-7} bar. In the present work, Eq. (6) was used to repeat this calculation for the composition of each of the chondrules of Alexander et al. (2008) at its liquidus temperature for each of two values of log f_{O_2}, IW and the average log f_{O_2}, IW-1.3, where FeO-bearing olivine crystallizes in the standard case herein. The ratio of the vapor pressure of Na to its partial pressure in a system of solar composition at $P^{tot} = 10^{-3}$ bar is 9×10^4–4×10^5 at IW, and 2–8 $\times 10^5$ at IW-1.3; at 10^{-7} bar, the ratios are 1–6 $\times 10^9$ and 3×10^9–1×10^{10}, respectively. These are the same as the enrichment factors of dust relative to gas compared to a system of solar composition that would be needed to maintain the Na contents of the chondrule liquids at their inferred levels at the stated conditions. Alternatively, if, as assumed by Alexander et al., the chondrules equilibrated their Na contents at liquidus temperatures after 10% of the Na had evaporated from them, the necessary dust enrichments would be 9×10^5–4×10^6 at IW and 2–8 $\times 10^6$ at IW-1.3 at P^{tot}=10^{-3} bar; and 1–6 $\times 10^{10}$ at IW and 3×10^{10}–1×10^{11} at IW-1.3 at 10^{-7} bar. These are 10-10^6 times greater than the largest dust enrichments predicted to date in dynamic models of the solar nebula, even under the most extreme conditions (Cuzzi et al., 2001).

The same fast heating thermal history with the greatly shortened heating interval was assumed as in the previous case but 100 times more dust was added, to reach a dust enrichment of 6x10^4 relative to solar composition. In this case, only 0.45% of the Mg and 2.0% of the Si evaporated but 15.7% of the total Fe was still lost, as seen in Fig. 18a. Much smaller isotopic variations are recorded by olivine than in the corresponding Type II PO case subjected to the normal fast heating shock wave thermal history, as seen in Fig. 18c–e. Olivine crystallizes with minimum, maximum and mean δ^{25}Mg of −0.07, 0.07 and 0.00‰, δ^{29}Si of −0.07, 0.20 and 0.02‰, and δ^{56}Fe of −0.33, 1.77 and 0.14‰,

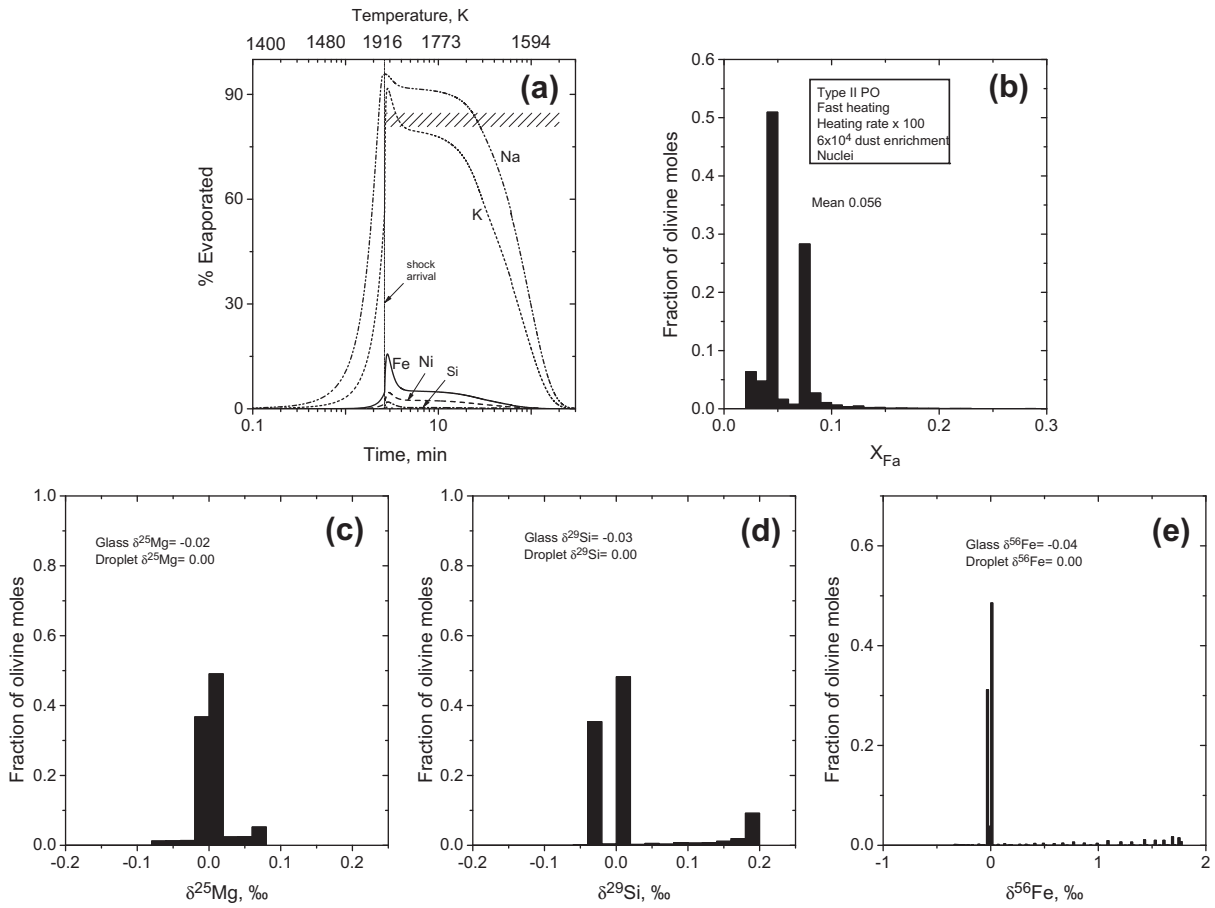

Fig. 18. Computed evaporation curves (a) and histograms of fayalite content (b), δ^{25}Mg (c), δ^{29}Si (d) and δ^{56}Fe (e) for a Type II precursor exposed to the fast heating thermal history, with the same accelerated heating rate as in Fig. 17 but with a dust enrichment of 6x10^4, instead of 600, relative to solar composition. Evaporation and consequent internal isotopic heterogeneity are suppressed. Note logarithmic scale in (a) and the reduced range of isotopic compositions compared to those in Figs. 9, 12–14 and 17. Cross-hatching in (a) as in Fig. 4.

Author's personal copy

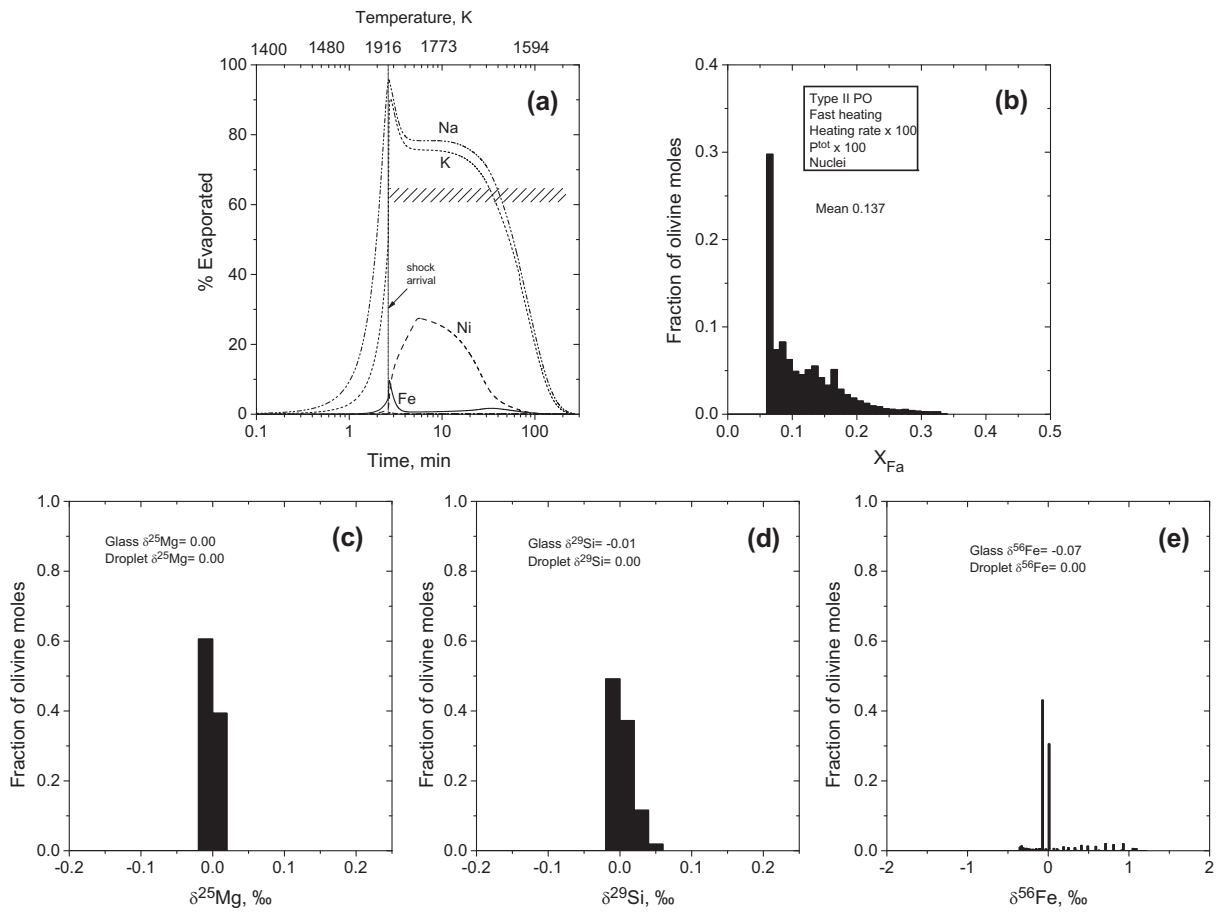

Fig. 19. Computed evaporation curves (a) and histograms of fayalite content (b), δ^{25}Mg (c), δ^{29}Si (d) and δ^{56}Fe (e) for a Type II precursor exposed to the fast heating thermal history, with the same accelerated heating rate as in Fig. 17, except that P^{tot} is 100 times higher at each temperature, reaching a maximum of 4×10^{-2} bar in the post-shock period. Evaporation and consequent internal isotopic heterogeneity are suppressed. Note logarithmic scale in (a) and the reduced range of isotopic compositions compared to those in Figs. 9, 12–14 and 17. Cross-hatching in (a) as in Fig. 4.

respectively. The liquid at 1000 K has δ^{56}Fe of only −0.04‰. Less than 10% of the olivine has δ^{56}Fe that differs by more than 1‰ from normal isotopic composition. If chondrules formed in this way, this would explain why internal isotopic heterogeneities have not been detected.

In another model run, exactly the same thermal history was assumed as in the previous case but, instead of increasing the dust enrichment, P^{tot} was increased by a factor of 100. In this case, the dust and water enrichments were 600 and 550, respectively, relative to solar composition, the heating time was made a factor of 100 shorter than for the fast heating thermal history in Fig. 2a, and P^{tot} was assumed to be a factor of 100 higher at each temperature than in the previous case. Thus, P^{tot} in the post-shock period is $4\text{x}10^{-2}$ bar. As can be seen in Fig. 19a, even less evaporation occurred than in the case of a dust enrichment of 6×10^4. Only 0.13% of the Mg, 0.45% of the Si and 9.6% of the total Fe evaporated. As a result, olivine crystallizes with minimum, maximum and mean δ^{25}Mg of −0.01, 0.01 and 0.00‰, δ^{29}Si of −0.02, 0.04 and 0.00‰, and δ^{56}Fe of −0.35, 1.10 and 0.09‰, respectively. The liquid at 1303 K has δ^{56}Fe of only −0.07‰. This is another way of producing chondrules with internal isotopic heterogeneities so small that they would not be detected.

It has been shown here that enrichment in water by a factor of ~550 relative to solar composition is necessary to account for the oxidation states of Types I and II chondrules. It has also been demonstrated that, if chondritic matter were heated to near-liquidus temperatures in minutes and cooled at tens to hundreds of degrees/hr, particular combinations of dust enrichment and P^{tot} would suppress evaporation sufficiently to prevent development of large isotopic heterogeneities within olivine + glass assemblages that form by solidification of the resulting droplets. Specifically, these are a dust enrichment of 600 relative to solar composition and $P^{tot} \sim 4 \times 10^{-2}$ bar, and dust enrichment of $6\text{x}10^4$ and $P^{tot} \sim 4 \times 10^{-4}$ bar. If the heating time were longer, the required enhancement in dust concentration or P^{tot} would be even greater. No way has yet been found to concentrate water by a factor > 10 or dust by a factor > 125 in large regions of the solar nebula (*e.g.*, Grossman et al., 2008), so the needed water and dust enrichments must be considered extreme. Impacts on planetesimals cause rapid melting and vaporization. In this local process, a frequent

Author's personal copy

one in the early solar system, it may have been possible to generate clouds of silicate droplets embedded in vapor that both contained the enormous enrichments of volatilized chondritic rock and cooled at the rates that are required to form chondrules. An impact-generated vapor plume highly enriched in condensable elements was also suggested by Campbell et al. (2002) to account for metal grains in CB chondrites, in that case by a factor of $\sim 10^7$ relative to solar composition, and Krot et al. (2005) suggested that chondrules in these meteorites formed in the same event. If the impacted planetesimals envisioned here had formed after nebular condensation of water ice, high, near-surface concentrations of this component could have also led to the required enrichment of water in the vapor plume.

7. CONCLUSIONS

Protochondrule material subjected to shock wave thermal histories calculated for dust and water enrichments of 600 and 550, respectively, would form objects containing large internal isotopic variations in Fe, Mg and Si, which are not observed in natural chondrules. Processes that subject protochondrule material to the same peak temperatures and cool it at the same rates as in the shock wave thermal histories investigated here, but heat it at rates that are a factor of 100 higher while doing so either at pressures or dust enrichments that are at least 100 times higher than those used to generate those thermal histories, would yield excellent environments for making chondrules with only minimal bulk Mg, Si and Fe isotopic fractionations and minimal internal isotopic heterogeneities in those elements. The combination of rapid heating and relatively high f_{O_2} with high densities of condensable elements suggests that clouds of liquid droplets and vapor generated by impact on ice-rich planetesimals could be such environments.

ACKNOWLEDGMENTS

We thank the Museum Nationale d'Histoire Naturelle and the National Museum of Natural History for thin sections of the Semarkona meteorite; P. Asimow, R.N. Clayton, H. Connolly, N. Dauphas, M. S. Ghiorso, R. Hewins, M. Humayun, R. Marcus, S. A. Kurtz and S. Weinbruch for helpful discussions; three anonymous reviewers for constructive comments; and S. Russell for editorial handling. Special thanks go to J. Ganguly for extensive assistance with diffusion calculations. This work was supported by NASA Grants NNX08AG27G (to FJC) and NNX08AE06G (to LG). F. Ciesla's work was also supported by funds from the Carnegie Institution of Washington.

APPENDIX A. CHEMICAL COMPOSITIONS OF OLIVINE AND GLASS IN PO CHONDRULES

Olivine compositions were measured in 7 Type I and 10 Type II PO chondrules by wavelength-dispersive analysis of three sections of the LL3.00 Semarkona and one section of the CO3.0 ALHA 77307. The Chicago Cameca SX-50 electron microprobe was used at an accelerating voltage of 15 kV and a beam current of 50 nA. To avoid bias, analyses were collected every 10 μm along linear, evenly-spaced, automated traverses. Peak counting times equaled background counting times and were 10 s for Mg and Si and 25 s for Mn, Cr and Fe, allowing collection of ~40 analyses per hour. The traverses yielded 43–415 stoichiometric (~1 Si, 3.00 ± 0.05 total cations per four oxygen anions) olivine analyses for each histogram. The full range of compositions and patterns of the Type Is and IIs are shown by 6 histograms in each of Fig. A-1a and b, respectively. The mean fayalite mole fraction, X_{Fa}, ranges from 0.012 to 0.043 with a mean value of 0.023 for the Type Is, and from 0.12 to 0.24, with a mean value of 0.17 for the Type IIs, in good agreement with respective values of 0.010 (Jones and Scott, 1989) and 0.16 (Jones, 1990). The olivine phenocrysts in the Type IIs tend to have uniform cores and strongly zoned rims. Some chondrules, *e.g.*, #18 (Fig. A-1a) and #696 and #7 (Fig. A-1b), have rare grains with cores that are extremely Mg-rich compared to the continuous parts of the histograms. These cores are anhedral, 20–100 μm across and have diffuse contacts with the relatively FeO-rich olivine in which they are enclosed. Much more common are histograms without obvious relict grains and with long, low, discontinuous, higher-X_{Fa} tails extending to X_{Fa} of 0.49 (Type I) and 0.45 (Type II).

The compositions of mesostases of seven of the above chondrules that are free of terrestrial alteration effects were determined by energy-dispersive analysis. In the SEM, a beam was rastered over areas ~5 μm across (Type I) and ~10–40 μm across (Type II). From three to seven areas were analyzed in each chondrule. After normalization to 100 wt.% oxides, average FeO contents of the chondrule mesostases were found to be ~1.1 wt.% for the Type Is and to range from 5.1 to 9.5 wt.%, with an overall average of 7.4 ± 1.7 wt.% for the Type IIs. These values are quite similar to respective values of 0.74 (Jones and Scott, 1989) and 6.5–9.7 wt.% FeO, yielding a mean of 8.1 ± 1.1 wt.%, in nine chondrules free of pyroxene laths (Jones, 1990).

APPENDIX B. EVAPORATION COEFFICIENTS

Hashimoto (1983) performed vacuum evaporation experiments on molten chondrule analogs at several temperatures. Fedkin et al. (2006) modeled the predominant evaporation reactions in these experiments, and derived evaporation coefficients for $Mg_{(g)}$, $Fe_{(g)}$ and $SiO_{(g)}$ from silicate liquid, and their temperature dependences. These coefficients were used to model evaporation from MELTS liquids in this study. For the MgO-rich CMAS liquids encountered here, the values of γ^e_{SiO} and γ^e_{Mg} derived by Fedkin et al. (2006) from the experiments of Wang et al. (2001) were used. Ni is assumed to evaporate from silicate liquid with the same evaporation coefficient as Fe. Richter et al. (2009) performed evaporation experiments on molten chondrule analogs in vacuum at 1743 K, measured the rates of Na and K loss with time and determined that $\gamma^e_{Na} = 0.09$ and $\gamma^e_{K} = 0.06$, which are adopted here. Evaporation coefficients of the alkalis were assumed invariant with temperature in the present work. Insufficient data are available to determine a distinct value of γ^e_i for each evaporating species of a given element. The derived value is determined largely

Author's personal copy

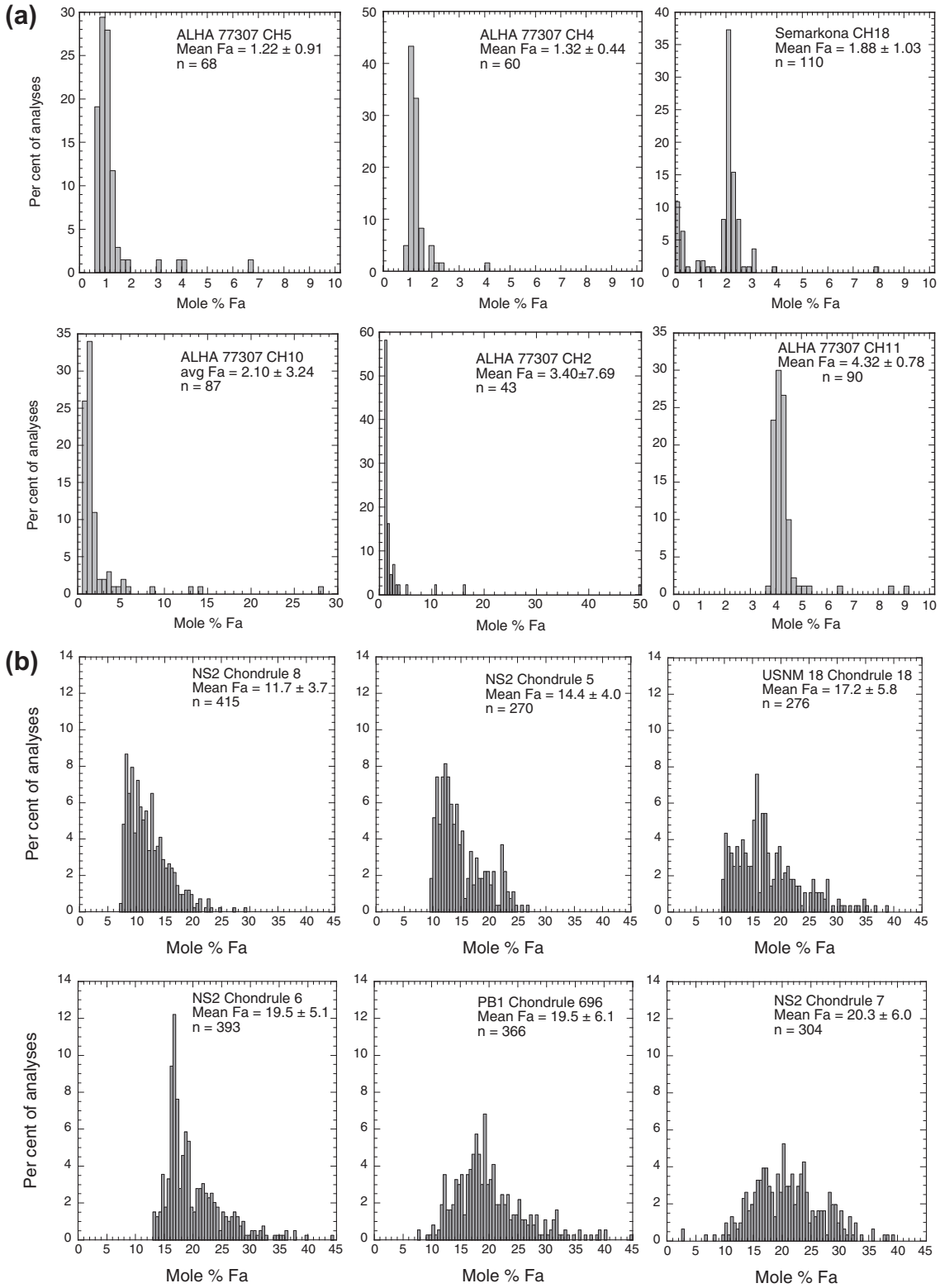

Fig. A-1. Histograms of fayalite content of olivine in individual (a) Type I PO chondrules in ALHA 77307 and Semarkona and (b) Type II chondrules in Semarkona. For Type II chondrules, the mode tends to be at a lower fayalite content than the median. Note the sporadic and rare occurrence of compositions to the low-X_{Fa} side of the continuous parts of the distributions, and the much more common occurrence of a long, discontinuous, low tail to high X_{Fa}. Note the variable bin widths within Fig. A-1a. One standard deviation uncertainties are shown for the means. n: number of analyses.

Author's personal copy

by γ_i^e for the dominant evaporating species. In modeling chondrule analogs in this work, however, the same evaporation reactions were found to predominate as in the above experiments, justifying use of the experimentally determined value in every term of Eq. (17) for a given element.

Tachibana et al. (in press) performed evaporation experiments on solid metallic Fe, and found that

$$In\gamma_{\mathrm{Fe}}^e = 1.44 - 2595/T, \tag{B1}$$

which is adopted in this work and assumed to be the same for liquid metallic iron and solid and liquid metallic nickel. Crystalline silicate and oxide phases were assumed not to evaporate.

Because there is virtually no information on the values of condensation coefficients for reactions relevant to chondrule compositions, γ_i^c is assumed to be identical to γ_i^e at the same temperature in this work. The one exception is that a different fit was made to the temperature dependence of γ_{SiO}^c from that of γ_{SiO}^e, in order to ensure near-total condensation of Si by 900 K.

APPENDIX C. EVAPORATION-INDUCED ISOTOPIC FRACTIONATIONS

Isotopic fractionation factors employed in this study were measured in vacuum evaporation experiments of liquid chondrite analogs for Fe at 1700 °C (Dauphas et al., 2004), Si at 1800 °C (Wang et al., 2001), K at 1470 °C (Richter et al., 2009) and Mg at 1800 °C and 2000 °C (Wang et al., 2001), and in vacuum evaporation experiments of CAI analogs for Mg at 1600, 1700 and 1900 °C (Richter et al., 2007). The isotopic fractionation factor measured in these experiments for one pair of isotopes was used to calculate those of the other pairs of isotopes of the same element by writing the Rayleigh equation in δ notation and expressing simple proportional relationships between the δ values of the different pairs. Separate evaporation coefficients for each isotopologue were then derived by writing Eq. (16) to express the flux of each isotopologue of the dominant evaporating species of each of Mg, Si and Fe, and then equating the total flux of that species to the sum of the fluxes of all isotopologues of that species. Of these elements, Mg is the only one known to have a temperature-dependent isotopic fractionation factor. In the model, the isotopic compositions of droplet and coexisting gas were calculated by using the separate evaporation coefficients derived herein to write Eq. (16) for the flux of each isotopologue of the dominant evaporating species.

Isotopic fractionation factors equal to the square root of the inverse mass ratios were determined experimentally for evaporation of iron from metallic solid iron (Tachibana et al., 2007). Thus, the evaporation coefficient for the dominant evaporating species of iron was used for each isotopologue of that species in Eq. (16). It is assumed here that the isotopic composition of a droplet of liquid metallic iron evolves according to the fractionation factor found for solid metallic iron. It is also assumed, however, that solid metallic iron is isotopically unfractionated during evaporation due to the inability of diffusion to homogenize isotopically fractionated iron on grain surfaces with isotopically normal iron in grain interiors prior to total evaporative loss of surface material.

APPENDIX D. NON-EQUILIBRIUM MELTING

Kirkpatrick (1975) showed that the rate of change of the radius of a dissolving crystal, r, is

$$\frac{dr}{dt} = \frac{fkT}{3\pi a_o^2 \eta}[1 - e^{-\Delta G_c/RT}], \tag{D1}$$

where f, k, a_o, η and ΔG_c are the fraction of surface sites available for detachment, the Boltzmann constant, the thickness of each molecular layer removed, the melt viscosity, and the free energy of fusion, respectively. In this work, f is assumed to be one and a_o equal to the maximum dimension of the unit cell for each silicate and oxide phase.

After the equilibrium assemblage was computed at 1400 K, 75% of each crystalline silicate and oxide phase was arbitrarily assumed not to equilibrate with the liquid, and the bulk composition of the equilibrating part of the system was calculated by subtraction. At the next temperature step, MELTS was used to calculate the free energy, ΔG_1, and viscosity of the liquid composition from the previous step. The bulk chemical composition of the equilibrating system was changed by addition of the sequestered olivine composition, in an amount so small that olivine remained undersaturated. MELTS was then used to determine the free energy of the new liquid composition, ΔG_2, while suppressing formation of all other silicate and oxide phases. The partial molar Gibbs free energy of olivine in the liquid is then $\Delta G_{lol} = \Delta G_2 - \Delta G_1$, divided by the incremental number of moles of olivine dissolved. The equivalent of the free energy of fusion of olivine in this multicomponent system is then $\Delta G_c = \Delta G_{lol} - \Delta G_{ol}$, where ΔG_{ol} is the molar free energy of solid olivine. An analogous computation was made for each of the other silicate and oxide phases at this temperature step, from which dr/dt was calculated. Each of these rates was multiplied by the time step size to yield the kinetically allowed decrease in radius, dr, of the grains of each phase, from which was calculated the mass of each phase that could be dissolved in the liquid.

Olivine, orthopyroxene, clinopyroxene, plagioclase and spinel were assumed to exist as spherical grains with initial radii, r_g, of 100, 100, 100, 50 and 10 μm, respectively. Because all grains of each phase are assumed to be the same size, the fractional mass of each phase whose chemical and isotopic composition is not equilibrated with the liquid can be expressed by the radius of an inner sphere, r_u, and the fraction that is equilibrated by the radius of an outer shell, r_e, where $r_g = r_u + r_e$. At a given temperature step, when the amount of a phase that can be dissolved, dr, was found from Eq. (D1) to be $>r_e$, r_g was reduced by dr, r_u was reduced by $dr - r_e$, and the mass of the previously unequilibrated amount of the phase within the shell of thickness $dr - r_e$ was added to the equilibrating system. After the trial amount of each phase that could be dissolved was computed in this way at each temperature step, and the chemical composition of the equilibrating system was modified from that of the previous step by the resulting addi-

Author's personal copy

tions of amounts of previously unequilibrated phases, MELTS was used to compute the equilibrium assemblage, from which the vapor pressures for this temperature step were calculated. It was found that the actual amount of a phase calculated to be in equilibrium with the liquid was always less than the amount within the shell of thickness dr, *i.e.*, the trial amount allowed by melting kinetics. Therefore, before proceeding to the next temperature step, the excess equilibrium amount of each phase was used to calculate a new r_e, within whose volume the chemical and isotopic composition was the same as the liquid, and r_g was increased by that amount.

This method has the effect of delaying dissolution of plagioclase by ~10 K and clinopyroxene by 25–35 K depending on the specific thermal history. Reducing the assumed grain sizes by factors of two, decreasing the values of a_o to the minimum dimensions of the unit cells and sequestering smaller fractions of the initial solids had little effect on these results. Although the method gradually introduces the initially sequestered solid fraction of the droplet into chemical communication with the liquid, all of it reaches equilibrium by the time the pre-shock temperature is reached in the investigated thermal histories. Thus, no relics of the initial precursors are preserved. This is probably because Eq. (D1) overestimates actual dissolution rates by taking into account diffusion only across crystal-melt interfaces but not within the liquid phase that, in the present work, is assumed instantaneously homogenized. Significant amounts of olivine exist in the model droplets at pre-shock temperatures because the latter are always below the liquidus. Although subsequent temperature spikes may be quite large, the total time during which this olivine is subjected to higher temperatures is only 1.5–3.8 min, depending on the specific thermal history. Although some olivine likely survives these temperature excursions, the present model is unable to predict the amount. Consequently, two different cases are investigated in this work for each thermal history. In one, referred to as the "porphyritic olivine", or "PO" case, 5 volume% of the pre-shock olivine is assumed to survive the temperature spike. In the other, the "barred olivine", or "BO" case, no olivine survives.

Because silicate liquid and metal are always assumed to be entirely in the equilibrating part of the system and these are the only phases allowed to evaporate, it is the equilibrating system that undergoes evaporative changes in its chemical and isotopic compositions during heating, while the sequestered fraction retains its original chemical and its normal isotopic composition. Because progressive equilibration of the droplet with increasing temperature and time occurs by gradual transfer of material from the sequestered fraction into the equilibrating fraction, the chemical and isotopic compositions of the bulk droplet do not change as fast as they would if the entire droplet were assumed always to be in liquid–crystal equilibrium. After its bulk chemical and isotopic compositions change at each time step, the equilibrating system is assumed to reach liquid–crystal equilibrium, and the isotopic composition of each element is equalized in every phase within it. Thus, even though the Fe isotopic compositions of the metal and silicate liquid phases evolve with different isotopic fractionation factors, the Fe isotopic compositions of all phases in the equilibrating system are equalized after each time step. This assumes that equilibrium and kinetic, metal–silicate and silicate-silicate Fe isotope fractionations are zero at chondrule melting temperatures, although evidence for small fractionations exists (Roskosz et al., 2006; Theis et al., 2008).

APPENDIX E. FRACTIONAL CRYSTALLIZATION

An empirical fractional crystallization model was derived from the experiments of Weinbruch et al. (1998) in which glasses of Type IIAB chondrule composition were placed in iron crucibles, brought from room temperature to 1500 °C, just below their liquidus, in ~1.5 h, held at that temperature for 30 min, cooled at controlled rates to 1000 °C, and then quenched. In the present work, wavelength dispersive analyses were performed on all phases in polished sections of the products of their runs 5 and 13 that were cooled at 100 °C/h and 10 °C/h, respectively, both within the range of cooling rates of natural chondrules. After the FeO contents were corrected for oxidation of the crucibles during heating, MELTS was used to simulate fractional crystallization of these runs. At a log f_{O_2} of IW, the equilibrium phase assemblage was calculated for the bulk compositions of each of the runs, a fraction of the total olivine was sequestered, and the bulk composition of the unsequestered fraction of each was calculated at two-degree temperature intervals from 1500 to 1000 °C. For each run, a set of histograms of sequestered olivine compositions was

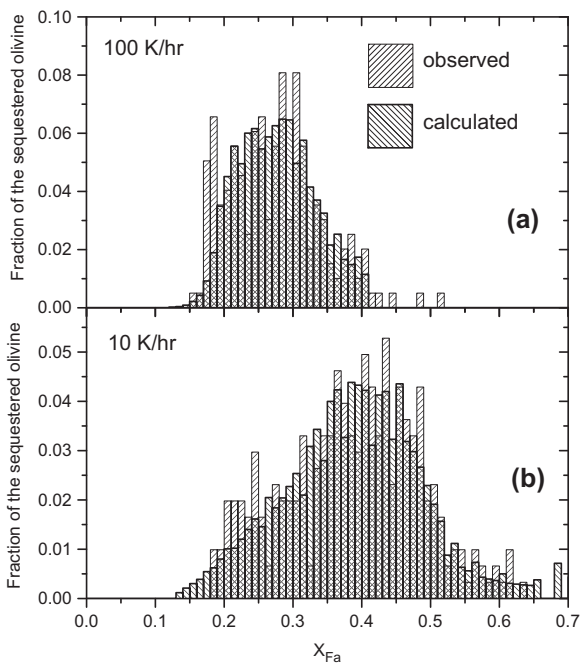

Fig. E-1. Histogram of fayalite content of olivine measured in experimental run products of Weinbruch et al. (1998) compared to that computed from the best-fit fractional crystallization model used in this work for their (a) run #5, made at a cooling rate of 100 K/hr, and (b) run #13, made at a cooling rate of 10 K/hr.

Author's personal copy

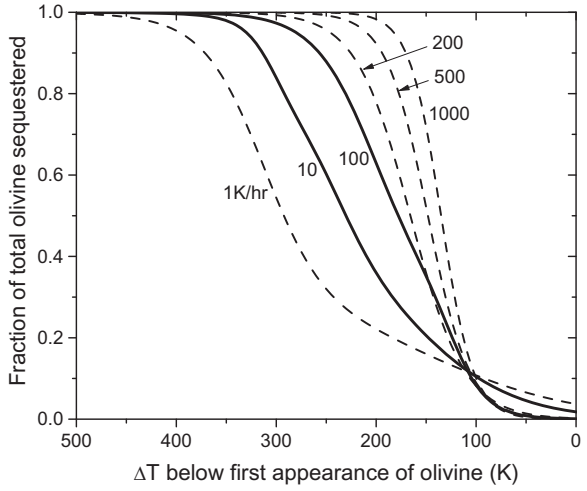

Fig. E-2. Functional relationship between the fraction of the total olivine isolated from equilibrium and the temperature below the first temperature of appearance of olivine. Solid curves are those that, when used with MELTS to model fractional crystallization, produced the computed histograms in Fig. E-1. Dashed curves for other cooling rates were derived by logarithmic extrapolation of the coefficients of the equations for the solid curves.

produced by varying the functional relationship between temperature and the total amount of olivine sequestered.

The best matches between observed and calculated histograms are shown in Fig. E-1. For run 5, the calculated histogram fits well the shape and fayalite range of the observed histogram but misses the noisy spike on the low-fayalite side of the peak and does not cover the highest-fayalite points in the tail. The fayalite content at the point of truncation of the modeled data, however, is entirely a function of the temperature at which orthopyroxene was assumed to nucleate after subcooling. For run 13, the calculated and observed histograms are in excellent agreement. For each run, the modeling also produced excellent agreement with the observed modal proportions of olivine, pyroxene and glass and with the measured glass composition.

Plots of the proportion of sequestered olivine as a function of temperature that produced the computed histograms for 100 °C/h and 10 °C/h are shown in Fig. E-2. The shapes of the curves are generally sigmoidal. During fractional crystallization, an ever-increasing proportion of the total olivine was isolated from chemical communication with the liquid as the temperature fell. Thus, while some of the earliest-formed olivine preserves the composition with which it crystallized, some of it re-equilibrated with liquid and changed its composition to that of newly-formed crystals before a fraction of that olivine was preserved, and so on. This makes general sense, in that early crystals are small enough that most of the volume of each is in chemical communication with surrounding liquid but, as the crystals grow with falling temperature, more and more of the volume of each is isolated from the liquid. Furthermore, much less of the total olivine is sequestered at any temperature in the more slowly cooled case. Logarithmic extrapolation of the coefficients for these curves was used to construct curves for the other cooling rates shown. Linear translations of the curves were used to model fractional crystallization beginning at temperatures other than 1500 °C. When fractional crystallization begins above the inflection temperature and extends to a temperature below it, where the cooling rate is lower, a different curve is used to model fractional crystallization during each of the two cooling stages.

REFERENCES

Alexander C. M. O'D. (2001) Exploration of quantitative kinetic models for the evaporation of silicate melts in vacuum and in hydrogen. *Meteoritics Planet. Sci.* **36**, 255–283.

Alexander C. M. O'D. (2004) Chemical equilibrium and kinetic constraints for chondrule and CAI formation conditions. *Geochim. Cosmochim. Acta* **68**, 3943–3969.

Alexander C. M. O'D. and Grossman J. N. (2005) Alkali elemental and potassium isotopic compositions of Semarkona chondrules. *Meteoritics Planet. Sci.* **40**, 541–556.

Alexander C. M. O'D. and Wang J. (2001) Iron isotopes in chondrules: implications for the role of evaporation during chondrule formation. *Meteoritics Planet. Sci.* **36**, 419–428.

Alexander C. M. O'D., Grossman J. N., Wang J., Zanda B., Bourot-Denise M. and Hewins R. H. (2000) The lack of potassium-isotopic fractionation in Bishunpur chondrules. *Meteoritics Planet. Sci.* **35**, 859–868.

Alexander C. M. O'D., Grossman J. N., Ebel D. S. and Ciesla F. J. (2008) The formation conditions of chondrules and chondrites. *Science* **320**, 1617–1619.

Armytage R. M. G., Georg R. B., Williams H. M. and Halliday A. N. (2012) Silicon isotopic composition of Allende chondrules and nebular processes (abstract). In *Papers Presented at the 43rd Lunar and Planetary Science Conference*. Lunar and Planetary Institute, Houston (Abstract #1971).

Berman R. G. (1983) A Thermodynamic Model for Multicomponent Melts, with Application to the System CaO–MgO–Al2O3–SiO2. Ph.D. dissertation, Univ. of British Columbia.

Bizzarro M., Baker J. A. and Haack H. (2004) Mg isotope evidence for contemporaneous formation of chondrules and refractory inclusions. *Nature* **431**, 275–278.

Bouvier A., Wadhwa M., Simon S. B. and Grossman L. (2009) Magnesium isotope compositions of chondrules from the Murchison and Murray carbonaceous chondrites. *Lunar Planet. Sci.* **XL**. Abstract #2193 (CD-ROM).

Campbell A. J., Humayun M. and Weisberg M. K. (2002) Siderophile element constraints on the formation of metal in the metal-rich chondrites Bencubbin, Weatherford, and Gujba. *Geochim. Cosmochim. Acta* **66**, 647–660.

Cassen P. (2001) Nebular thermal evolution and the properties of primitive planetary materials. *Meteoritics Planet. Sci.* **36**, 671–700.

Chakraborty S. (2010) Diffusion coefficients in olivine, wadsleyite and ringwoodite. In *Diffusion in Minerals and Melts* (eds. Y. Zhang and D.J. Cherniak), Rev. Mineral. Geochem. 72, pp. 603–639.

Chakraborty S. and Ganguly J. (1991) Compositional zoning and cation diffusion in garnets. In Diffusion, Atomic Ordering and Mass Transport (ed. J. Ganguly). *Advances in Physical Geochemistry* **8**, 120–175.

Chase, M.W. Jr. (1998) NIST-JANAF Thermochemical Tables. Fourth Edition. *J. Phys. Chem. Ref. Data, Monograph 9*. American Institute of Physics, Woodbury, New York.

Ciesla F. J. (2005) Chondrule-forming processes-an overview. In *Chondrites and the Protoplanetary Disk, ASP Conference Series*

Author's personal copy

341 (eds. A. N. Krot, E. R. D. Scott and B. Reipurth). Astronomical Society of the Pacific, San Francisco, CA, pp. 811–820.

Ciesla F. J. and Cuzzi J. N. (2006) The evolution of the water distribution in a viscous protoplanetary disc. *Icarus* **181**, 178–204.

Ciesla F. J. and Hood L. L. (2002) The nebular shock wave model for chondrule formation: shock processing in a particle-gas suspension. *Icarus* **158**, 281–293.

Ciesla F. J., Lauretta D. S., Cohen B. A. and Hood L. L. (2003) A nebular origin for fine-grained phyllosilicates. *Science* **299**, 549–552.

Clayton R. N., Onuma N., Ikeda Y., Mayeda T. K., Hutcheon I. D., Olsen E. J. and Molini-Velsko C. (1983) Oxygen isotopic compositions of chondrules in Allende and ordinary chondrites. In *Chondrules and their Origins* (ed. E. A. King). Lunar and Planetary Institute, pp. 37–43.

Clayton R. N., Mayeda T. K., Goswami J. N. and Olsen E. J. (1991) Oxygen isotope studies of ordinary chondrites. *Geochim. Cosmochim. Acta* **55**, 2317–2337.

Crank J. (1989) *The Mathematics of Diffusion*. Arrowsmith, Bristol, pp. 414.

Cuzzi J. N., Hogan R. C., Paque J. M. and Dobrovolskis A. R. (2001) Size-selective concentration of chondrules and other small particles in protoplanetary nebula turbulence. *Astrophys. J.* **546**, 496–508.

Dauphas N. and Rouxel O. (2005) Mass spectrometry and natural variations of iron isotopes. *Mass Spectrom. Rev.* **25**, 515–550.

Desch S. J. and Connolly, Jr., H. C. (2002) A model of the thermal processing of particles in solar nebula shocks: application to the cooling rates of chondrules. *Meteoritics Planet. Sci.* **37**, 183–207.

Desch S. J., Ciesla F. J., Hood L. L. and Nakamoto T. (2005) Heating of chondritic materials in solar nebula shocks. In *Chondrites and the Protoplanetary Disk, ASP Conference Series 341* (eds. A. N. Krot, E. R. D. Scott and B. Reipurth). Astronomical Society of the Pacific, San Francisco, CA, pp. 849–872.

Dohmen R. and Chakraborty S. (2007) Fe–Mg diffusion in olivine II: point defect chemistry, change of diffusion mechanisms and a model for calculation of diffusion coefficients in natural olivine. *Phys. Chem. Minerals* **34**, 409–430.

Fedkin A. V. and Grossman L. (2006) The fayalite content of chondritic olivine: obstacle to understanding the condensation of rocky material. In *Meteorites and the Early Solar System II* (eds. D. S. Lauretta and , Jr.H. Y. McSween). Univ. AZ Press, Tucson, AZ, pp. 279–294.

Fedkin A. V., Grossman L. and Ghiorso M. S. (2006) Vapor pressures and evaporation coefficients for melts of ferromagnesian chondrule-like compositions. *Geochim. Cosmochim. Acta* **70**, 206–223.

Fedkin A. V., Ciesla F. J. and Grossman L. (2008) Shock wave models: dependence of thermal history and Type II chondrule composition on water and dust enrichment. *Lunar Planet. Sci.* **XXXIX**. Abstract #1834 (CD-ROM).

Fedkin A. V., Grossman L., Ciesla F. J. and Simon S. B. (2011) Mineralogical and isotopic effects of shock wave thermal histories on chondrule precursors (abstract). In *Papers Presented at the 42nd Lunar and Planetary Science Conference*. Lunar and Planetary Institute, Houston (Abstract #2123).

Galy A., Young E. D., Ash R. D. and O'Nions R. K. (2000) The formation of chondrules at high gas pressures in the solar nebula. *Science* **290**, 1751–1753.

Galy A., Yoffe O., Janney P. E., Williams R. W., Cloquet C., Alard O., Halicz L., Wadhwa M., Hutcheon I. D., Ramon E. and Carignan J. (2003) Magnesium isotope heterogeneity of the isotopic standard SRM980 and new reference materials for magnesium-isotope-ratio measurements. *J. Anal. At. Spectrom.* **18**, 1352–1356.

Georg R. B., Halliday A. N., Schauble E. A. and Reynolds B. C. (2007) Silicon in the Earth's core. *Nature* **447**, 1102–1106.

Ghiorso M. S. and Sack R. O. (1995) Chemical mass transfer in magmatic processes IV. A revised and internally consistent thermodynamic model for the interpolation and extrapolation of liquid-solid equilibria in magmatic systems at elevated temperatures and pressures. *Contrib. Mineral. Petrol.* **119**, 197–212.

Grossman L. and Fedkin A. V. (2003) $CaO–MgO–Al_2O_3–SiO_2$ liquids: chemical and isotopic effects of Mg and Si evaporation in a closed system of solar composition. *Geochim. Cosmochim. Acta* **67**, 4205–4221.

Grossman L., Ebel D. S., Simon S. B., Davis A. M., Richter F. M. and Parsad N. M. (2000) Major element chemical and isotopic compositions of refractory inclusions in C3 chondrites: the separate roles of condensation and evaporation. *Geochim. Cosmochim. Acta* **64**, 2879–2894.

Grossman L., Beckett J.R., Fedkin A.V., Simon S.B. and Ciesla F.J. (2008) Redox conditions in the solar nebula: observational, experimental and theoretical constraints. In *Oxygen in the Solar System* (eds. G.J. MacPherson, D.W. Mittelfehldt, J.H. Jones and S.B. Simon), Rev. Mineral. Geochem 68, pp. 93–140.

Hewins R. H. and Connolly, Jr., H. C. (1996) Peak temperatures of flash-melted chondrules. In *Chondrites and the Protoplanetary Disk* (eds. R. H. Hewins, R. H. Jones and E. R. D. Scott). Cambridge University Press, New York, pp. 197–204.

Hewins R. H. and Radomsky P. M. (1990) Temperature conditions for chondrule formation. *Meteoritics* **25**, 309–318.

Hewins R. H., Ganguly J. and Mariani E. (2009) Diffusion modeling of cooling rates of relict olivine in Semarkona chondrules. *Lunar Planet. Sci.* **XL**. Abstract # (CD-ROM).

Hezel D. C., Needham A. W., Armytage R., Georg B., Abel R. L., Kurahashi E., Coles B. J., Rehkämper M. and Russell S. S. (2010) A nebula setting as the origin for bulk chondrule Fe isotope variations in CV chondrites. *Earth Planet. Sci. Lett.* **296**, 423–433.

Hood L. L. and Horanyi M. (1991) Gas dynamic heating of chondrule precursor grains in the solar nebula. *Icarus* **93**, 259–269.

Hood L. L. and Horanyi M. (1993) The nebular shock wave model for chondrule formation – One-dimensional calculations. *Icarus* **106**, 179–189.

Humayun M. and Clayton R. N. (1995) Potassium isotope cosmochemistry: genetic implications of volatile element fractionation. *Geochim. Cosmochim. Acta* **59**, 2131–2148.

Iida A., Nakamoto T., Susa H. and Nakagawa Y. (2001) A shock heating model for chondrule formation in a protoplanetary disk. *Icarus* **153**, 430–450.

Jones R. H. (1990) Petrology and mineralogy of Type II, FeO-rich chondrules in Semarkona (LL3.0): origin by closed-system fractional crystallization, with evidence for supercooling. *Geochim. Cosmochim. Acta* **54**, 1785–1802.

Jones R. H. (1994) Petrology of FeO-poor, porphyritic pyroxene chondrules in the Semarkona chondrite. *Geochim. Cosmochim. Acta* **58**, 5325–5340.

Jones R. H. (1996) FeO-rich, porphyritic pyroxene chondrules in unequilibrated ordinary chondrites. *Geochim. Cosmochim. Acta* **60**, 3115–3138.

Jones R. H. and Scott E. R. D. (1989) Petrology and thermal history of Type IA chondrules in the Semarkona (LL3.0) chondrite. In *Proc. 19th Lunar Planet. Sci. Conf.*. Lunar and Planetary Institute, Houston, TX, pp. 523–536.

Author's personal copy

Jones R. H., Grossman J. N. and Rubin A. E. (2005) Chemical, mineralogical and isotopic properties of chondrules: clues to their origin. In *Chondrites and the Protoplanetary Disk, ASP Conference Series 341* (eds. A. N. Krot, E. R. D. Scott and B. Reipurth). Astronomical Society of the Pacific, San Francisco, CA, pp. 251–285.

Kehm K., Hauri E. H., Alexander C. M. O'D. and Carlson R. W. (2003) High precision iron isotope measurements of meteoritic material by cold plasma ICP-MS. *Geochim. Cosmochim. Acta* **67**, 2879–2891.

Krot A. N., Amelin Y., Cassen P. and Meibom A. (2005) Young chondrules in CB chondrites from a giant impact in the early Solar System. *Nature* **436**, 989–992.

Marcus R. A., Fedkin A. V. and Grossman L. (2010) Condensation and evaporation from thermally unequilibrated phases. *Meteoritics Planet. Sci.* **45**(Suppl.), A126 (abstr.).

Miura H. and Nakamoto T. (2006) Shock-wave heating model for chondrule formation: prevention of isotopic fractionation. *Astrophys. J.* **651**, 1272–1295.

Miura H., Nakamoto T. and Doi M. (2008) Origin of three-dimensional shapes of chondrules: I. Hydrodynamics simulations of rotating droplet exposed to high-velocity rarefied gas flow. *Icarus* **197**, 269–281.

Miyamoto M., Koizumi E. and Mikouchi T. (2008) A wide range of the cooling rate of Type II porphyritic olivine chondrules in Semarkona (LL3.0). *Lunar Planet. Sci.* **XXXIX** (Abstract #1587 (CD-ROM)).

Morris M. A. and Desch S. J. (2010) Thermal histories of chondrules in solar nebula shocks. *Astrophys. J.* **722**, 1474–1494.

Morris M. A., Desch S. J. and Ciesla F. J. (2009) Cooling of dense gas by H_2O line emission and an assessment of its effects in chondrule-forming shocks. *Astrophys. J.* **691**, 320–331.

Morris M. A., Desch S. J. and Ciesla F. J. (2009b) Thermal histories of chondrules in solar nebula shocks. *Meteoritics Planet. Sci.* **44**(Suppl.), A148 (abstr.).

Mullane E., Russell S. S. and Gounelle M. (2005) Nebular and asteroidal modification of the iron isotope composition of chondritic components. *Earth Planet. Sci. Lett.* **239**, 203–218.

Nagahara H., Kita N. T., Ozawa K. and Morishita Y. (2008) Condensation of major elements during chondrule formation and its implication to the origin of chondrules. *Geochim. Cosmochim. Acta* **72**, 1442–1465.

Neufeld D. A. and Kaufman M. J. (1993) Radioactive cooling of warm molecular gas. *Astrophys. J.* **418**, 263–272.

Whattam S. A. and Hewins R. H. (2009) Granoblastic olivine aggregates as precursors of Type I chondrules: an experimental test. *Geochim. Cosmochim. Acta* **73**, 5460–5482.

Young E. D., Ash R. D., Galy A. and Belshaw N. S. (2002) Mg isotope heterogeneity in the Allende meteorite measured by UV laser ablation-MC-ICPMS and comparisons with O isotopes. *Geochim. Cosmochim. Acta* **66**, 683–698.

Zhu X. K., Guo Y., O'Nions R. K., Young E. D. and Ash R. D. (2001) Isotopic homogeneity of iron in the early solar nebula. *Nature* **412**, 311–313.

Appendix References

Dauphas N., Janney P. E., Mendybaev R. A., Wadhwa M., Richter F. M., Davis A. M., van Zuilen M., Hines R. and Foley C. N. (2004) Chromatographic separation and multicollection-ICPMS analysis of iron. Investigating mass-dependent and -independent isotope effects. *Anal. Chem.* **76**, 5855–5863.

Fedkin A. V., Grossman L. and Ghiorso M. S. (2006) Vapor pressures and evaporation coefficients for melts of ferromagnesian chondrule-like compositions. *Geochim. Cosmochim. Acta* **70**, 206–223.

Hashimoto A. (1983) Evaporation metamorphism in the early solar nebula-evaporation experiments on the melt $FeO–MgO–SiO_2–CaO–Al_2O_3$ and chemical fractionations in primitive materials. *Geochem J.* **17**, 111–145.

Jones R. H. (1990) Petrology and mineralogy of Type II, FeO-rich chondrules in Semarkona (LL3.0): origin by closed-system fractional crystallization, with evidence for supercooling. *Geochim. Cosmochim. Acta* **54**, 1785–1802.

Jones R. H. and Scott E. R. D. (1989) Petrology and thermal history of Type IA chondrules in the Semarkona (LL3.0) chondrite. In *Proc. 19th Lunar Planet. Sci. Conf.*. Lunar and Planetary Institute, Houston, TX, pp. 523–536.

Kirkpatrick R. J. (1975) Crystal growth from a melt: a review. *Am. Mineral.* **60**, 798–814.

Richter F. M., Janney P. E., Mendybaev R. A., Davis A. M. and Wadhwa M. (2007) Elemental and isotopic fractionation of Type B CAI-like liquids by evaporation. *Geochim. Cosmochim. Acta* **71**, 5544–5564.

Richter F. M., Mendybaev R. A., Christensen J., Gaffney A. and Ebel D. S. (2009) Elemental and isotope fractionation of chondrule-like liquids by evaporation into vacuum. *Lunar Planet. Sci.* **XL**. Abstract #2321 (CD-ROM).

Roskosz M., Luais B., Watson H. C., Toplis M. J., Alexander C. M. O'D. and Mysen B. O. (2006) Experimental quantification of the fractionation of Fe isotopes during metal segregation from a silicate melt. *Earth Planet. Sci. Lett.* **248**, 851–867.

Tachibana S., Nagahara H., Ozawa K., Ikeda Y., Nomura R., Tatsumi K. and Joh Y. (In press) Kinetic condensation and evaporation of metallic iron and implications to metallic iron dust formation. *Astrophys. J.*

Tachibana S., Nagahara H., Ozawa K. and Yamada M. (2007) Isotopic fractionation of iron during kinetic evaporation of metallic iron. *Meteoritics Planet. Sci.* **42**(Suppl.), A146 (abstr.).

Theis K. J., Burgess R., Lyon I. C. and Sears D. W. (2008) The origin and history of ordinary chondrites: a study by iron isotope measurements of metal grains from ordinary chondrites. *Geochim. Cosmochim. Acta* **72**, 4440–4456.

Wang J., Davis A. M., Clayton R. N., Mayeda T. K. and Hashimoto A. (2001) Chemical and isotopic fractionation during the evaporation of the $FeO–MgO–SiO_2–CaO–Al_2O_3–TiO_2$ rare earth element melt system. *Geochim. Cosmochim. Acta* **65**, 479–494.

Weinbruch S., Büttner H., Holzheid A., Rosenhauer M. and Hewins R. H. (1998) On the lower limit of chondrule cooling rates: the significance of iron loss in dynamic crystallization experiments. *Meteoritics Planet. Sci.* **33**, 65–74.

Associate editor: Sara S. Russell